UNIVERSITY OF CALIFORNIA
RIVERSIDE

Transition Metal Boride Nanoparticles for Hydrogen Evolution Reaction Electrocatalysis

A Dissertation submitted in partial satisfaction
of the requirements for the degree of

Doctor of Philosophy

in

Chemical and Environmental Engineering

by

Sang Bum Kim

September 2025

Dissertation Committee:
Dr. Boniface P. T. Fokwa, Chairperson
Dr. Juchen Guo
Dr. Pingyun Feng

The Dissertation of Sang Bum Kim is approved:

Committee Chairperson

University of California, Riverside

ACKNOWLEDGEMENTS

Countless people supported my efforts in this thesis. First and foremost, my deepest appreciation goes to my advisor, Professor Boniface P. T. Fokwa, for his outstanding supervision, guidance, and encouragement. Whenever my research was stuck, his clear advice and steady confidence helped me move forward. I am profoundly grateful for the patience, high standards, and fundamental training in solid-state chemistry and depth of knowledge I gained under his mentorship. Thank you very much, Professor Fokwa.

I would also like to thank my dissertation committee members, Dr. Juchen Guo and Dr. Pingyun Feng, for their time, insightful questions, and constructive feedback. Their guidance strengthened this work and deepened my perspective on chemistry, materials science, and electrochemistry, and shaped the mindset I bring to endeavors beyond research.

I am indebted to my past and present lab mates and friends: Dr. Eunsoo Lee, Dr. Amir Ardalan Rezaie, Dr. Diana Luong, Dr. Kate Gibson, Dr. Johan Yapo, and Shola Elijah Adeniji for the many discussions, troubleshooting, and day-to-day teamwork that made this journey meaningful. In particular, I am grateful to Johan for computational analyses that pushed my results further, and to Shola, whose optimism and support, as the last lab member working alongside me in the run-up to graduation, kept me grounded. I also thank my collaborators Hyeonkyeong (Elly) Lee and Logan Quach for their work on our manuscripts and for helping carry key results across the finish line. I cherish the memories with each of you.

Finally, my deepest thanks go to my family for their unwavering love and support: my mother, Younghwa Choi; my father, Yoonkwon Kim; and my sister, Jungmin Kim. I am especially grateful to my nearby family, including Cecilia, Mick, Ella Kim, and Jisun Hong, for caring for me and encouraging me through the most challenging stretches. Lastly, my dearest friends, Danny Cho in Seoul and Jangwon Kim in Houston, and especially Joowon Lee in Riverside, who has been here with me, were indispensable to this journey. To all my extended family and everyone who believed in me, this accomplishment is ours.

COPYRIGHT ACKNOWLEDGEMENTS

DFT calculation was conducted by Dr. Johan Yapo.

ABSTRACT OF THE DISSERTATION

Transition Metal Boride Nanoparticles for Hydrogen Evolution Reaction Electrocatalysis

by

Sang Bum Kim

Doctor of Philosophy, Graduate Program in Chemical and Environmental Engineering
University of California, Riverside, September 2025
Dr. Boniface P. T. Fokwa, Chairperson

Green hydrogen production demands electrocatalysts that are efficient, durable, and composed of earth-abundant elements, particularly under device-relevant current densities ($\geq 10^2$-10^3 mA cm^{-2}). This thesis advances transition-metal boride (TMB) electrocatalysts for the hydrogen evolution reaction (HER) by coupling low-temperature redox–flux synthesis with precursor/feed-chemistry control to access nanoscale, boron-rich phases that operate at electrolyzer-level currents. First, vanadium substitution stabilizes α-MoB, enabling single-phase $V_{0.3}Mo_{0.7}B$ nanoparticles that outperform commercial Pt/C at high currents: an overpotential of 0.452 V achieves 1000 mA cm^{-2} in 0.5 M H_2SO_4, nearly half that of Pt/C (η_{1000} = 0.837 V). Mechanistically, $V_{0.3}Mo_{0.7}B$ exhibits the largest electrochemically active surface area (C_{dl} = 18.6 mF cm^{-2}) and the lowest charge-transfer resistance (R_{ct} = 35.2 Ω) among the Mo-boride controls, consistent with dense active-site populations and facile charge transport.

Next, we map a MoB_2 synthesis space in which stoichiometric or B-rich feeds, moderated by Sn flux, access phase-pure MoB_2 (MoB_2-SP) or MoB_2/B composites under mild ramps (800 °C, 2 °C min^{-1}), clarifying how excess boron promotes phase purity but can introduce resistive B-rich overlayers. Finally, we develop a halide-directed iodide/KCl route to nanosized RuB_2/Ru_2B_3 (I-RuB_2/Ru_2B_3) and benchmark it head-to-head against a conventional $RuCl_3$/Sn route: the iodide path yields smaller particles and superior activity (0.5 M H_2SO_4: 13.0/101.7 mV at 10/150 mA cm^{-2}; 1 M KOH: 15.6/122 mV), sub-30 mV dec^{-1} Tafel slopes, and ~97% retention after 5000 cycles in alkaline electrolyte. Collectively, these results establish precursor/flux-engineering principles that enable true nanosizing of boron-rich TMBs and deliver HER performance competitive with noble-metal benchmarks at technologically relevant current densities.

Table of Contents

Acknowledgements ..... **iv**

Abstract ..... **vii**

Table of Contents ..... **ix**

List of Figures ..... **xi**

List of Tables ..... **xv**

Chapter 1. Introduction **1**

1.1 An Overview of Hydrogen Energy and Electrocatalysts 1

1.2 Hydrogen Evolution (HER) 3

1.3 Transition Metal Borides (TMBs) and their Nanoparticles 6

1.4 Synthesis Method 12

1.5 Characterization Techniques 13

1.6 References 16

Chapter 2. Vanadium-Stabilized MoB Nanoparticles Enable Hydrogen Evolution at Industry-Relevant High Current Densities **22**

2.1 Introduction 23

2.2 Experimental Section 27

2.3 Computational Details 28

2.4 Results and Discussion 30

2.5 Conclusion 50

2.6 References 51

Chapter 3. Stoichiometric α-MoB_2 and MoB_2/MoB Composites for Ampere-Level Hydrogen Evolution: Tin and Boron Guided Morphology and Phase Design 57

3.1 Introduction.....58

3.2 Experimental Section.....64

3.3 Results and Discussion.....65

3.4 Conclusion.....80

3.5 References.....81

Chapter 4. Redox-Flux-Assisted Iodide Chemistry Yields Nanosized RuB_2/Ru_2B_3 Composites for Hydrogen Evolution in Acidic and Alkaline Media: Managing Iodide Volatility.....87

4.1 Introduction.....88

4.2 Experimental Section.....91

4.3 Results and Discussion.....93

4.4 Conclusion.....101

4.5 References.....103

Chapter 5. Conclusion 107

List of Figures

Figure 1.1 (left) Scheme of water electrolysis system and (right) different reactions in acidic and alkaline solution.....3

Figure 1.2 HER mechanisms in (a) acidic and (b) alkaline solutions. 4

Figure 1.3 HER volcano plot. The data points are measured exchange current density plotted versus the calculated free energy of H adsorption at $U = 0$ V. The metals on the left side of the volcano have high H coverage (1 ML) and the metals on the right side low H coverage (0.25 ML). The line is a prediction by a kinetic model in which all input parameters are taken from DFT calculations.....5

Figure 1.4 Different structures formed by boron atoms in transition metal borides. (a) isolated atomic boron, (b) pairs, (c) zig-zag chains, (d) straight chains, (e) extended chains, (f) double chains, (g) triple chains, (h) corrugated networks, and (i) flat networks of boron atoms 6

Figure 2.1 (a) Powder X-ray diffraction pattern of synthesized $V_{0.3}Mo_{0.7}B$ (top) compared with the theoretical pattern (bottom). Inset: crystal structure of $V_{0.3}Mo_{0.7}B$ (space group $I4_1/amd$). (b) HRSEM image showing lattice distortions (stacking faults). (c) High-resolution transmission electron microscopy (HRTEM) image and (d) atomic-resolution high-angle annular dark-field scanning transmission electron microscopy (HAADF-STEM) image of $V_{0.3}Mo_{0.7}B$ nanoparticles, displaying interplanar spacings (slightly inaccurate due to lattice distortions, see red rectangle); the bright dots represent metal atoms.....30

Figure 2.2 Powder X-ray diffraction data of synthesized products of reaction feed rate of VCl_3:$MoCl_5$:B:Sn = a) 0:1:1:2.0 (MoB/Mo), b) 0.5:0.5:1:2.0, c) 0.3:0.7:1:2.2, d) 0:1:2:2.5 (MoB/B) and e) 0.3:0.7:1:2.0 (Before HCl). Peaks of impurity phases are indicated (*: Mo and +: unknown phase that can be removed after HCl treatment). The reaction conditions are the same for all samples at 800°C for 4 hours, except (d) MoB/B for 8 hours.....33

Figure 2.3 HRSEM image of (a) $V_{0.3}Mo_{0.7}B$, (b) MoB/Mo, and (c) MoB/B.....34

Figure 2.4 EDS mapping of $V_{0.3}Mo_{0.7}B$ for metals (Mo & V) in (a) wide and (b) close up views. 34

Figure 2.5 SEM image and the corresponding EDS mapping of (a) MoB/Mo and (b) MoB/B to compare B and Mo ratio. 35

Figure 2.6 (a) Selected area electron diffraction (SAED) pattern, (b) high-resolution STEM image and (c) calculated model structure of $V_{0.3}Mo_{0.7}B$.....35

Figure 2.7 Deconvoluted XPS spectra of $V_{0.3}Mo_{0.7}B$: a) core-level V 2p, b) core-level Mo 3d, and c) core-level B 1s.....38

Figure 2.8 Linear sweep polarization curves of different materials ($V_{0.3}Mo_{0.7}B$, MoB/Mo, MoB/B, and 20% Pt/C) recorded in 0.5 M H_2SO_4 at current densities up to (a) 150 and (c) 1000 mA cm^{-2}. (b) Tafel plots of these materials. (d) Charging current density difference plotted against scan rate to determine the double-layer capacitance (C_{dl}) of the borides samples. (e) Nyquist plot representations of the electrochemical impedance spectra of the borides samples. (f) Polarization curves of $V_{0.3}Mo_{0.7}B$ electrode after 5000 cycles.....39

Figure 2.9 C_{dl} measurements from cyclic voltammetry profiles at different scan rates from 20 to 200 mV/s for (a) $V_{0.3}Mo_{0.7}B$, (b) MoB/Mo, (c) MoB/B. 42

Figure 2.10 Chronoamperometry curve of $V_{0.3}Mo_{0.7}B$ electrode for 24 h in 0.5 M H_2SO_4.....44

Figure 2.11 Deconvoluted XPS spectra of $V_{0.3}Mo_{0.7}B$ after activity/stability test at 1000 mA/cm^2: (a) core-level B 1s, (b) core-level V 2p, and (c) core-level Mo 3d.....45

Figure 2.12 Surface slab models for the {112} surface of (a) MoB and (b) $V_{0.31}Mo_{0.69}B$.....45

Figure 2.13 Powder X-ray diffraction data (red circles) of $V_{0.3}Mo_{0.7}B$, the Rietveld refined data (black line), and the difference curve (orange line) between observed and refined data (a) without preferred orientation and (b) with (112) preferred orientation.....46

Figure 2.14 Calculated Gibbs free energy diagram for 25% and 100% hydrogen coverage of different HER active sites on surfaces of $V_{0.3125}Mo_{0.6875}B$, MoB, and Pt. 47

Figure 2.15 Different HER active sites on surfaces of (a) & (b) MoB and (c) & (d) $V_{0.3125}Mo_{0.6875}B$, at high and low hydrogen coverages.....47

Figure 3.1. Powder X-ray diffraction patterns of synthesized (a) MoB_2/MoB, (b) MoB_2-SP, and (c) MoB_2/B. Energy dispersive X-ray spectroscopy (EDS) elemental mapping of Mo and B in (d) MoB_2/MoB, (e) MoB_2-SP, and (f) MoB_2/B. 66

Figure 3.2. EDS elemental spectra associated with EDS mapping in Fig. 3.1 of (a) MoB_2/MoB, (b) MoB_2-SP, and (c) MoB_2/B.....67

Figure 3.3. SEM images of (a) MoB_2/MoB, (b) MoB_2-SP, and (c) MoB_2/B. Isothemerms of (d) MoB2/MoB, (e) MoB2-SP, and (f) MoB2/B, and the insets showing pore volume distribution. 69

Figure 3.4. HRTEM image of MoB_2/MoB nanoparticles with MoB c-lattice and MoB_2 b-lattice 71

Figure 3.5. High-resolution XPS spectra of Mo 3d, B 1s and O 1s of MoB_2/MoB (a–c), MoB_2-SP (d–f), and MoB_2/B (g–i). 72

Figure 3.6. Linear sweep polarization curves of different electrodes of MoB_2/MoB, MoB_2-SP, MoB_2/B and 20% Pt/C recorded in 0.5 M H_2SO_4 at (a) 150 mA/cm^2 and (d) 1000 mA/cm^2. (b) Tafel slopes of these materials at different current densities. (c) Charging current density difference plotted against scan rate to yield double-layer capacitance (C_{dl}) of the borides samples. (e) Polarization curves of MoB_2/MoB electrode before and after 5000 cycles. (f) Chronoamperometry curve of MoB_2/MoB electrode for 24 h.....76

Figure 3.7. Linear sweep polarization curves of different electrodes of MoB_2/MoB, MoB_2-SP, MoB_2/B and 20% Pt/C recorded in 0.5 M H_2SO_4 at 10 mA/cm^2. 77

Figure 3.8. Tafel plots of MoB_2/MoB, MoB_2-SP, MoB_2/B and Pt/C electrodes at different current densities of (a) 10, (b) 100, and (c) 1000 mA/cm^2. 77

Figure 3.9. Nyquist plot representations of the electrochemical impedance spectra of the borides samples of (red) MoB_2/MoB, (blue) MoB_2-SP, and (green) MoB_2/B. 77

Figure 3.10. C_{dl} measurements from cyclic voltammetry profiles at different scan rates from 20 to 200 mV/s for (a) MoB_2/MoB, (b) MoB_2-SP, and (c) MoB_2/B. 78

Figure 3.11. Polarization curves of (a) MoB_2-SP and (b) MoB_2/B electrodes before and after 5000 cycles. 79

Figure 4.1. Powder X-ray diffraction (PXRD) of ruthenium boride products prepared by halide-directed, flux-assisted synthesis. (a) I-RuB_2/Ru_2B_3 and (b) Cl-RuB_2/Ru_2B_3.....93

Figure 4.2. Powder X-ray diffraction data of synthesized products of different Ru:B ratio with KCl or Sn at different reaction temperatures and heating rates. (a) 1:2+KCl at 800 °C with 2 °C/min, (b) 1:2+KCl at 800 °C with 0.5 °C/min, (c) 1:4+KCl at 800 °C with 0.5 °C/min, and (d) (Cl-RuB_2/B) 1:8+Sn at 850 °C with 2°C/min. 94

Figure 4.3. SEM images of (a) I-RuB_2/Ru_2B_3 and (b) Cl-RuB_2/Ru_2B_3, and the energy dispersive X-ray spectroscopy (EDS) elemental mapping of Ru and B in (c) I-RuB_2/Ru_2B_3 and (d) Cl-RuB_2/Ru_2B_3.....96

Figure 4.4. (a) SEM image and (b) energy dispersive X-ray spectroscopy (EDS) elemental mapping of Ru and B of Cl-RuB_2/B.....96

Figure 4.5. EDS mapping of I-RuB_2/Ru_2B_3 (Ru, B, and K) in (a) wide and (b) close-up views. 97

Figure 4.6. EDS elemental spectra of (a) I-RuB_2/Ru_2B_3, (b) Cl-RuB_2/Ru_2B_3, and (c) Cl-RuB_2/B for Ru & B from the mapping in **Figure 4.3** and **4.4**.. 98

Figure 4.7. Linear sweep polarization curves of I-RuB_2/Ru_2B_3, Cl-RuB_2/Ru_2B_3, Cl-RuB_2/B, and 20% Pt/C electrodes (a) in 0.5 M H_2SO_4 and (b) 1 M KOH. Tafel slopes of these materials (c) in 0.5 M H_2SO_4 and (d) 1 M KOH. Polarization curves of I-RuB_2/Ru_2B_3 electrode before and after 5000 cycles (e) in 0.5 M H_2SO_4 and (f) 1 M KOH.....99

List of Tables

Table 2.1 XPS peak position and full width at half maximum (FWHM) parameters for V 2p, Mo 3d, and B 1s of $V_{0.3}Mo_{0.7}B$ before and after HER.. 38

Table 2.2 Fitted EIS data from Nyquist Plots in **Figure 2.8e**.. 42

Table 3.1 Composition of the three samples measured from EDS (**Figure 3.1** & **3.2**) ……..68

Table 3.2 Textural parameters from N_2 physisorption at 77 K. Specific surface area (S_{BET}) was obtained by multipoint BET from adsorption branch. Total pore volume (V_{pore}) was derived from the QSDFT-Ads analysis (N_2 @ 77K; mixed slit/cylindrical kernel) 68

Table 3.3 XPS peak position and full width at half maximum (FWHM) parameters for Mo 3d and B1s of MoB_2/MoB, MoB_2-SP, and MoB_2/B 73

Table 3.4 Composition of the three samples measured from XPS. 73

Table 3.5 Fitted EIS data from Nyquist Plots in **Figure 3.9**.....76

Table 4.1. Composition of the three samples measured from EDS (Fig 4.3 & Fig 4.4) 95

Chapter 1.

Introduction

1.1. An Overview of Hydrogen Energy and Electrocatalysts

Hydrogen is increasingly viewed as a versatile energy vector for decarbonizing hard-to-abate sectors (refining, ammonia, steel, shipping) and for integrating high shares of variable renewables by providing long-duration storage and sector coupling.[1,2] Its role within a net-zero energy system underpins the contemporary "hydrogen economy," with near-term supply and demand growth hinging on scalable low-emission production.[3,4] In this context, electrochemical energy conversion and storage technologies intensify the need for efficient, durable, and earth-abundant catalysts to reduce cost and accelerate deployment.[5]

At present, most hydrogen is generated thermochemically by steam-methane reforming and coal gasification, processes that are CO_2-intensive unless paired with carbon capture.[6] By contrast, water electrolysis—splitting water into H_2 (cathodic hydrogen evolution reaction, HER) and O_2 (anodic oxygen evolution reaction, OER)—offers a clean, flexible route that can be directly coupled to renewable electricity in both PEM and AEM electrolyzers.[5,7,8] Platinum remains the state-of-the-art HER catalyst, and Ir/Ru oxides set acidic-OER benchmarks, but cost and scarcity limit scale-up, motivating discovery of non-precious alternatives.[9,10] Design principles such as the HER volcano based on ΔG_{H^*} and interfacial kinetic effects (especially in alkaline media) guide materials optimization and benchmarking.[11–13]

Intense efforts have yielded noble-metal-free HER catalysts that rival Pt under optimized compositions and microstructures. Transition-metal chalcogenides (e.g., MoS_2) demonstrate edge-site activity and phase/defect engineering routes to high performance.[6,14,15] Transition-metal carbides deliver near-Pt activity when nanoscaled and support-engineered, with trends rationalized by electronic descriptors.[16] Nitrides provide bifunctional pathways and interface-engineered activity across pH.[17–19] Phosphides (e.g., Ni_2P, CoP) are robust, acid-tolerant HER catalysts with well-defined active motifs and scalable architectures.[20–22] Recently, transition-metal borides (TMBs) have garnered attention for combining low cost with high HER activity and stability in both acidic and basic electrolytes, where structure–activity relationships implicate boron frameworks (1D chains, 2D sheets, 3D networks), lattice parameters, and site occupancy in tuning electronic structure and hydrogen adsorption thermodynamics.[23,24] Beyond composition and crystal chemistry, catalytic metrics can be enhanced by nanosizing—achieved via metallic flux (e.g., Sn-assisted) growth, molten-salt routes, and plasma syntheses—together with electronic/defect engineering through doping, substitution, and grain-boundary control; these collective strategies motivate this thesis to elucidate and improve the HER performance of TMB nanoparticles.[25]

1.2. Hydrogen Evolution Reaction (HER)

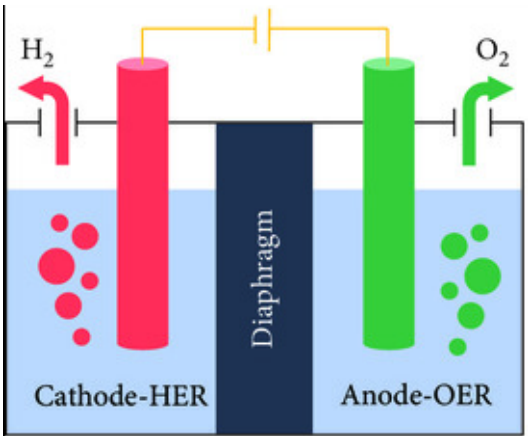

In acidic solution

Cathode: $4H^+ + 4e^- \rightarrow 2H_2$

Anode: $2H_2O \rightarrow O_2 + 4H^+ + 4e^-$

$2H_2O \rightarrow 2O_2 + 2H_2$

In alkaline solution

Cathode: $4H_2O + 4e^- \rightarrow 2H_2 + 4OH^-$

Anode: $4OH^- \rightarrow O_2 + 2H_2O + 4e^-$

$2H_2O \rightarrow 2O_2 + 2H_2$

Figure 1.1. (left) Scheme of water electrolysis system and (right) different reactions in acidic and alkaline solution[26]

Figure 1.1 depicts a two-electrode water-electrolysis cell in which H_2 forms at the negatively charged cathode (HER) and O_2 at the positively charged anode (OER), separated by an ion-conducting diaphragm/membrane that minimizes product crossover while completing the ionic circuit.[26] The overall reaction is $2H_2O \rightarrow 2H_2 + O_2$, whose reversible potential is 1.23 V at 298 K and 1 atm.[27] In practice, a higher cell voltage is required because each elementary cathodic or anodic step must surmount an activation barrier; these kinetic barriers appear experimentally as overpotentials (η) that add to the reversible potential.[27,28] For HER on metals, η reflects the barrier for forming adsorbed hydrogen (Volmer), recombining/desorbing H_2 (Tafel/Heyrovský), and reorganizing the interfacial solvent/ions, so the electrode *material* (and its surface structure) directly controls the needed driving force.[29] Additional voltage is lost to ohmic (iR) drop through electrolyte, separator, and contacts, which can be reduced by design (high conductivity, short ion paths) and corrected during analysis by iR compensation.[30,31] Mass-transport polarization and

bubble coverage at gas-evolving surfaces can further raise the apparent cell voltage; flow fields, porous/rough electrodes, and hydrophobic patterning are commonly used to alleviate these effects.[32–34]

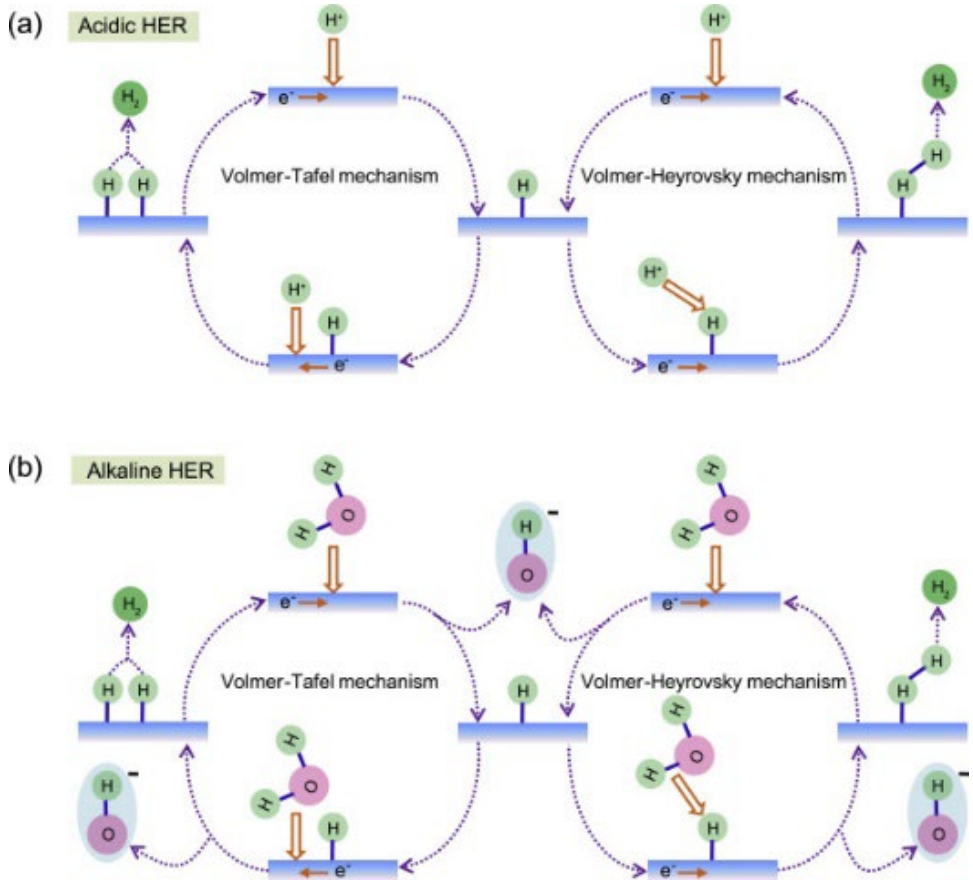

Figure 1.2. HER mechanisms in (a) acidic and (b) alkaline solutions.[35]

The classical HER mechanisms at the cathode are illustrated in **Figure 1.2**. In acidic media (top, **Figure 1.2a**), adsorbed hydrogen (H*) is generated by the electrochemical Volmer step ($H^+ + e^- + M \rightarrow M–H^*$), followed either by chemical recombination of two adsorbates (Tafel: $2M–H^* \rightarrow 2M + H_2$) or by electrochemical desorption (Heyrovský: $M–H^* + H^+ + e^- \rightarrow M + H_2$).[31,35] In alkaline media (bottom, **Figure 1.2b**), the Volmer step

requires *water activation* ($H_2O + e^- + M \rightarrow M–H^* + OH^-$), introducing an additional barrier associated with breaking the O–H bond and reorganizing interfacial water.[36,37] The diagrams also highlight how bifunctional surfaces—e.g., a metal site that binds H* adjacent to an oxide/hydroxide site that facilitates H_2O dissociation—can accelerate the alkaline Volmer step.[38] These pathways leave distinct kinetic signatures: when Volmer is rate-limiting, Tafel slopes approach ~120 mV dec^{-1}; when Tafel controls, ~30 mV dec^{-1}; and when Heyrovský controls, ~40 mV dec^{-1}, assuming ideal transport and minimal series resistance. Thus, **Figure 1.2** links molecular steps to the macroscopic polarization behavior used to benchmark catalysts.[11,39]

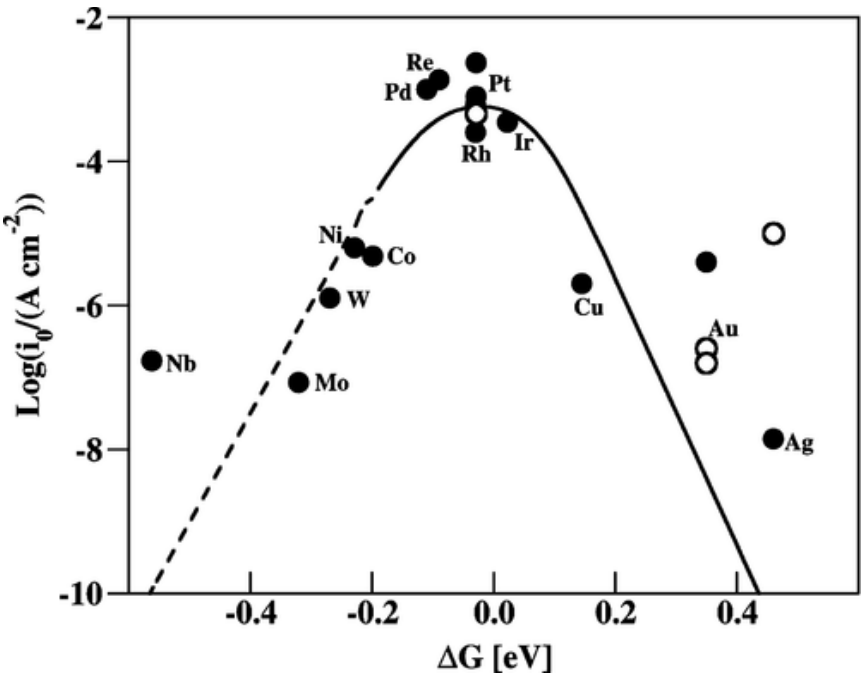

Figure 1.3. HER volcano plot. The data points are measured exchange current density plotted versus the calculated free energy of H adsorption at $U = 0$ V. The metals on the left side of the volcano have high H coverage (1 ML) and the metals on the right side low H coverage (0.25 ML). The line is a prediction by a kinetic model in which all input parameters are taken from DFT calculations.[40]

Figure 1.3 plots exchange current density (log i_0) versus the Gibbs free energy of hydrogen adsorption (ΔG_{H^*}), producing the well-known "volcano" that captures the Sabatier principle for HER.[40] Metals on the left flank ($\Delta G_{H^*} < 0$) bind H* too strongly—adsorption is facile but H_2 release is slow—whereas metals on the right flank ($\Delta G_{H^*} > 0$) bind H* too weakly, limiting H* formation (slow Volmer).[40] The apex near $\Delta G_{H^*} \approx 0$ eV reflects an optimal balance; Pt sits close to this maximum, while base-metal surfaces populate the flanks (e.g., Ni/Co/W/Mo on the strong-binding side; Cu/Au/Ag on the weak-binding side).[41] Practically, one can *draw* a candidate onto the volcano by estimating its ΔG_{H^*} from DFT or spectroscopic surrogates and projecting horizontally to the curve to anticipate an intrinsic i_0 (and, by extension, the overpotential at a given current).[11,40] This mapping is now used broadly—from noble metals to sulfides/carbides/borides—to screen materials and to rationalize why improving alkaline HER often also requires sites that promote water dissociation in parallel with near-thermoneutral H* binding.[42,43]

1.3. Transition Metal Borides (TMBs) and their Nanoparticles

1.3.1 Transition Metal Borides in HER

TMBs span a rich set of crystal chemistries (e.g., AlB_2-type diborides with planar "graphene-like" B layers, and more complex boron nets or chains as shown in **Figure 1.4**) that hybridize metal d-states with B sp-states to create conductive frameworks and tunable hydrogen-binding ensembles.[44,45] These bonding motifs make TMBs an attractive, *designable* class of bulk HER cathodes in which crystal structure (and thus surface-

projected electronic structure) provides levers complementary to those in carbides, nitrides, or phosphides.[23]

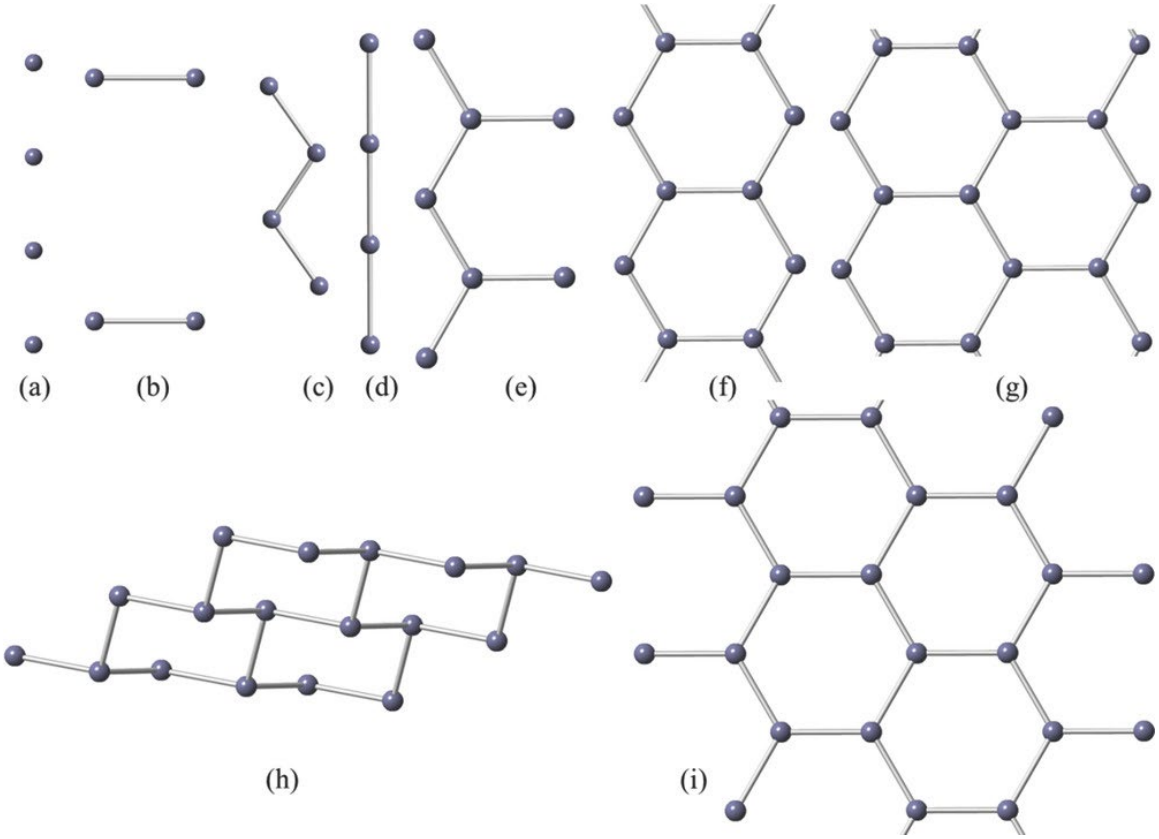

Figure 1.4. Different structures formed by boron atoms in transition metal borides. (a) isolated atomic boron, (b) pairs, (c) zig-zag chains, (d) straight chains, (e) extended chains, (f) double chains, (g) triple chains, (h) corrugated networks, and (i) flat networks of boron atoms.[44]

Within the Mo–B system, phase-resolved studies established a clear boron-content/activity trend for bulk arc-melted phases: MoB_2 and β-MoB exhibit superior HER kinetics and stability, outperforming α-MoB and Mo_2B under acidic testing; these results directly tied structure to activity at identical mass transport and measurement conditions. [46] At the same time, introducing alternating boron sublattices in bulk Mo_2B_4 (graphene-like vs phosphorene-like layers) revealed strikingly different surface activities: DFT and

experiments showed that the graphene-like B layer hosts near-optimal H adsorption, whereas the puckered, phosphorene-like layer is far less active—linking crystallography to site-specific ΔG_{H^*} on a single compound.[47] Together, these two Mo–B exemplars (MoB_2/β-MoB vs Mo_2B_4) demonstrate how boron topology and metal–boron hybridization govern HER in *bulk* borides.

AlB_2-type solid solutions offer a second structural handle. In $Cr_{1-x}Mo_xB_2$, a canonical ("canonic-like") variation of the c-lattice parameter with composition tracks intrinsic HER activity in acid, with a maximum near $x \approx 0.6$; notably, at high current densities the best bulk compositions rival or even surpass Pt/C while retaining robustness. This composition–structure–activity correlation underscores how tuning the metal d-band/B-sp interaction through lattice chemistry can optimize H* binding on extended **bulk** surfaces.[48]

Beyond Mo-based borides, bulk vanadium borides extend the design rules. Systematic measurements showed that HER activity in VB and V_3B_4 scales with boron-chain condensation—a crystallographic descriptor that increases the density and quality of B–B units participating in favorable adsorption ensembles—providing a predictive, structure-aware pathway to select active *bulk* phases before synthesis.[24] A related line on VB_2 with graphene-like B layers reported high bulk activity and durability consistent with DFT-identified active terminations, further supporting the central role of boron topology across chemistries.[49]

Finally, recent work has highlighted an electronic mechanism—antibonding–vacancy coupling in diborides—that boosts HER by aligning metal–boron antibonding

states near the Fermi level and stabilizing surface vacancies to tune ΔG_{H^*}. Although demonstrated alongside redox-flux chemistry, the underlying electronic principle directly concerns *bulk-terminating* AlB_2-type surfaces and offers a route to engineer active sites via controlled non-stoichiometry and defect chemistry in bulk crystals.[50]

1.3.2 TMB Nanoparticles for enhanced HER

Nanostructuring transition-metal borides (TMBs) typically boosts apparent activity by enlarging the electrochemically active surface area (ECSA) and, in favorable cases, shifts intrinsic kinetics by exposing metastable terminations and under-coordinated metal/boron ensembles; however, obtaining crystalline, phase-pure TMB nanoparticles is nontrivial because strong, directional B–B covalency and refractory thermodynamics bias conventional syntheses toward high temperatures (sintering, grain growth) or toward low-temperature borohydride routes that often yield amorphous M–B gels requiring annealing that coarsens particles and mixes phases.[51–53] Solution impurities (e.g., oxygenated boron species) and immiscibility issues further complicate colloidal control relative to oxides or chalcogenides, motivating alternative chemistries such as metal-immiscibility/flux strategies and rapid metathesis routes that can deliver crystalline nanoborides with tunable surfaces.[54,55]

Within this context, the first benchmarks from the Fokwa group established that downsizing MoB_2 to nanoparticles markedly improves HER exhibiting low onset overpotentials (≈154 mV at 10 mA cm^{-2} in 0.5 M H_2SO_4) and Tafel slopes near ~50 mV dec^{-1}, outperforming prior microscale/bulk analogues and revealing that accessible B-terminated facets are catalytically competent.[56] In a companion study, VB_2—whose crystal

structure features graphene-like B layers—was prepared both as bulk and as nanoparticles; DFT and experiments together showed fast HER kinetics and durability over wide pH, with the nanoscale material providing higher geometric activity at matched loading by combining favorable H* binding with rapid charge transport through the B sheets.[49] Methodologically, a general redox route using $Sn/SnCl_2$ (and the immiscibility of Sn with B) provided a versatile way to access crystalline nanoscale borides (3d–5d; multiple Mo–B phases), opening a palette of particle sizes and terminations that could be correlated to HER performance.[57]

Beyond these early exemplars, phase-engineered nanosheets of β-MoB_2 and α-MoB_2 prepared by Liu & Gong via a controllable route showed further improvements in exchange current and η_{10} over bulk, attributed to abundant edge sites and short diffusion paths in the nanosheets.[58,59] Extending to W-borides, AlB_2-type WB_2-191 nanosheets made by a one-step molten-salt synthesis displayed low overpotentials (≈121 mV in acid; ≈147 mV in 1.0 M KOH at 10 mA cm^{-2}) and long-term stability, underscoring that nanostructuring plus the "flat" B layers of the 191 polytype can rival precious-metal benchmarks under practical current densities.[25] As a complementary synthetic advance (useful for catalyst libraries), rapid solid-state metathesis has produced crystalline Fe/Co/Ni monoboride nanoparticles that function as bifunctional water-splitting catalysts, highlighting a scalable path to phase-pure nanoborides without severe sintering.[55] Finally, recent colloidal work now achieves phase-pure Ni_2B/Ni_3B nanocrystals under 400 °C, explicitly documenting how oxygenated boron shells can form and be managed—practical guidance that also applies to late-transition-metal borides pursued for HER.[54]

Heterostructuring at the nanoscale further elevates TMB performance by combining *fast H adsorption sites** with adjacent promoters that accelerate interfacial water dissociation (critical in alkaline electrolytes). Co_2B/MoB_2 heterostructured nanoclusters prepared by molten-salt electrochemistry show pH-universal activity and small Tafel slopes, with DFT attributing rate gains to interfacial charge redistribution and optimized ΔG_{H^*}.[60] A Mo–Ru–B nano-heterostructure synthesized by molten-salt assisted routes exhibits reduced overpotentials and excellent durability, consistent with a bifunctional mechanism in which boride domains modulate H binding while Ru-rich sites aid Volmer kinetics in base.[61] Related studies on Ni_3B/MoB nanosheets with grain-boundary-rich heterointerfaces—and, separately, deliberate MoB–Ni_3B interfaces—demonstrate that interfacial band alignment and strain optimize ΔG_{H^*} and lower charge-transfer resistance, delivering high intrinsic activities in both acid and base.[62,63]

Lastly, looking ahead to Chapter 2, vanadium-stabilized MoB nanoparticles ($V_{0.3}Mo_{0.7}B$) were synthesized with $Sn/SnCl_2$-redox method that maintain near-thermoneutral H-binding while preserving nanoscale morphology at high current densities; notably, these nanoparticles sustain industry-relevant rates with limited η growth and robust stability, an observation we revisit in Chapter 2 with a detailed structure–property analysis.[64]

1.4. Synthesis Method

A central synthesis in this work follows Jothi et al. (UCR), who introduced a simple, general route to nanoscale TMBs by exploiting the immiscibility of Sn and B: metallic Sn acts simultaneously as a solvent/flux and as a redox partner (with $SnCl_2$), driving boridation of early transition metals at relatively low temperatures while inhibiting boron loss and suppressing coarsening.[57]

All the chemicals used in the experiment were handled in a nitrogen-filled glovebox. Anhydrous metal sources (Ch.2: $MoCl_5$, VCl_3; Ch.3: $MoCl_5$, Ch.4: $RuCl_3$, RuI_3), elemental boron, and Sn powder (Ch.4: KCl for RuI_3) were mixed in a mortar and pressed into a pellet in the glovebox. The pellet was then sealed in a quartz ampoule under vacuum or argon atmosphere. Different molar ratios of metal sources:B:Sn were used for different samples. The sealed quartz ampoule containing the pellet was then heated in an electric furnace for target time at target temperature. Upon completion of the reaction, the ampoule was opened to reveal a dark-colored product (pellet, powder for Ch.4), which was then ground into powder and treated in approximately 10% concentrated HCl until all the side phases dissolved or removed, then washed with deionized water and ethanol, then dried overnight at 65°C. X-ray diffraction analysis was done for the resulting powder.

1.5. Characterization Techniques

1.5.1 Powder X-ray diffraction(PXRD)

Ch.2: PXRD measurements were performed using Rigaku Miniflex-600 (Japan). The scanning voltage was 40 kV, and the scanning current was 15 mA which was generated by Cu K_α radiation (λ=1.5418 Å).

Ch.3,4: PXRD measurements were performed using Malvern PANalytical Empyrean Series 2 to analyze the crystallinity and composition of the samples. The scanning voltage was 40 kV, and the scanning current was 40 mA which was generated Cu K_α radiation (λ=1.54056 Å).

The recorded PXRD patterns were refined using the Rietveld method as carried out in the PDXL 2 software (Rigaku), along with preferred orientation analysis. The crystal phases information was certified by the standard ICSD database.

1.5.2 X-ray photoelectron spectroscopy (XPS)

The XPS spectrum was recorded using a Kratos AXIS ULTRA ^{DLD} XPS (Japan) system equipped with a monochromated Al Kα X-ray source and a 165 mm mean radius hemispherical electron energy analyzer. The XPS was used to interrogate surface composition/oxidation states and boride vs oxide/borate signatures with contemporary fitting protocols for transition-metal and boron core levels.[65,66]

1.5.3 SEM, EDS, TEM, and STEM

Scanning electron microscopy (SEM), Energy dispersive X-ray spectroscopy (EDS) were used to characterize the surface morphology and mapping images using Nova NanoSEM450 (Japan), equipped with a 50 mm^2 X-Max50 SD EDX detector.

Transmission electron microscopy (TEM) / Scanning transmission electron microscopy (STEM) were used to take the images and measure corresponding selected area electron diffraction patterns with JEM-ARM200F (JEOL Ltd., Japan), operated at 200 kV.

Electron microscopy (SEM/TEM/STEM) provided morphology, particle-size distributions, and interplanar spacings, complemented by EDS for qualitative compositional mapping.

1.5.4 Brunauer-Emmett-Teller (BET)

Specific surface areas were determined by N_2 physisorption and BET analysis to support ECSA normalization and to decouple geometric from intrinsic activity.[67] The N_2 adsorption-desorption isotherms were collected at 77 K on an Anton Paar NOVA 800. Samples were outgassed under vacuum at 100 °C for 6 h (ramp 5 °C min^{-1}); free space was determined with He prior to adsorption. The Brunauer-Emmett-Teller (BET) specific surface areas were calculated from the adsorption branch using the Rouquerol criteria (σN_2 = 0.162 nm^2). Pore-size distributions were obtained in Kaomi using a QSDFT adsorption kernel for N_2 at 77 K with a mixed slit/cylindrical pore model (N_2 @ 77 K on carbon, slit/cyl. pore, QSDFT Ads.").

1.5.5 Electrochemical characterization

The electrochemical tests of the samples were carried out on a VSP electrochemical workstation (Bio-Logic Science Instruments, France) using a three-electrode system: prepared electrode of our sample as a working electrode, graphite rod and saturated calomel electrode (SCE) as the counter and reference electrodes, respectively, in 0.5 M H_2SO_4 electrolyte solution. All the potentials are translated into the reversible hydrogen electrode

(RHE) according to the equation: $E_{RHE} = E_{SCE} + 0.242\ V + 0.059 \times pH$. All the measurements were obtained by *iR*-drop compensation. Linear sweep voltammetry (LSV) plots were used to measure electrochemical HER activity with a scan rate of 5 mV/s in the potential range of -1.0 to 0 V vs. SCE. It was recorded after 10 cycles of cyclic voltammetry (CV) tests in the potential range of -1.0 to 0 V to stabilize the current. The Tafel equation $\eta = b\ log\ j + a$ (where j is the current density, b is the Tafel slope, and a is the intercept relative to the exchange current density j_0) was used to calculate the Tafel slopes by fitting the linear part of the Tafel plots. Electrochemical impedance spectroscopy (EIS) was conducted at the overpotential corresponding to -10 mA cm^{-2} current density by applying an AC voltage over the frequency range from 500 kHz to 100 mHz with an amplitude of 10 mV versus the open-circuit potential. The electrochemically active surface area (ECSA) was estimated from CV tests using different scan rates within a non-faradaic reaction region. The double-layer capacitance, $C_{dl,}$ was obtained from the slope of $\Delta J = (J_a - J_c)$ vs the scan rate.

1.6.References

1. Staffell, I.; Scamman, D.; Velazquez Abad, A.; Balcombe, P.; Dodds, P. E.; Ekins, P.; Shah, N.; Ward, K. R., The role of hydrogen and fuel cells in the global energy system., *Energy and Environmental Science*, **2019**, *12*, (2), 463–491.
2. Lewis, N. S.; Nocera, D. G., Powering the planet: Chemical challenges in solar energy utilization., *Proceedings of the National Academy of Sciences*, **2006**, *103*, (43), 15729–15735.
3. Turner, J. A., Sustainable Hydrogen Production., *Science (1979)*, **2004**, *305*, (5686), 972–974.
4. Energy Agency, I., *Global Hydrogen Review 2024*., **2024**,.
5. Roger, I.; Shipman, M. A.; Symes, M. D., Earth-abundant catalysts for electrochemical and photoelectrochemical water splitting., *Nat Rev Chem*, **2017**, *1*, 1–13.
6. Dincer, I.; Acar, C., Review and evaluation of hydrogen production methods for better sustainability., *Int J Hydrogen Energy*, **2014**, *40*, (34), 11094–11111.
7. Carmo, M.; Fritz, D. L.; Mergel, J.; Stolten, D., A comprehensive review on PEM water electrolysis., *International Journal of Hydrogen Energy*, **2013**, *38*, (12), 4901–4934.
8. Du, N.; Roy, C.; Peach, R.; Turnbull, M.; Thiele, S.; Bock, C., Anion-Exchange Membrane Water Electrolyzers., *Chemical Reviews*, **2022**, *122*, (13), 11830–11895.
9. Hansen, J. N.; Prats, H.; Toudahl, K. K.; Mørch Secher, N.; Chan, K.; Kibsgaard, J.; Chorkendorff, I., Is There Anything Better than Pt for HER?, *ACS Energy Lett*, **2021**, *6*, (4), 1175–1180.
10. Seitz, L. C.; Dickens, C. F.; Nishio, K.; Hikita, Y.; Montoya, J.; Doyle, A.; Kirk, C.; Vojvodic, A.; Hwang, H. Y.; Norskov, J. K.; Jaramillo, T. F., A highly active and stable IrO_x /$SrIrO_3$ catalyst for the oxygen evolution reaction., *Science (1979)*, **2016**, *353*, (6303), 1011–1014.
11. Nørskov, J. K.; Bligaard, T.; Logadottir, A.; Kitchin, J. R.; Chen, J. G.; Pandelov, S.; Stimming, U., Trends in the Exchange Current for Hydrogen Evolution., *J Electrochem Soc*, **2005**, *152*, (3), J23.
12. Danilovic, N.; Subbaraman, R. A. M.; Strmcnik, D., Electrocatalysis of the HER in acid and alkaline media., *Journal of the Serbian Chemical Society*, **2013**, *78*, (12), 2007–2015.
13. Ledezma-Yanez, I.; Wallace, W. D. Z.; Sebastián-Pascual, P.; Climent, V.; Feliu, J. M.; Koper, M. T. M., Interfacial water reorganization as a pH-dependent descriptor of the hydrogen evolution rate on platinum electrodes., *Nat Energy*, **2017**, *2*, (4).

14. Hinnemann, B.; Moses, P. G.; Bonde, J.; Jørgensen, K. P.; Nielsen, J. H.; Horch, S.; Chorkendorff, I.; Nørskov, J. K., Biomimetic hydrogen evolution: MoS2 nanoparticles as catalyst for hydrogen evolution., *J Am Chem Soc*, **2005**, *127*, (15), 5308–5309.

15. T. F. Jaramillo; K. P. Jørgensen; J. Bonde; J. H. Nielsen; S. Horch; I. Chorkendorff, Identification of Active Edge Sites for Electrochemical H2 Evolution from MoS2 Nanocatalysts., *Science (1979)*, **2007**, *317*, (5834), 100–102.

16. Michalsky, R.; Zhang, Y. J.; Peterson, A. A., Trends in the hydrogen evolution activity of metal carbide catalysts., *ACS Catal*, **2014**, *4*, (5), 1274–1278.

17. Chen, W. F.; Muckerman, J. T.; Fujita, E., Recent developments in transition metal carbides and nitrides as hydrogen evolution electrocatalysts., *Chemical Communications*, **2013**, *49*, (79), 8896–8909.

18. Lu, B.; Guo, L.; Wu, F.; Peng, Y.; Lu, J. E.; Smart, T. J.; Wang, N.; Finfrock, Y. Z.; Morris, D.; Zhang, P.; Li, N.; Gao, P.; Ping, Y.; Chen, S., Ruthenium atomically dispersed in carbon outperforms platinum toward hydrogen evolution in alkaline media., *Nat Commun*, **2019**, *10*, (1).

19. Song, F.; Li, W.; Yang, J.; Han, G.; Liao, P.; Sun, Y., Interfacing nickel nitride and nickel boosts both electrocatalytic hydrogen evolution and oxidation reactions., *Nat Commun*, **2018**, *9*, (1).

20. Popczun, E. J.; McKone, J. R.; Read, C. G.; Biacchi, A. J.; Wiltrout, A. M.; Lewis, N. S.; Schaak, R. E., Nanostructured nickel phosphide as an electrocatalyst for the hydrogen evolution reaction., *J Am Chem Soc*, **2013**, *135*, (25), 9267–9270.

21. Tian, J.; Liu, Q.; Asiri, A. M.; Sun, X., Self-supported nanoporous cobalt phosphide nanowire arrays: An efficient 3D hydrogen-evolving cathode over the wide range of pH 0-14., *J Am Chem Soc*, **2014**, *136*, (21), 7587–7590.

22. Stern, L. A.; Feng, L.; Song, F.; Hu, X., Ni2P as a Janus catalyst for water splitting: The oxygen evolution activity of Ni2P nanoparticles., *Energy Environ Sci*, **2015**, *8*, (8), 2347–2351.

23. Lee, E.; Fokwa, B. P. T., Nonprecious Metal Borides: Emerging Electrocatalysts for Hydrogen Production., *Acc Chem Res*, **2022**, *55*, (1), 56–64.

24. Lee, E.; Park, H.; Joo, H.; Fokwa, B. P. T., Unexpected Correlation Between Boron Chain Condensation and Hydrogen Evolution Reaction (HER) Activity in Highly Active Vanadium Borides: Enabling Predictions., *Angewandte Chemie - International Edition*, **2020**, *59*, (29), 11774–11778.

25. Liu, X.; Cao, M.; Wen, J.; Gong, Y., Facile Synthesis of Tungsten Diboride (WB2-191) in Molten Salt and Its Hydrogen Evolution Performance in Acidic and Alkaline Media., *ACS Sustain Chem Eng*, **2024**, *12*, (48), 17460–17467.

26. Wan, X.; Song, Y.; Zhou, H.; Shao, M., Layered Double Hydroxides for Oxygen Evolution Reaction towards Efficient Hydrogen Generation., *Energy Material Advances*, **2022**, *2022*.

27. Koper, M. T. M., Thermodynamic theory of multi-electron transfer reactions: Implications for electrocatalysis., *Journal of Electroanalytical Chemistry*, **2011**, *660*, (2), 254–260.

28. Trasatti, S., Work function, electronegativity, and electrochemical behaviour of metals., *J Electroanal Chem Interfacial Electrochem*, **1971**, *33*, (2), 351–378.

29. Markovic, N. M.; Ross, P. N., Surface science studies of model fuel cell electrocatalysts., *Surf Sci Rep*, **2002**, *45*, (4–6), 117–229.

30. Zheng, W., *iR* Compensation for Electrocatalysis Studies: Considerations and Recommendations., *ACS Energy Lett*, **2023**, *8*, (4), 1952–1958.

31. Conway, B. E.; Tilak, B. V., Interfacial processes involving electrocatalytic evolution and oxidation of H2, and the role of chemisorbed H., *Electrochim Acta*, **2002**, *47*, (22–23), 3571–3594.

32. Xu, W.; Lu, Z.; Sun, X.; Jiang, L.; Duan, X., Superwetting Electrodes for Gas-Involving Electrocatalysis., *Acc Chem Res*, **2018**, *51*, (7), 1590–1598.

33. Angulo, A.; van der Linde, P.; Gardeniers, H.; Modestino, M.; Fernández Rivas, D., Influence of Bubbles on the Energy Conversion Efficiency of Electrochemical Reactors., *Joule*, **2020**, *4*, (3), 555–579.

34. Vogt, H.; Balzer, R. J., The bubble coverage of gas-evolving electrodes in stagnant electrolytes., *Electrochim Acta*, **2005**, *50*, (10), 2073–2079.

35. Zhang, S.; Zhang, X.; Rui, Y.; Wang, R.; Li, X., Recent advances in non-precious metal electrocatalysts for pH-universal hydrogen evolution reaction., *Green Energy and Environment*, **2021**, *6*, (4), 458–478.

36. Sheng, W.; Myint, M.; Chen, J. G.; Yan, Y., Correlating the hydrogen evolution reaction activity in alkaline electrolytes with the hydrogen binding energy on monometallic surfaces., *Energy Environ Sci*, **2013**, *6*, (5), 1509.

37. Parsons, R., The rate of electrolytic hydrogen evolution and the heat of adsorption of hydrogen., *Transactions of the Faraday Society*, **1958**, *54*, 1053.

38. Shinagawa, T.; Garcia-Esparza, A. T.; Takanabe, K., Insight on Tafel slopes from a microkinetic analysis of aqueous electrocatalysis for energy conversion., *Sci Rep*, **2015**, *5*.

39. Durst, J.; Siebel, A.; Simon, C.; Hasché, F.; Herranz, J.; Gasteiger, H. A., New insights into the electrochemical hydrogen oxidation and evolution reaction mechanism., *Energy Environ Sci*, **2014**, *7*, (7), 2255–2260.

40. Skúlason, E.; Tripkovic, V.; Björketun, M. E.; Gudmundsdóttir, S.; Karlberg, G.; Rossmeisl, J.; Bligaard, T.; Jónsson, H.; Nørskov, J. K., Modeling the

Electrochemical Hydrogen Oxidation and Evolution Reactions on the Basis of Density Functional Theory Calculations., *The Journal of Physical Chemistry C*, **2010**, *114*, (42), 18182–18197.

41. Greeley, J.; Jaramillo, T. F.; Bonde, J.; Chorkendorff, I.; Nørskov, J. K., Computational high-throughput screening of electrocatalytic materials for hydrogen evolution., *Nat Mater*, **2006**, *5*, (11), 909–913.
42. Kibsgaard, J.; Jaramillo, T. F.; Besenbacher, F., Building an appropriate active-site motif into a hydrogen-evolution catalyst with thiomolybdate [Mo3S13]2− clusters., *Nat Chem*, **2014**, *6*, (3), 248–253.
43. Voiry, D.; Chhowalla, M.; Gogotsi, Y.; Kotov, N. A.; Li, Y.; Penner, R. M.; Schaak, R. E.; Weiss, P. S., Best Practices for Reporting Electrocatalytic Performance of Nanomaterials., *ACS Nano*, **2018**, *12*, (10), 9635–9638.
44. Akopov, G.; Yeung, M. T.; Kaner, R. B., Rediscovering the Crystal Chemistry of Borides., *Advanced Materials*, **2017**, *29*, (21).
45. Lee, E.; Fokwa, B. P. T., Nonprecious Metal Borides: Emerging Electrocatalysts for Hydrogen Production., *Acc Chem Res*, **2022**, *55*, (1), 56–64.
46. Park, H.; Encinas, A.; Scheifers, J. P.; Zhang, Y.; Fokwa, B. P. T., Boron-Dependency of Molybdenum Boride Electrocatalysts for the Hydrogen Evolution Reaction., *Angewandte Chemie - International Edition*, **2017**, *56*, (20), 5575–5578.
47. Park, H.; Zhang, Y.; Scheifers, J. P.; Jothi, P. R.; Encinas, A.; Fokwa, B. P. T., Graphene-and Phosphorene-like Boron Layers with Contrasting Activities in Highly Active Mo2B4 for Hydrogen Evolution., *J Am Chem Soc*, **2017**, *139*, (37), 12915–12918.
48. Park, H.; Lee, E.; Lei, M.; Joo, H.; Coh, S.; Fokwa, B. P. T., Canonic-Like HER Activity of Cr1–xMoxB2 Solid Solution: Overpowering Pt/C at High Current Density., *Advanced Materials*, **2020**, *32*, (28).
49. Jothi, P. R.; Zhang, Y.; Yubuta, K.; Culver, D. B.; Conley, M.; Fokwa, B. P. T., Abundant vanadium diboride with graphene-like boron layers for hydrogen evolution., *ACS Appl Energy Mater*, **2019**, *2*, (1), 176–181.
50. Lee, E.; Yapo, J. A.; Bhupathy, A.; Mentzel, T. S.; Yin, X.; Adeniji, S. E.; Kim, S. B.; Fokwa, B. P. T., Antibonding–Vacancy Coupling Boosts Hydrogen Evolution Rate in Diborides., *ACS Energy Lett*, **2025**, 4560–4566.
51. Hong, J.; Mutalik, S.; Pescarmona, P. P.; Protesescu, L., Metal Borides: From Industrial Classics to Versatile Colloidal Nanocrystals for Energy, Catalysis, and Hard Coatings Applications†., *Chemistry of Materials*, **2024**, *36*, (5), 2147–2164.
52. Chen, H.; Zou, X., Intermetallic borides: Structures, synthesis and applications in electrocatalysis., *Inorg Chem Front*, **2020**, *7*, (11), 2248–2264.

53. Glavee, G. N.; Klabunde, K. J.; Sorensen, C. M.; Hadjapanayis, G. C., Borohydride reductions of metal ions. A new understanding of the chemistry leading to nanoscale particles of metals, borides, and metal borates., *Langmuir*, **1992**, *8*, (3), 771–773.

54. Hong, J.; Mutalik, S.; Miola, M.; Gerlach, D.; Mehrabi K., R.; Ahmadi, M.; Kooi, B. J.; Portale, G.; Rudolf, P.; Pescarmona, P. P.; Protesescu, L., Nickel Boride (Ni_xB) Nanocrystals: From Solid-State Synthesis to Highly Colloidally Stable Inks., *Chemistry of Materials*, **2023**, *35*, (4), 1710–1722.

55. Abeysinghe, J. P.; Kölln, A. F.; Gillan, E. G., Rapid and Energetic Solid-State Metathesis Reactions for Iron, Cobalt, and Nickel Boride Formation and Their Investigation as Bifunctional Water Splitting Electrocatalysts., *ACS Materials Au*, **2022**, *2*, (4), 489–504.

56. Jothi, P. R.; Zhang, Y.; Scheifers, J. P.; Park, H.; Fokwa, B. P. T., Molybdenum diboride nanoparticles as a highly efficient electrocatalyst for the hydrogen evolution reaction., *Sustain Energy Fuels*, **2017**, *1*, (9), 1928–1934.

57. Jothi, P. R.; Yubuta, K.; Fokwa, B. P. T., A Simple, General Synthetic Route toward Nanoscale Transition Metal Borides., *Adv Mater*, **2018**, *30*, (14), 2–7.

58. Liu, X.; Gong, Y., A Simple Molten Salt Route to Crystalline β-MoB2Nanosheets with High Activity for the Hydrogen Evolution Reaction., *Inorg Chem*, **2021**, *60*, (23), 18075–18081.

59. Liu, X.; Gong, Y., α-MoB2Nanosheets for Hydrogen Evolution in Alkaline and Acidic Media., *ACS Appl Nano Mater*, **2022**, *5*, (8), 10183–10191.

60. Liu, X.; Yao, Y.; Li, W.; Zhang, Y.; Liu, Z.; Yin, H.; Wang, D., Molten-Salt Electrochemical Preparation of Co_2B/MoB_2 Heterostructured Nanoclusters for Boosted pH-Universal Hydrogen Evolution., *Small*, **2024**, *20*, (18).

61. Yang, P.; Zhou, B.; Wang, J.; Wang, Y.; Chen, Z.; Wang, X.; Wang, L.; Liu, F.; Wu, Z., Molten salt assisted to synthesize molybdenum–ruthenium boride for hydrogen generation in wide pH range., *Int J Hydrogen Energy*, **2023**, *48*, (57), 21568–21577.

62. Jiang, L.; Wang, R.; Zhang, D.; Wei, G.-F.; Wang, X., Modulate the surface charge toward efficient hydrogen evolution reaction: Electronic structure engineering of MoB-Ni3B interface., *Chemical Engineering Journal*, **2024**, *485*, 149920.

63. Huang, H.; Jung, H.; Jun, H.; Woo, D. Y.; Han, J. W.; Lee, J., Design of grain boundary enriched bimetallic borides for enhanced hydrogen evolution reaction., *Chemical Engineering Journal*, **2021**, *405*, 126977.

64. Kim, S. B.; Yapo, J. A.; Yasuhara, A.; Yubuta, K.; Fokwa, B. P. T., Vanadium-Stabilized MoB Nanoparticles Enable Hydrogen Evolution at Industry-Relevant High Current Densities., *Small*, **2025**,.

65. Biesinger, M. C., Advanced analysis of copper X-ray photoelectron spectra., *Surface and Interface Analysis*, **2017**, *49*, (13), 1325–1334.

66. Silversmit, G.; Depla, D.; Poelman, H.; Marin, G. B.; De Gryse, R., Determination of the V2p XPS binding energies for different vanadium oxidation states (V5+ to V0+)., *J Electron Spectros Relat Phenomena*, **2004**, *135*, (2–3), 167–175.

67. Brunauer, S.; Emmett, P. H.; Teller, E., Adsorption of Gases in Multimolecular Layers., *J Am Chem Soc*, **1938**, *60*, (2), 309–319.

Chapter 2.

Vanadium-Stabilized MoB Nanoparticles Enable Hydrogen Evolution at Industry-Relevant High Current Densities

Sang Bum Kim, Johan A. Yapo, Akira Yasuhara, Kunio Yubuta, Boniface P.T. Fokwa

Bulk molybdenum boride electrocatalysts have emerged as cost-effective alternatives to platinum-based catalysts toward the hydrogen evolution reaction (HER), particularly under harsh industrial conditions requiring high current densities. However, differences in electrode preparation methods between molybdenum borides and Pt/C thus complicate direct activity comparison. In this study, vanadium-stabilized molybdenum monoboride ($V_{0.3}Mo_{0.7}B$) nanoparticles are synthesized and shown to outperform Pt/C at industrially relevant current densities under the same experimental conditions, achieving 1000 mA cm^{-2} with an overpotential of just 0.452 V compared to 0.837 V for Pt/C. Our density functional theory (DFT) calculations demonstrate that $V_{0.31}Mo_{0.69}B$ exhibits improved Gibbs free energy for HER (ΔG_H = -0.12 eV) at high hydrogen coverages (80 to 100%), showcasing its superior catalytic activity at high current densities. Stability tests demonstrate that the $V_{0.3}Mo_{0.7}B$ electrode retains 97% of its performance after ≈28 h of operation at 1000 mA cm^{-2}, positioning it as a compelling candidate for sustainable hydrogen production.

S. B. Kim, J. A. Yapo, A. Yasuhara, K. Yubuta, B. P.T. Fokwa, ***Small 2025, 21, 2412693 (****10.1002/smll.202412693)*

2.1. Introduction

The hydrogen evolution reaction (HER) in electrochemical water splitting is one of the most promising pathways for clean hydrogen production. As global demand for sustainable energy continues to rise, there is an increasing need for highly efficient, durable, and cost-effective electrocatalysts to facilitate this reaction.[1] Although platinum-based materials have been the benchmark catalysts due to their excellent performance, their high cost and scarcity have driven research toward alternative catalytic materials based on non-noble metals.[2,3] The challenge lies in designing these cost-effective materials while maintaining or improving catalytic efficiency and durability at the high current densities required for industrial applications.[4] Among the various materials being studied, molybdenum-based catalysts are recognized for their efficiency in the HER, presenting a cost-effective alternative to platinum-based materials.[5] These catalysts—including molybdenum carbides, nitrides, borides, sulfides, and phosphides[6–11]—exhibit high activity and stability across a wide range of pH conditions, enhancing their viability for sustainable hydrogen production.[12] Specifically, the mechanism of MoS_2 has been extensively studied, revealing unique edge sites that facilitate hydrogen adsorption and desorption, a critical aspect of effective catalytic action.[13] Defects, such as vacancies or heteroatom doping, in molybdenum-based catalysts, have been widely investigated and found to significantly modulate the electronic structure of the catalysts, thereby increasing their active sites and enhancing catalytic activity.[14–19] This aspect of defect engineering is vital for optimizing the performance of molybdenum-based catalysts in the hydrogen evolution reaction.

Additionally, morphology changes[20] and heteroatom doping[21,22] have been shown to influence catalytic performance.

Transition metal borides (TMBs) have emerged as a promising class of catalysts for the HER due to their excellent catalytic activity and stability in both acidic and alkaline electrolytes.[23,24] Among the most studied TMBs for HER applications are the molybdenum-based borides. Studies have explored the trend of boron dependency by synthesizing and testing Mo_2B, MoB, and MoB_2 for HER, with MoB_2—containing the highest boron content—exhibiting the greatest activity.[25]

Additionally, the flat hexagonal boron layer has been identified as the most effective catalytic surface in molybdenum diborides.[26] Subsequent studies on elemental substitutions in AlB_2-type compounds aimed to enhance catalytic activity while preserving the flat boron layer. For example, substituting 40% Cr into MoB_2 produced the most active material,[27] while substituting 30% W into MoB_2 also improved its activity.[28] Furthermore, strong hybridization between the d-orbitals of transition metals (TMs) and the sp-orbitals of boron has been shown to significantly enhance the HER catalytic activity of TMBs.[29] Combining TMBs with semiconducting materials has opened another avenue for designing Mott–Schottky catalysts, which exhibit exceptional HER activity due to their unique charge redistribution properties. For instance, the combination of MoB and graphitic carbon nitride (g-C_3N_4) as a Schottky catalyst induces charge redistribution across the interface, increasing the local electron density on the MoB surface. This enhancement boosts HER performance by lowering the kinetic barriers to proton adsorption and reduction.[30] Similarly, TiB_2 encapsulated with polypyrrole (PPy), which serves as a Mott-

Schottky center, facilitated electron transfer and improved the HER catalytic performance of TiB_2 by reducing overpotential and increasing the number of active sites.[31] These approaches have proven effective in enhancing both the activity and durability of the catalysts, offering promising alternatives to traditional noble metal-based catalysts.

While the above studies have primarily utilized bulk materials, the activity of TMBs could be further improved by reducing their particle size to maximize the exposure of the catalytic surface area. For example, the formation of α-MoB_2 nanoparticles through solid-state metathesis (SSM) highlighted the potential of TMBs as HER catalysts at the nanoscale.[32] However, boron's high melting point (≈2200 °C) poses significant challenges for producing dispersed nanoparticles, as the reaction requires high temperatures and prolonged reaction times. This often results in large particle sizes, uncontrolled crystallization, and mixed-phase products.[26,33] A major challenge in synthesizing TMB nanoparticles is the need for an excess of boron in the feed. Despite significant efforts, synthesizing nanomaterials such as MoB, MoB_2, and Mo_2B has required excess boron, leading to the presence of amorphous boron as a side phase.[32,34] For instance, a Mo:B ratio of 1:2 was necessary for MoB using the $Sn/SnCl_2$ redox method,[34,35] while ratios of 1:8 and 1:4 were required for MoB_2 using the $Sn/SnCl_2$ redox and solid-state metathesis methods, respectively.[32,34] Similarly, molten salt methods required Mo:B ratio of 1:5 for β-MoB and 1:4 for α-MoB.[36,37] Although this excess boron is not always necessary for all TMBs—an exception being VB_2[38]—other early transition metal borides, such as NbB_2 and its ternary boride solid solutions, still face this issue.[39–41] The excess boron forms an amorphous boron layer on the particles, which cannot be removed by any known method.

This layer hinders particle conductivity and limits the exposure of active catalytic sites on the surface, ultimately reducing catalytic performance.[42]

Although significant breakthroughs in HER electrocatalysts have been reported over the past decade, most evaluations have been conducted at relatively low current densities, typically between 10 and 100 mA cm^{-2}. In contrast, industrial-scale hydrogen production demands electrocatalysts that can operate efficiently at much higher current densities, often exceeding 1000 mA cm^{-2}.[43,44] Moreover, durability is a critical factor in maintaining long-term catalytic performance under these conditions. As a result, recent research has increasingly focused on developing electrocatalysts that are not only efficient and cost-effective but also capable of sustaining high activity at large current densities. For example, TMB-based bulk HER electrocatalysts, such as bulk $Cr_{0.4}Mo_{0.6}B_2$, have been reported to perform at 800 mA cm^{-2},[27] and high-pressure-synthesized bulk α-MoB_2 has demonstrated activity and stability beyond 1000 mA cm^{-2}.[45] However, to the best of our knowledge, reports of TMB nanoparticles capable of operating at such high current densities are lacking.

In this study, we successfully synthesized and characterized a single-phase α-MoB by incorporating vanadium into the α-MoB structure, yielding α-$V_{0.3}Mo_{0.7}B$ (thereafter referred to as $V_{0.3}Mo_{0.7}B$) nanoparticles. The substitution of vanadium enabled synthesis under milder reaction conditions, which facilitated the formation of smaller particles and crystallite sizes, while maintaining a stoichiometric amount of boron in the feed. This approach minimized the formation of an amorphous boron layer on the particle surfaces, thereby enhancing catalytic performance. The experimentally observed outperformance of

the benchmark Pt/C at high current densities was further corroborated by density functional theory (DFT) calculations at high hydrogen coverages.

2.2. Experimental Section

2.2.1. Chemicals

Vanadium Chloride (VCl_3, powder, 99 %), Molybdenum Chloride ($MoCl_5$, powder, 99.95 %), boron (amorphous powder, 99 %) and Platinum on carbon (Pt/C, 20 %) were obtained from Alfa Aesar. Sulfuric acid (H_2SO_4, 98 %) was purchased from Fisher Scientific. Copper sheet and conductive carbon glue were obtained from Basic copper, Ted pella, respectively. All chemicals were used without further purification.

2.2.2. Sample Preparation

All the chemicals used in the experiment were handled in a nitrogen-filled glovebox. Anhydrous metal sources ($MoCl_5$, VCl_3), elemental boron, and Sn powder were mixed in a mortar and pressed into a pellet in the glovebox. The pellet was then sealed in a quartz ampoule under vacuum or argon atmosphere. Different mole compositions (VCl_3:$MoCl_5$:B:Sn) used for different samples, specifically 0.3:0.7:1:2.0 for $V_{0.3}Mo_{0.7}B$, 0:1:1:2.0 for MoB/Mo, 0:1:2:2.5 for MoB/B. The sealed quartz ampoule containing the pellet was then heated in an electric furnace for 4 hours at 800°C for $V_{0.3}Mo_{0.7}B$ and MoB/Mo, and for 8 hours at 900°C for MoB/B with 20°C/min initial heating rate and quenching afterwards. Upon completion of the reaction, the ampoule was opened to reveal a dark-colored product (pellet), which was then ground into powder and treated in approximately 10% concentrated HCl for one hour before washed with deionized water

and ethanol, then dried overnight at 65°C. X-ray diffraction analysis confirmed that the resulting powder of $V_{0.3}Mo_{0.7}B$, MoB/B exhibited a single crystalline phase (space group $I4_1/amd$, ICSD no. 9008953), while MoB/Mo displayed a secondary phase of Mo.

2.2.3. Electrode Preparation

1 mg of each synthesized powder or the commercial 20% Pt/C powder was ultrasonically dispersed in 95 µl ethanol and 5 µl Nafion solution (Sigma Aldrich) for 30 min to form a homogeneous catalyst slurry. Then the slurry catalyst mixture (9 µl or 0.09 mg) was coated over a carbon cloth (Sigracet) with an area of 0.3×0.3 cm^2. Finally, the catalyst-coated carbon cloth was dried at 70 °C for 120 minutes in hot air oven to remove the solvent from the electrode and to improve the bonding. Then the catalyst coated carbon cloth was attached to a copper sheet using conductive silver paste. The exposed surface of the copper sheet was covered with epoxy adhesive and dried overnight at room temperature. The catalyst loading of the electrode was kept at ~1 mg/cm^2 for all the samples analyzed.

2.3. Computational Details

Density functional theory (DFT) calculations were applied to evaluate the Hydrogen surface binding energy (ΔE_H) for MoB and $V_{0.31}Mo_{0.69}B$ {112} surfaces. Total energy calculations were performed using the projector augmented wave (PAW) method of Blöchl[46,47] coded in the Vienna ab initio simulation package (VASP).[48] All VASP calculations employed the generalized gradient approximation (GGA) with exchange and correlation treated by the Perdew-Burke-Ernzerhof (PBE) and revised PBE (revPBE) functionals, respectively, for structure relaxation and single energy calculations.[46] RevPBE

is a reliable functional for the calculation of H-surface adsorption energy.[49] The convergence threshold for structural relaxation was set to be 0.02 eV/Å in force. The coordinates of all layers of the slabs are optimized with fixed cell volume and cell parameters. The cutoff energy for the plane wave calculations was set to 500 eV and the Brillouin zone integrations were carried out using a 7 × 5 × 1 k-point mesh grid for MoB and $V_{0.31}Mo_{0.69}B$.

The surfaces were constructed by first cleaving the bulk structures into two dimensional (2D) slabs by choosing the right surface to expose along with enough vacuum (more than 10 Å) between slabs to avoid inter-slab interactions. For $V_{0.31}Mo_{0.69}B$ 31% of Mo atoms were replaced4e with V atoms. As shown in **Figure 2.12**, the resulting slabs contain six combined metal and boron layers. For the $V_{0.31}Mo_{0.69}B$ model, the exposed surface is comprised of Mo only with no V, because of previous work showing vanadium borides to have more oxidation compared to Mo borides.[50] The hydrogen coverage on each surface was calculated by dividing the number of H atoms adsorbed on the surface by the number of metal atoms in a single layer.

The Gibbs free energy (ΔG_H) for Hydrogen adsorption on each surface was calculated using the equation $\Delta G_H = \Delta E_H + \Delta E_{ZPE} - T\Delta S$, where ΔE_H is the H-surface binding energy, ΔE_{ZPE} is the zero-point energy difference between adsorbed H and free H_2 (ΔE_{ZPE} is usually very small, from 0.01 eV to 0.05 eV, hence neglected here).[49,51] $T\Delta S$ is obtained by $T\Delta S \approx -1/2\ TS^0(H_2)$, where $S^0(H_2) = 130.7\ J \cdot mol^{-1}K^{-1}$ is the entropy of H_2 in the gas phase at standard conditions.[52] Therefore, $\Delta G_H \approx \Delta E_H + 0.20$. ΔE_H can be calculated from the equation $\Delta E_H = E[surface + n_H] - E[surface + (n-1)H] - 1/2\ E[H_2]$, where $E[H_2]$ is

the total energy of a gas phase H_2 molecule, E[surface + nH] and E[surface + (n-1)H] represent the total energy of n and (n-1) hydrogen atoms adsorbed on the surface, respectively.

2.4. Results and Discussion

2.2.1. Synthesis and Materials Characterization

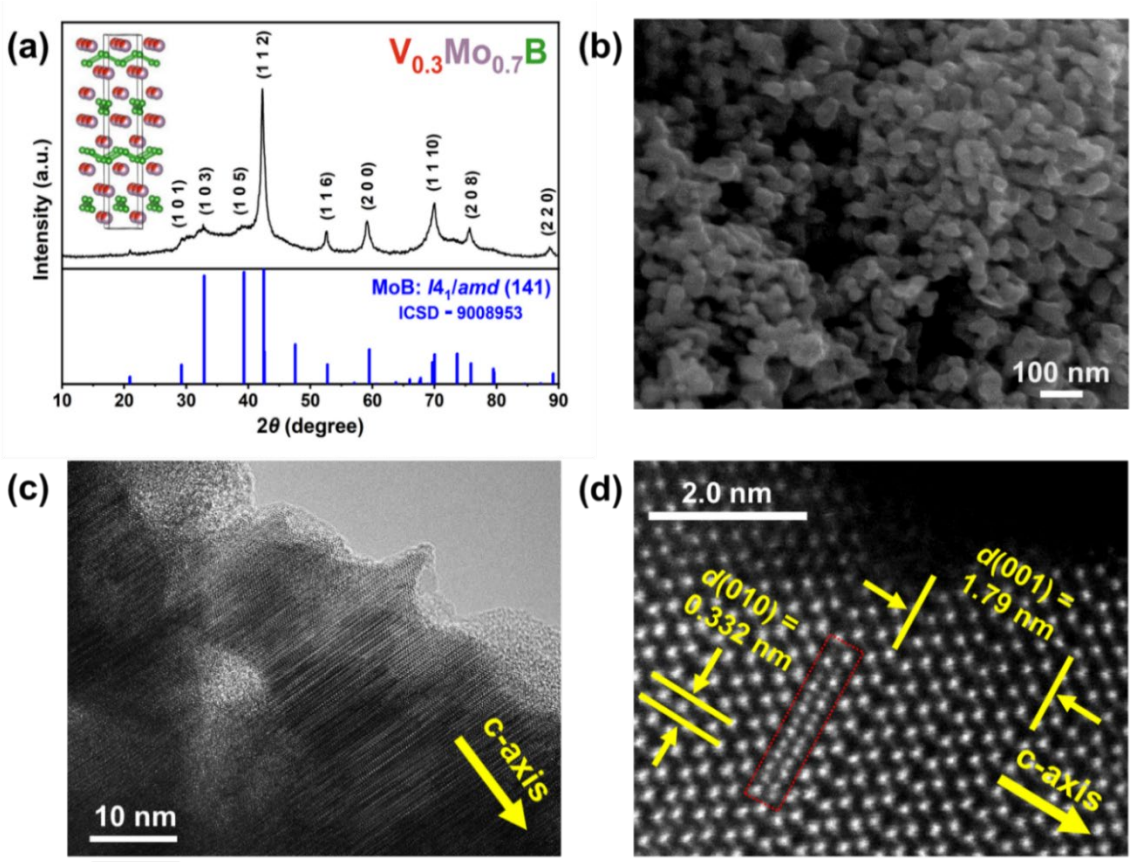

Figure 2.1. (a) Powder X-ray diffraction pattern of synthesized $V_{0.3}Mo_{0.7}B$ (top) compared with the theoretical pattern (bottom). Inset: crystal structure of $V_{0.3}Mo_{0.7}B$ (space group $I4_1/amd$). (b) HRSEM image showing lattice distortions (stacking faults). (c) High-resolution transmission electron microscopy (HRTEM) image and (d) atomic-resolution high-angle annular dark-field scanning transmission electron microscopy (HAADF-STEM) image of $V_{0.3}Mo_{0.7}B$ nanoparticles, displaying interplanar spacings (slightly inaccurate due to lattice distortions, see red rectangle); the bright dots represent metal atoms.

A few years ago, we reported a general synthetic route for nanoscale binary transition metal borides (TMBs),[34] which leverages the redox chemistry of Sn/$SnCl_2$, the volatility and recrystallization of $SnCl_2$ at the synthesis conditions, the immiscibility of tin with boron, and the use of metal halides as metal sources. Here, we have successfully synthesized the first ternary TMB using this method under milder conditions (lower temperature and shorter reaction time), resulting in significantly smaller particle sizes. As shown in the powder X-ray diffraction (PXRD) patterns (**Figure 2.1a**), $V_{0.3}Mo_{0.7}B$ was successfully synthesized as a single-phase material adopting the crystal structure of α-MoB (space group $I4_1/amd$). The elevated background in the PXRD pattern between 30° and 40° in **Figure 2.1a** suggests the presence of diffuse scattering, likely due to structural stacking faults, as evidenced by high-resolution transmission electron microscopy (HRTEM) images (**Figure 2.1c and d**). Such stacking faults are common in monoborides due to the numerous possible arrangements of boron chains within these structures.[53,54] Nevertheless, the lattice parameters were refined to a = 3.1239(9) and c = 16.99(2) Å, which are somewhat larger than those of the parent bulk phase MoB (a = 3.102 and c = 16.967 Å).[25] This expansion is likely attributable to the relaxation of lattice parameters in nanoscale materials, compounded by the presence of stacking faults (see also **Figure 2.1d**).

The reaction conditions were modified to achieve these results. Stoichiometrically, the reduction of each reactant—$MoCl_5$ and VCl_3—requires 2.5 and 1.5 mol of Sn, respectively. For a feed containing 30% VCl_3, precisely 2.2 mol of Sn is needed.[34] Interestingly, using 2.2 mol of Sn still produces elemental Mo as a side phase, suggesting that excess Sn hinders the formation of MoB and favors the production of elemental Mo.

Reducing the Sn content to 2.0 mol results in a complete reaction, yielding a product consisting primarily of the expected phase, along with a trace amount of an unknown phase (**Figure 2.2e**) that can be readily removed by treatment with 10% HCl to yield a single-phase product (**Figure 2.1a**). This observation indicates that boron, as noted in previous work,[34] also contributes to the reduction of metal chlorides. This explains why a slightly smaller amount of Sn is required and why no unreacted metal chlorides are detected in the powder X-ray diffraction (PXRD) patterns prior to HCl washing, as shown in **Figure 2.2e**. Neither VB nor β-MoB, both of which adopt the orthorhombic CrB-type (*Cmcm*) structure, was identified in the PXRD patterns. Notably, a vanadium-free synthesis resulted in the formation of elemental Mo as a secondary phase, as indicated by red asterisks in **Figure 2.2a**. To determine the maximum amount of vanadium that could be substituted for molybdenum, we increased the vanadium content to 50%. However, this led to the formation of elemental Mo (likely doped with V) as a side phase (**Figure 2.2b**), suggesting that the substitution limit is below 50%.

Given that previous syntheses of MoB required higher temperatures, longer reaction times, and excess boron, we tested the new synthesis conditions with an excess of boron (Mo:B = 1:2) in hopes of achieving smaller particles. Although a crystalline single-phase material was obtained under these milder conditions, significant particle growth still occurred, as evidenced by the very sharp reflections in the PXRD pattern (**Figure 2.2d**) and the scanning electron microscopy (SEM) images in **Figure 2.3**. However, the milder synthesis conditions used for the 50% V and V-free syntheses also produced smaller particles compared to previous experiments. Consequently, we plan to evaluate their

hydrogen evolution reaction (HER) catalytic performance. These materials will be designated as MoB/Mo and MoB/B composites to reflect their dual-phase compositions.

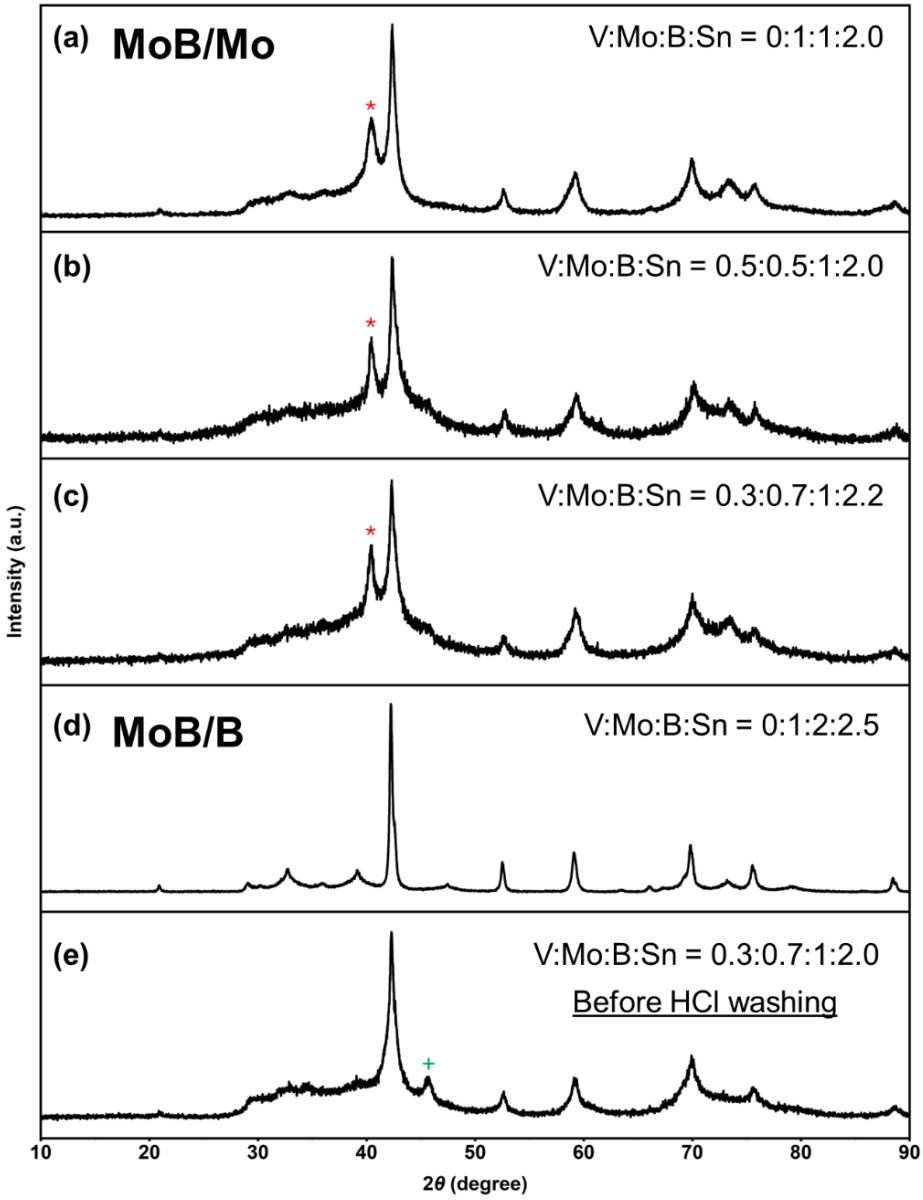

Figure 2.2. Powder X-ray diffraction data of synthesized products of reaction feed rate of VCl_3:$MoCl_5$:B:Sn = a) 0:1:1:2.0 (MoB/Mo), b) 0.5:0.5:1:2.0, c) 0.3:0.7:1:2.2, d) 0:1:2:2.5 (MoB/B) and e) 0.3:0.7:1:2.0 (Before HCl). Peaks of impurity phases are indicated (*: Mo and +: unknown phase that can be removed after HCl treatment). The reaction conditions are the same for all samples at 800°C for 4 hours, except (d) MoB/B for 8 hours.

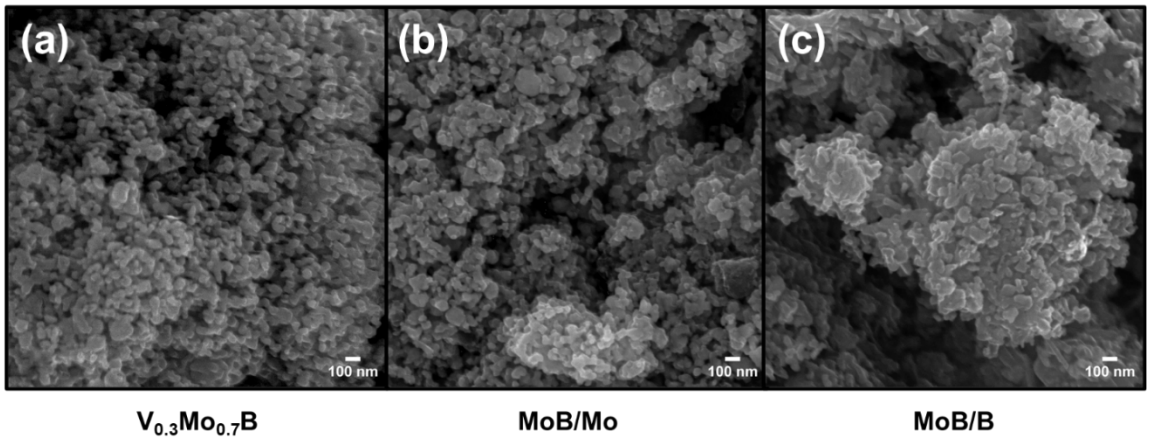

Figure 2.3. HRSEM image of (a) $V_{0.3}Mo_{0.7}B$, (b) MoB/Mo, and (c) MoB/B

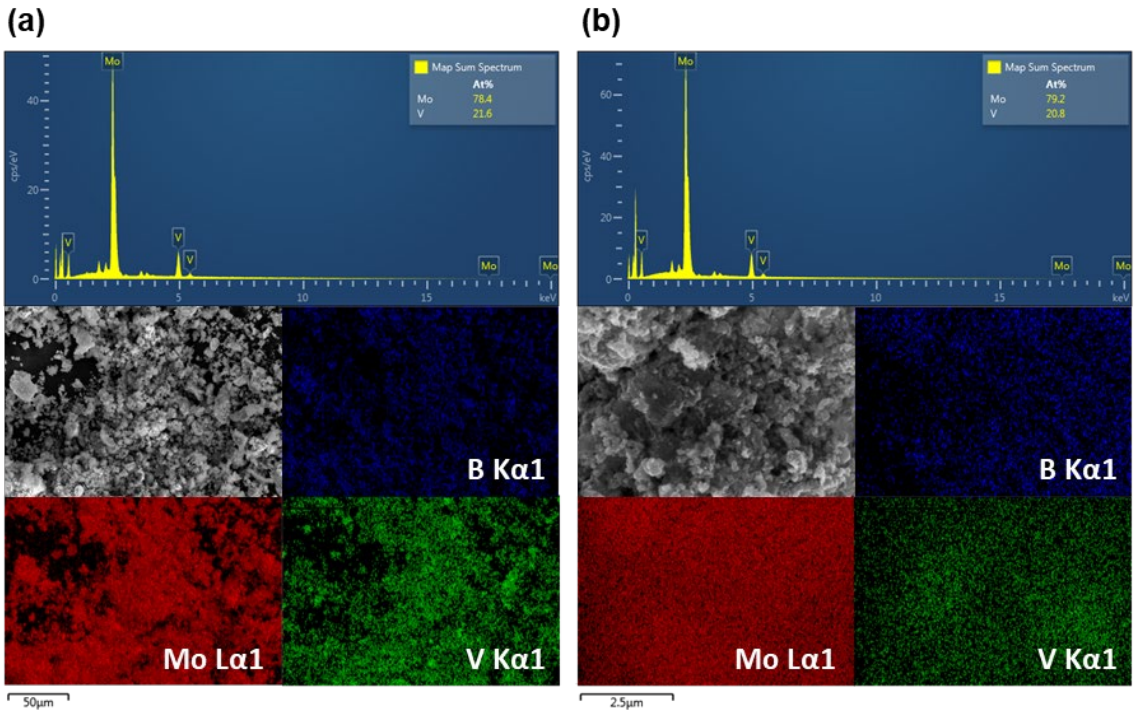

Figure 2.4. EDS mapping of $V_{0.3}Mo_{0.7}B$ for metals (Mo & V) in (a) wide and (b) close up views.

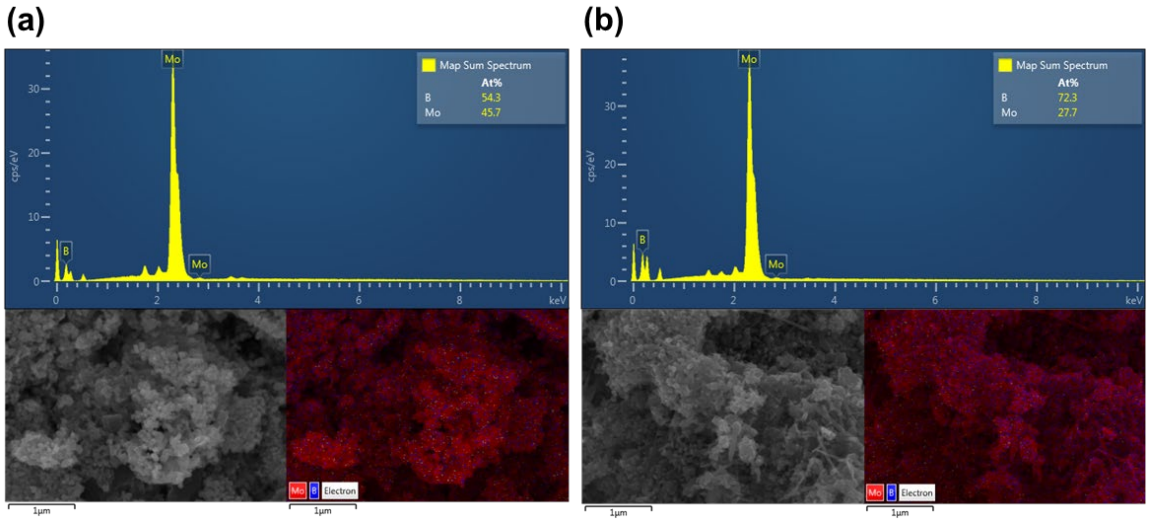

Figure 2.5. SEM image and the corresponding EDS mapping of (a) MoB/Mo and (b) MoB/B to compare B and Mo ratio.

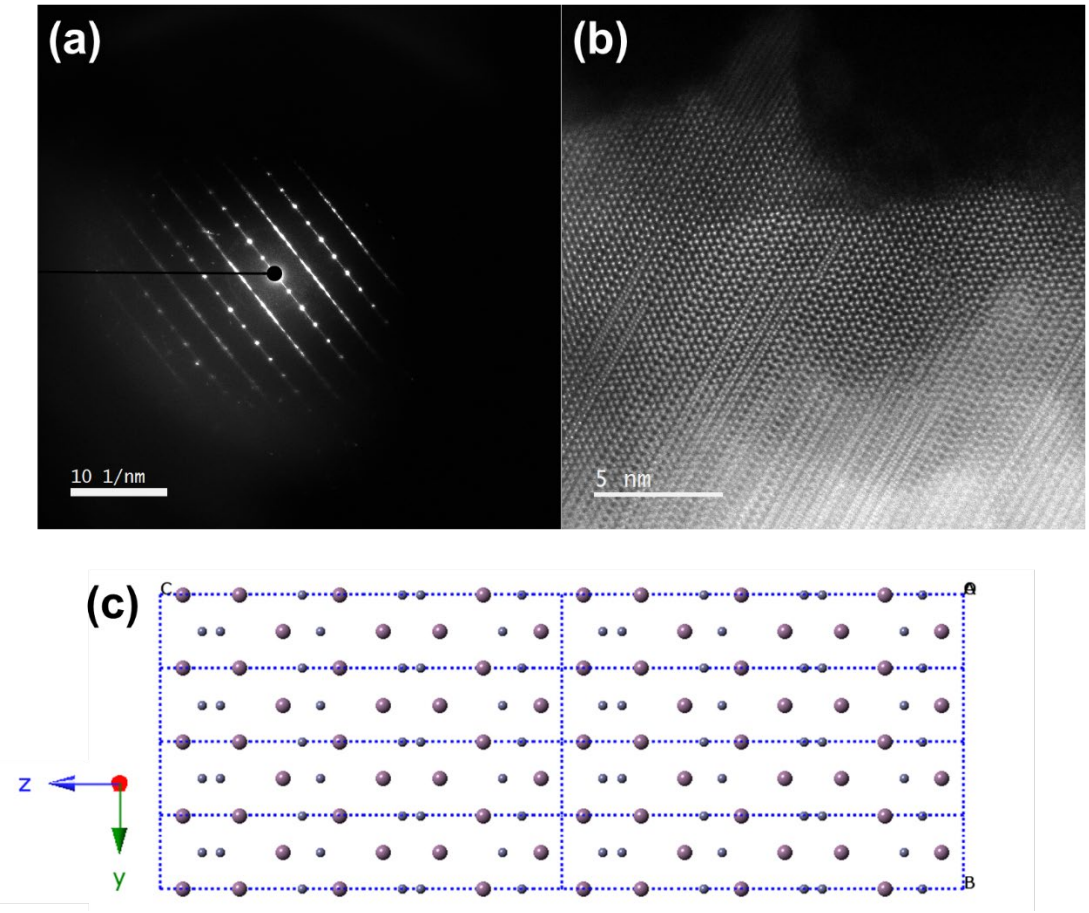

Figure 2.6. (a) Selected area electron diffraction (SAED) pattern, (b) high-resolution STEM image and (c) calculated model structure of $V_{0.3}Mo_{0.7}B$.

Figure 2.1b presents a high-resolution scanning electron microscopy (HRSEM) image of the $V_{0.3}Mo_{0.7}B$ sample. The surface morphology reveals nanoparticles with diameters ranging from 30 to 60 nm. Additionally, the elemental composition and homogeneity of the sample were analyzed using energy-dispersive X-ray spectroscopy (EDS) and elemental mapping, respectively. The EDS mapping results (**Figure 2.4**) demonstrate a uniform distribution of the constituent elements across an ensemble of nanoparticles. Semi-quantitative EDS analysis of the metal content revealed an atomic ratio of Mo to V of ≈8:2, which closely aligns with the composition of the initial mixture. Similarly, semi-quantitative EDS analyses of MoB/Mo and MoB/B composites (**Figure 2.5**) confirm a higher boron content in the MoB/B composite, while significantly less boron is detected in MoB/Mo, consistent with the synthesis expectations described earlier.

The high-resolution transmission electron microscopy (HRTEM) images in **Figure 2.1c** and **Figure 2.6b**, along with the atomic-resolution high-angle annular dark-field scanning transmission electron microscopy (HAADF-STEM) image in **Figure 2.1d**, demonstrate the crystallinity of the $V_{0.3}Mo_{0.7}B$ nanoparticles. TEM observations along the [100] direction successfully revealed characteristic stacking defects along the *c*-axis, consistent with the stacking faults anticipated from the powder X-ray diffraction (PXRD) analysis above. The selected area electron diffraction (SAED) pattern (**Figure 2.6a**) of a single nanoparticle (**Figure 2.6b**) exhibits intense diffraction peaks, which can be indexed to sets of crystal planes and lattice parameters corresponding to the tetragonal MoB-type structure (space group $I4_1/amd$), further confirming the crystalline nature of the

nanoparticles. However, the presence of characteristic diffuse scattering also indicates stacking disorder.

The surface chemical composition and core-level binding energies of $V_{0.3}Mo_{0.7}B$ were examined using X-ray photoelectron spectroscopy (XPS). Detailed results of these analyses are presented in **Figure 2.7** and **Table 2.1** illustrating the oxidation states of the B, V, and Mo species on the analyzed surfaces. As shown in **Figure 2.7c**, the B 1s spectrum exhibits a peak at 189.3 eV, corresponding to B^0 in metallic $V_{0.3}Mo_{0.7}B$, as well as peaks at 191.2 and 193.1 eV, which are assigned to sub-oxidized (B_2O_2) and fully oxidized (B_2O_3) boron species, respectively. These findings are consistent with previous reports on boride compounds, which demonstrate similar oxidation behavior in transition metal boride nanoparticles.[55,56] The high-resolution V 2p spectrum (**Figure 2.7a**) is deconvoluted into four peaks at 512.3, 517.5, 520.9, and 523.0 eV. The smaller peaks at 512.3 and 520.9 eV correspond to the $2p_{3/2}$ and $2p_{1/2}$ states of V^0 in $V_{0.3}Mo_{0.7}B$, while the peaks at 517.5 and 523.0 eV are attributed to the $2p_{3/2}$ and $2p_{1/2}$ states of V^{5+} in V_2O_5. These results align with previously reported studies on vanadium oxides and their corresponding binding energies.[50,57] Similarly, the Mo 3d spectrum (**Figure 2.7b**) primarily features peaks at 233.0 and 236.1 eV, which correspond to the $3d_{5/2}$ and $3d_{3/2}$ states of Mo^{6+} in MoO_3. However, smaller peaks at 228.1 and 230.6 eV are assigned to Mo^0 in $V_{0.3}Mo_{0.7}B$, indicating that molybdenum on the surface is predominantly oxidized.[32] The nanoparticle surfaces exhibit greater oxidation compared to bulk borides, which is expected due to the higher surface-area-to-volume ratio in smaller particles.

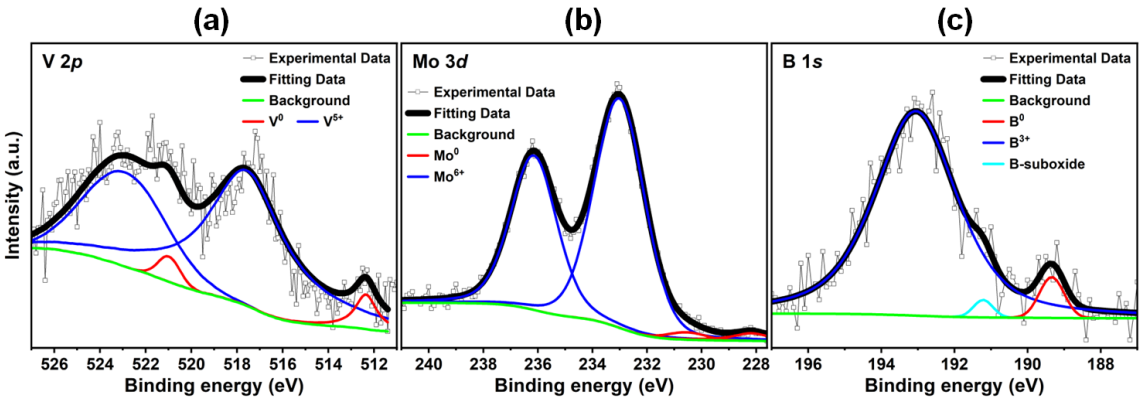

Figure 2.7. Deconvoluted XPS spectra of $V_{0.3}Mo_{0.7}B$: a) core-level V 2p, b) core-level Mo 3d, and c) core-level B 1s

Table 2.1. XPS peak position and full width at half maximum (FWHM) parameters for V 2p, Mo 3d, and B 1s of $V_{0.3}Mo_{0.7}B$ before and after HER.

Phase	Assigned Species		Peak position (eV)	FWHM (eV)
$V_{0.3}Mo_{0.7}B$	V^{5+} (V_2O_5)	$2p_{3/2}$	517.5	4.03
		$2p_{1/2}$	523.0	4.27
	V^0 ($V_{0.3}Mo_{0.7}B$)	$2p_{3/2}$	512.3	1.13
		$2p_{1/2}$	520.9	1.14
	Mo^{6+} (MoO_3)	$3d_{5/2}$	233.0	2.18
		$3d_{3/2}$	236.1	2.00
	Mo^0 ($V_{0.3}Mo_{0.7}B$)	$3d_{5/2}$	228.1	1.62
		$3d_{3/2}$	230.6	1.62
	B^{3+} (B_2O_2)		193.1	2.66
	B-suboxide (B_2O_2)		191.2	0.62
	B^0 ($V_{0.3}Mo_{0.7}B$)		189.3	0.79
$V_{0.3}Mo_{0.7}B$ After HER	V^{5+} (V_2O_5)	$2p_{3/2}$	517.2	1.14
	V^{3+} (V_2O_3)	$2p_{1/2}$	523.0	2.64
	V^{2+} (VO)	$2p_{1/2}$	521.1	3.18
	V^0 ($V_{0.3}Mo_{0.7}B$)	$2p_{3/2}$	511.9	2.9
		$2p_{1/2}$	519.1	1.9
	Mo^{6+} (MoO_3)	$3d_{5/2}$	232.3	2.07
		$3d_{3/2}$	235.4	2.48
	B^{3+} (B_2O_2)		193.2	2.28
	B-suboxide (B_2O_2)		191.9	3.22
	B^0 ($V_{0.3}Mo_{0.7}B$)		189.0	7.37

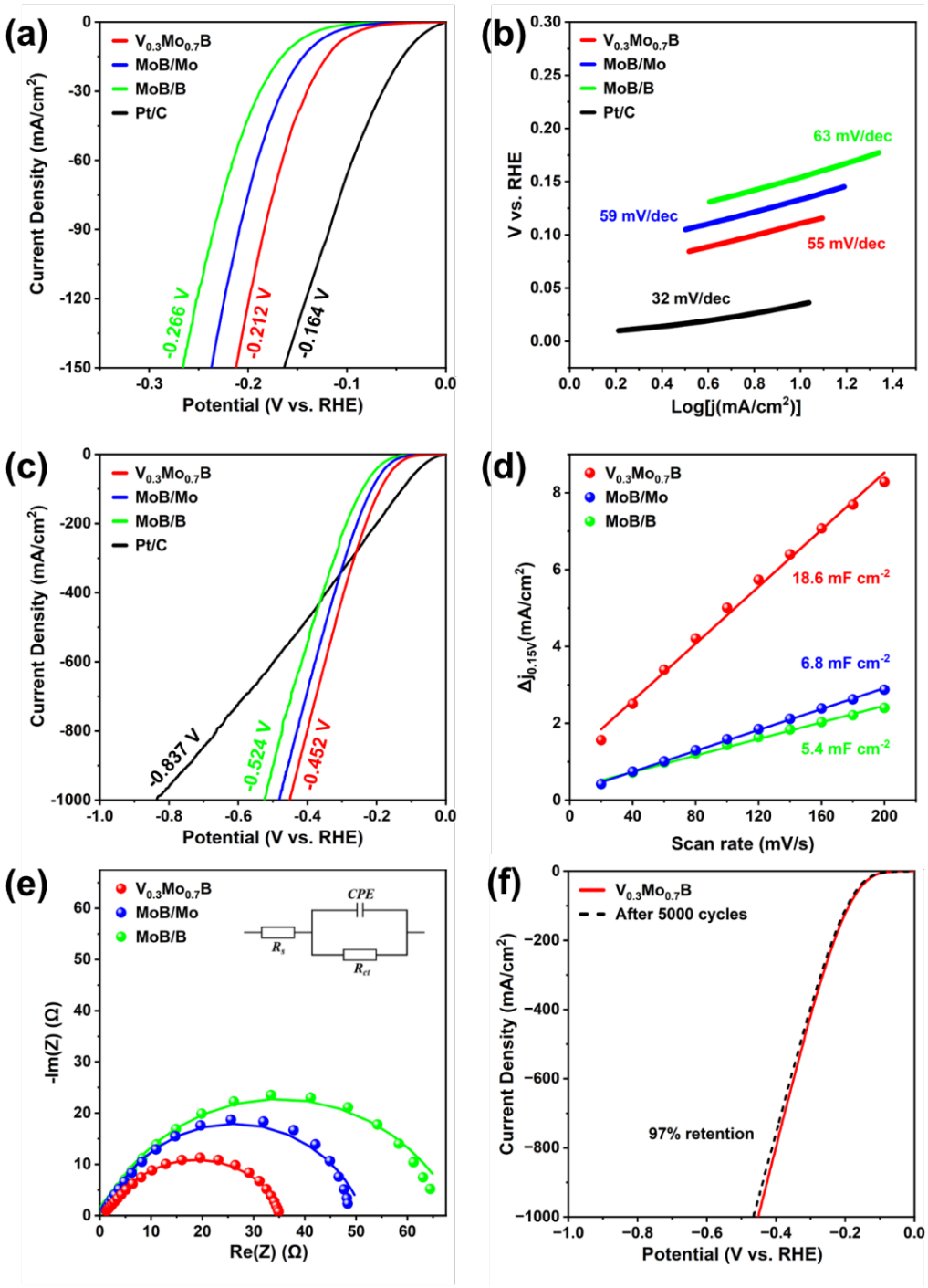

Figure 2.8. Linear sweep polarization curves of different materials ($V_{0.3}Mo_{0.7}B$, MoB/Mo, MoB/B, 20% Pt/C) recorded in 0.5 m H_2SO_4 at current densities up to (a) 150 and (c) 1000 mA cm^{-2}. (b) Tafel plots of these materials. (d) Charging current density difference plotted against scan rate to determine the double-layer capacitance (C_{dl}) of the borides samples. (e) Nyquist plot representations of the electrochemical impedance spectra of the borides samples. (f) Polarization curves of $V_{0.3}Mo_{0.7}B$ electrode after 5000 cycles.

2.2.2. Electrocatalytic Activity and Stability

The hydrogen evolution reaction (HER) activity of the $V_{0.3}Mo_{0.7}B$ sample was evaluated using a standard three-electrode system in an acidic environment of 0.5 M H_2SO_4. For comparison, 20% Pt/C, MoB/Mo, and MoB/B were also tested under identical conditions. **Figure 2.8a** presents the iR-corrected polarization curves up to a current density of 150 mA cm^{-2} measured in 0.5 m H_2SO_4. As expected, Pt/C exhibited excellent HER activity, requiring an overpotential of only 164 mV to achieve 150 mA cm^{-2},[27] whereas $V_{0.3}Mo_{0.7}B$ demonstrated the highest activity among the MoB-based electrodes. It required an overpotential of just 212 mV, while the MoB/Mo and MoB/B composite electrodes needed slightly higher overpotentials of 237 and 266 mV, respectively, to reach 150 mA cm^{-2}. The three MoB-based electrodes exhibited high but significantly different HER activities. The single-phase $V_{0.3}Mo_{0.7}B$, being the most active of the three, highlights the importance of achieving a single-phase material and the advantage of solid solution formation. Indeed, we have previously demonstrated for bulk materials that solid solution formation enhances the activity of metal borides, as seen in the $Mo_{1-x}W_xB_2$[28] and $Cr_{1-x}Mo_xB_2$[27] solid solutions, which outperform their respective binary parent systems (x = 0 or 1). However, the MoB/Mo and MoB/B composites also displayed very good performance, which is not surprising, given that most boride nanomaterials studied to date are rarely single-phase yet still exhibit high activities.[58–63] **Figure 2.8b** displays the Tafel slopes of the studied materials, providing insight into their HER catalytic mechanisms. In an acidic electrolyte, the HER mechanism involves three possible rate-determining steps (RDS): the Volmer reaction (Tafel slope ≈120 mV/dec),

the Heyrovsky reaction (Tafel slope ≈40 mV/dec), and the Tafel reaction (Tafel slope ≈30 mV/dec).[64,65] The Tafel slopes of Pt/C, $V_{0.3}Mo_{0.7}B$, MoB/Mo, and MoB/B were derived from the linear portions of the Tafel plots (**Figure 2.8b**). The calculated Tafel slope for Pt/C is 32 mV/dec, consistent with a Volmer-Tafel mechanism where the Tafel step is rate-limiting. For $V_{0.3}Mo_{0.7}B$, MoB/Mo, and MoB/B, the Tafel slopes were 55, 58, and 63 mV/dec, respectively, indicating faster kinetics and a rapid hydrogen generation rate during the HER process for $V_{0.3}Mo_{0.7}B$. These values do not align precisely with the typical Tafel slopes for the Volmer, Heyrovsky, or Tafel reactions, suggesting more complex mechanisms. Notably, the Tafel slope of 55 mV/dec for $V_{0.3}Mo_{0.7}B$ is among the lowest reported for non-noble metal boride electrodes to date, further confirming its superior activity.[63,66]

Figure 2.8c shows the polarization curves of all studied electrodes up to an industry-relevant current density of 1000 mA cm^{-2}. It is well established that Pt/C, a commercially available benchmark electrocatalyst, exhibits excellent intrinsic HER catalytic activity at low current densities (see above). However, Pt/C struggles to maintain efficient performance at higher current densities (several hundred mA/cm^2 or more) in a 0.5 m H_2SO_4 solution. This inefficiency is primarily attributed to the "bubble effect" at high current densities, where hydrogen gas bubbles accumulate and impede further reactions, particularly in an acidic environment.[67,68] In contrast, all the boride electrodes demonstrate superior electrocatalytic activity for HER compared to Pt/C at current densities exceeding 300 mA cm^{-2}. This aspect of HER performance at high current densities is critical for practical applications, as industrial water electrolysis requires

significantly higher current densities.[69] $V_{0.3}Mo_{0.7}B$ requires an overpotential of only 0.452 V to achieve 1000 mA cm^{-2}, nearly half that of Pt/C (η_{1000} = 0.837 V). Similarly, MoB/Mo and MoB/B exhibit significantly reduced overpotentials of 0.482 and 0.524 V, respectively, both outperforming the commercial 20% Pt/C electrode. This superior performance of the borides suggests a high number of effective active sites and good surface coverage by the boride nanoparticles. Remarkably, such high activity at elevated current densities has not been previously reported for boride nanoparticles smaller than 100 nm, highlighting the novel capabilities of these materials synthesized under mild conditions. Although similar current densities have been reported for bulk boride materials,[27,45] differences in electrode preparation between bulk materials and nanoparticles make direct comparisons challenging.

Table 2.2. Fitted EIS data from Nyquist Plots in **Figure 2.8e**.

Electrode type	R_s [Ohm]	R_{ct} [Ohm]	CPE [F s^{a-1}]	a
$V_{0.3}Mo_{0.7}B$	**11.9**	**35.2**	**3.71 e^{-3}**	**0.706**
MoB/Mo	**11.0**	**50.5**	**1.04 e^{-3}**	**0.786**
MoB/B	**10.7**	**69.6**	**0.72 e^{-3}**	**0.743**

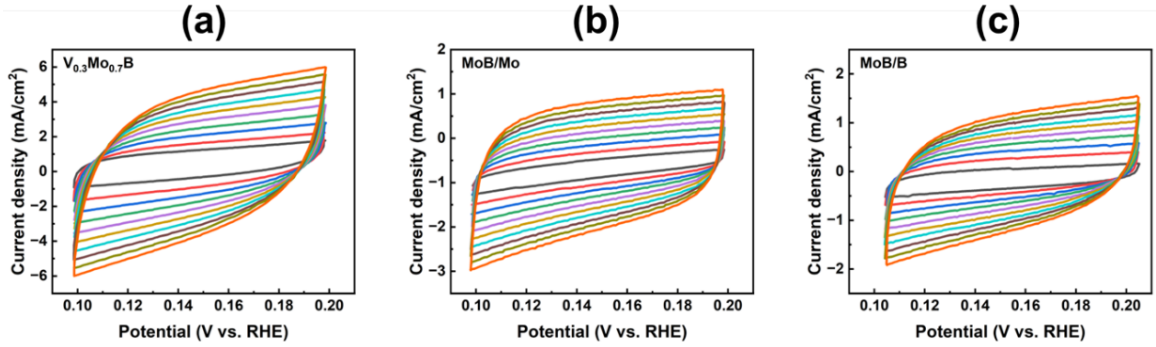

Figure 2.9. C_{dl} measurements from cyclic voltammetry profiles at different scan rates from 20 to 200 mV/s for (a) $V_{0.3}Mo_{0.7}B$, (b) MoB/Mo, (c) MoB/B.

The high HER efficiency of $V_{0.3}Mo_{0.7}B$ can be attributed to its electrochemically active surface area (ECSA) and electrochemical impedance spectroscopy (EIS) results. In **Figure 2.8d**, the ECSA was estimated based on the electrochemical double-layer capacitance (C_{dl}).[70] The C_{dl} was determined from cyclic voltammetry (CV) measurements at various scan rates (20–200 mV s^{-1}) within a non-Faradaic region from 0.10 to 0.20 V versus RHE (**Figure 2.9**). As expected, $V_{0.3}Mo_{0.7}B$ exhibited the highest C_{dl} (18.6 mF cm^{-2}) among the borides, indicating a significantly greater number of active sites compared to the MoB/Mo and MoB/B composite electrodes, which had C_{dl} values of 6.8 and 5.4 mF cm^{-2}, respectively. Additionally, EIS data in **Figure 2.8e** reveal the electron transfer resistance of $V_{0.3}Mo_{0.7}B$. The Nyquist plots for each electrode were fitted using an equivalent circuit model consisting of a solution resistance (R_s), a charge transfer resistance (R_{ct}), and a constant phase element (CPE), with derived values provided in **Table 2.2**. As shown in **Figure 2.8e** and **Table 2.2**, the R_s values for all samples are similar due to the consistent electrode preparation method. However, the R_{ct} value for $V_{0.3}Mo_{0.7}B$ (35.2 Ω) is significantly lower than those of the MoB/Mo (50.5 Ω) and MoB/B (69.6 Ω) composite electrodes, indicating greater electrical conductivity for $V_{0.3}Mo_{0.7}B$. These findings align with the overpotential and Tafel slope results, supporting the superior HER activity of $V_{0.3}Mo_{0.7}B$.

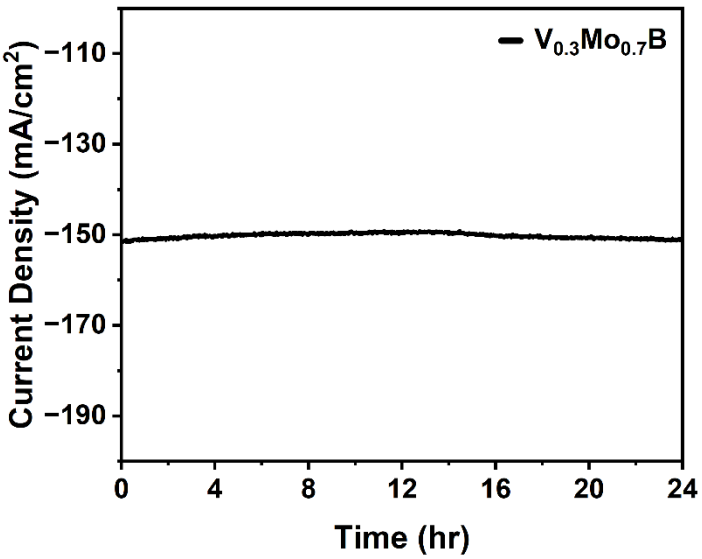

Figure 2.10. Chronoamperometry curve of $V_{0.3}Mo_{0.7}B$ electrode for 24 h in 0.5 M H_2SO_4.

The stability and durability of catalysts are critical for their practical application in acidic environments. Therefore, both properties were evaluated for the $V_{0.3}Mo_{0.7}B$ electrode. Durability was assessed through a continuous electrolysis test at a fixed current density of ≈−150 mA cm^{-2} for 24 h, with results shown in **Figure 2.10** indicating nearly no change in current density, demonstrating robust performance. Long-term stability was evaluated by cyclic voltammetry over 5000 cycles, equivalent to ≈100000 s (≈28 h), at a high current density of 1000 mA cm^{-2}. As depicted in **Figure 2.8f**, the polarization curve after testing showed minimal change, retaining an impressive 97% of the initial activity.

These results confirm that the $V_{0.3}Mo_{0.7}B$ electrode maintains its electrocatalytic activity under prolonged, industry-relevant conditions, attesting to its robustness and suitability for sustainable hydrogen production in demanding settings. X-ray photoelectron spectroscopy (XPS) measurements conducted post-electrochemical testing (**Figure 2.11**

and **Table 2.1**) reveal that all initial species, except for V^{5+} (which was reduced to V^{3+}/V^{2+}), remain present. The significance of the V^{5+} reduction to V^{3+}/V^{2+} is currently unclear, prompting planned in situ studies for a more detailed analysis of surface evolution during HER. Nevertheless, the persistence of boride species (V^0, B^0) suggests that, despite these harsh conditions, the boride remains unoxidized and likely plays a critical role in the high current density performance of this novel material. Below, we employ density functional theory (DFT) calculations to further elucidate the activity of this highly active boride.

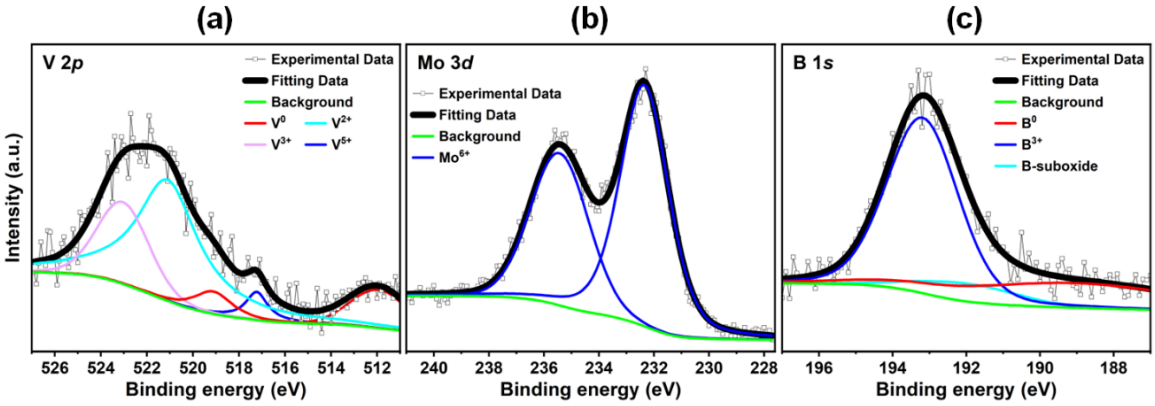

Figure 2.11. Deconvoluted XPS spectra of $V_{0.3}Mo_{0.7}B$ after activity/stability test at 1000 mA/cm^2: (a) core-level B 1s, (b) core-level V 2p, and (c) core-level Mo 3d.

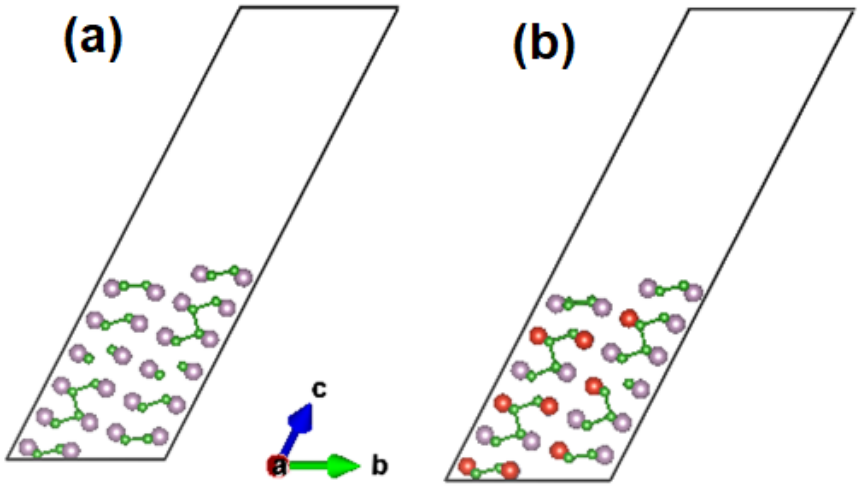

Figure 2.12. Surface slab models for the {112} surface of (a) MoB and (b) $V_{0.31}Mo_{0.69}B$.

2.2.3. Computational Analysis of Activity

To better understand the high activity of the borides, particularly at high current densities compared to Pt, we calculated the Gibbs free energy (ΔG_H) for atomic hydrogen (H) adsorption, which serves as a descriptor for correlating theoretical predictions with experimental measurements.[11,50,71] Optimal hydrogen evolution reaction (HER) activity is achieved when the ΔG_H value is close to zero, indicating that the overall reaction, encompassing both H adsorption and H_2 desorption, proceeds at the maximum rate. For these DFT calculations, the {112} surface was modeled (**Figure 2.12**), as it is the most exposed facet, based on the diffraction pattern in **Figure 2.1a**. Indeed, refinement of the powder X-ray diffraction (XRD) data, as shown in **Figure 2.13**, clearly reveals a preferential orientation of the $V_{0.3}Mo_{0.7}B$ sample along the {112} surface, supporting the selection of this facet for theoretical analysis.

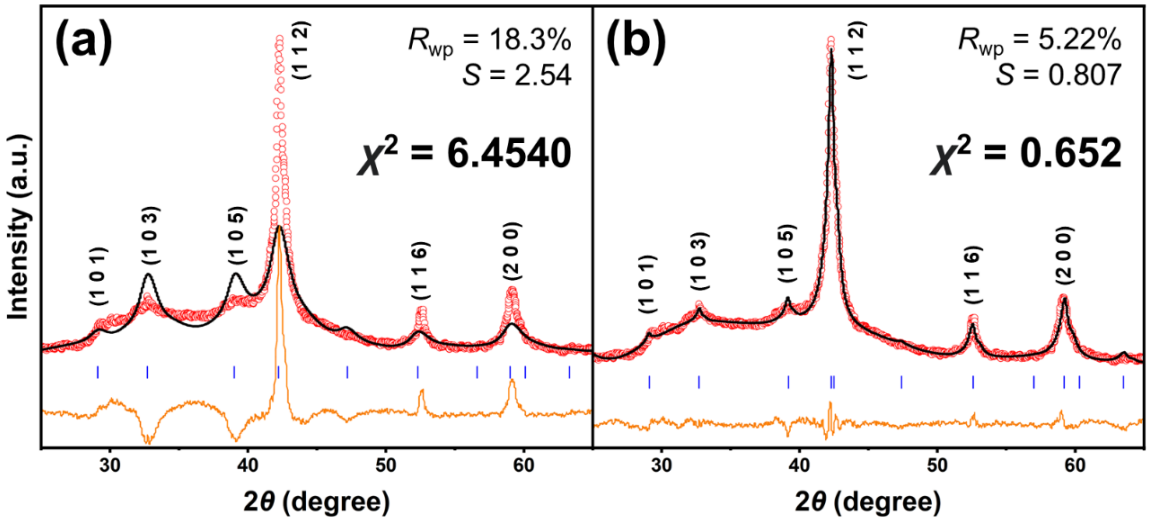

Figure 2.13. Powder X-ray diffraction data (red circles) of $V_{0.3}Mo_{0.7}B$, the Rietveld refined data (black line), and the difference curve (orange line) between observed and refined data (a) without preferred orientation and (b) with (112) preferred orientation.

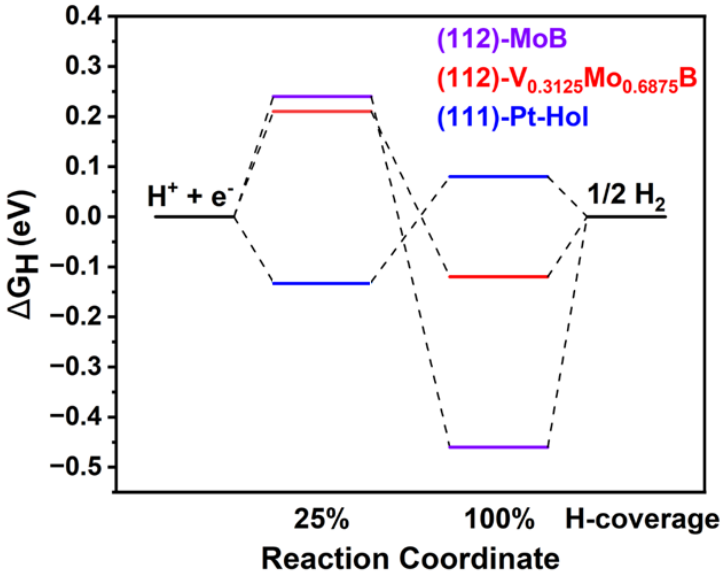

Figure 2.14. Calculated Gibbs free energy diagram for 25% and 100% hydrogen coverage of different HER active sites on surfaces of $V_{0.3125}Mo_{0.6875}B$, MoB, and Pt.

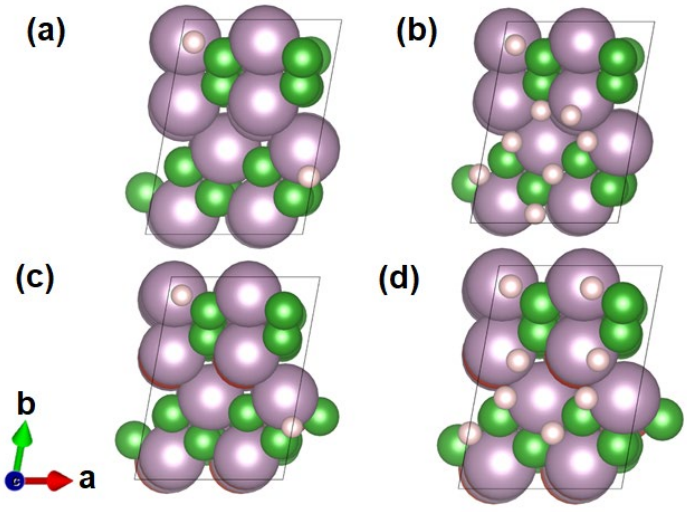

Figure 2.15. Different HER active sites on surfaces of (a) & (b) MoB and (c) & (d) $V_{0.3125}Mo_{0.6875}B$, at high and low hydrogen coverages.

The Gibbs free energy (ΔG_H) for H adsorption on MoB and $V_{0.3125}Mo_{0.6875}B$ (a model for the experimental $V_{0.3}Mo_{0.7}B$ composition) was studied at low (12.5%) and high (100%) hydrogen coverages to simulate catalyst performance at low and high current densities, respectively. As shown in **Figure 2.14**, the ΔG_H values for MoB and $V_{0.3125}Mo_{0.6875}B$ were +0.24 and +0.21 eV, respectively, at low (12.5%) hydrogen coverage, and −0.46 and −0.12 eV, respectively, at high (100%) hydrogen coverage. These results are consistent with the onset potential observed experimentally in **Figure 2.8a**. At low hydrogen coverages, the H adsorption rates on the surfaces of MoB and $V_{0.3125}Mo_{0.6875}B$ are comparable, with a slight preference for the latter.

Notably, at high hydrogen coverages (100%), the ΔG_H values are negative, with $V_{0.3125}Mo_{0.6875}B$ exhibiting a value much closer to 0 eV, indicating an excellent H_2 desorption rate at high current densities. In comparison, Pt (using the most active hollow adsorption site on the {111} surface) has ΔG_H values of −0.13 and +0.08 eV at low and high hydrogen coverages, respectively.[32] As expected, the Pt {111} surface performs exceptionally well at low current densities, with a ΔG_H value that is negative and closer to zero, while $V_{0.3125}Mo_{0.6875}B$ has a positive value (+0.21 eV) slightly further from zero, suggesting it is less efficient than Pt at low current densities, consistent with experimental findings. Interestingly, the signs of ΔG_H reverse at high hydrogen coverages, indicating a potential shift in hydrogen production rate favoring the boride at high current densities, which further corroborates the experimental results.

To further explain the significant enhancement of ΔG_H, particularly at high hydrogen coverages, the distributions of H adsorption sites on the surfaces of MoB and

$V_{0.3125}Mo_{0.6875}B$ were compared at both low (**Figures 2.15a**,**c**) and high (**Figures 2.15b,d**) coverages. At low hydrogen coverage (12.5%), both MoB and $V_{0.3125}Mo_{0.6875}B$ exhibit the same active sites, which accounts for the similarity of the two surfaces in the reaction coordinate diagram (**Figure 2.14**). However, this changes dramatically at high hydrogen coverages, as shown in **Figures 2.15b**,**d**. For MoB (**Figure 2.15b**), six of the H adsorption sites are hollow sites, where the H atom adsorbs between two Mo atoms and one B atom, while two sites are atop Mo atoms. In contrast, for $V_{0.3125}Mo_{0.6875}B$ (**Figure 2.15d**), substituting 31.25% of the Mo atoms just below the surface with V atoms makes the adsorption sites atop the surface-layer Mo atoms favorable at high hydrogen coverages, resulting in four H atoms adsorbed atop Mo atoms and four in hollow sites. Previous studies on MoB_2 and VB_2 borides as HER catalysts have shown that H adsorption sites atop metal atoms typically yield a positive ΔG_H, which does not favor H atom adsorption, whereas hollow sites between two metal atoms and one boron atom exhibit a slightly negative ΔG_H near zero, favoring H adsorption.[50] For $V_{0.3125}Mo_{0.6875}B$, an optimal balance appears to occur with an equal number of hollow and atop sites. This balance enables a synergistic effect: the four hollow sites facilitate H atom adsorption onto the surface, while the four nearby atop sites promote the dissociation of H_2 molecules, allowing their efficient release from the catalyst surface.

2.5. Conclusion

In this work, we have demonstrated the successful synthesis of vanadium-substituted molybdenum boride ($V_{0.3}Mo_{0.7}B$) nanoparticles using a $Sn/SnCl_2$-redox reaction method, achieving a single-phase product under milder conditions than those typically required for molybdenum borides. The synthesized $V_{0.3}Mo_{0.7}B$ nanoparticles (30–60 nm) exhibited outstanding hydrogen evolution reaction (HER) performance, particularly at the high current densities required for industrial-scale hydrogen production. At a current density of 1000 mA cm^{-2}, the catalyst required an overpotential of only 0.452 V, significantly lower than that of the commercial 20% Pt/C benchmark, highlighting its potential for large-scale applications. Electrochemical measurements confirmed that vanadium substitution increases the number of active catalytic sites and enhances electron transfer efficiency, leading to superior HER performance. Density functional theory (DFT) calculations were performed to evaluate the Gibbs free energy (ΔG_H) for H adsorption on the {112} surfaces of MoB and $V_{0.3}Mo_{0.7}B$. At high hydrogen coverage (100%), $V_{0.3}Mo_{0.7}B$ exhibited a ΔG_H of −0.12 eV, compared to +0.08 eV for the Pt {111} surface, suggesting more favorable behavior at high current densities for the boride, which supports experimental findings. Additionally, the $V_{0.3}Mo_{0.7}B$ catalyst demonstrated excellent long-term durability, retaining 97% of its initial activity after 5000 electrochemical cycles at high current density. This durability, combined with its exceptional electrocatalytic efficiency, positions vanadium-substituted MoB as a robust and cost-effective alternative to noble metal-based catalysts for the HER.

2.6. References

1. Li, X.; Hao, X.; Abudula, A.; Guan, G., Nanostructured catalysts for electrochemical water splitting: Current state and prospects., *Journal of Materials Chemistry A*, **2016**, *4*, (31), 11973–12000.
2. Roger, I.; Shipman, M. A.; Symes, M. D., Earth-abundant catalysts for electrochemical and photoelectrochemical water splitting., *Nat Rev Chem*, **2017**, *1*.
3. Cheng, N.; Stambula, S.; Wang, D.; Banis, M. N.; Liu, J.; Riese, A.; Xiao, B.; Li, R.; Sham, T. K.; Liu, L. M.; Botton, G. A.; Sun, X., Platinum single-atom and cluster catalysis of the hydrogen evolution reaction., *Nat Commun*, **2016**, *7*, (1), 13638.
4. Zhang, L.; Shi, Z.; Lin, Y.; Chong, F.; Qi, Y., Design Strategies for Large Current Density Hydrogen Evolution Reaction., *Front Chem*, **2022**, *10*.
5. Hua, W.; Sun, H. H.; Xu, F.; Wang, J. G., A review and perspective on molybdenum-based electrocatalysts for hydrogen evolution reaction., *Rare Met*, **2020**, *39*, (4), 335–351.
6. Li, J.; Li, J.; Hu, J.; Chen, P., Perspectives on Mo-Based Electrocatalysts for the Hydrogen Evolution Reaction: A Comprehensive Review., *Energy and Fuels*, **2023**, *37*, (23), 17803–17835.
7. Sun, X.; Dai, J.; Guo, Y.; Wu, C.; Hu, F.; Zhao, J.; Zeng, X.; Xie, Y., Semimetallic molybdenum disulfide ultrathin nanosheets as an efficient electrocatalyst for hydrogen evolution., *Nanoscale*, **2014**, *6*, (14), 8359–8367.
8. Xing, Z.; Liu, Q.; Asiri, A. M.; Sun, X., Closely interconnected network of molybdenum phosphide nanoparticles: A highly efficient electrocatalyst for generating hydrogen from water., *Adv Mater*, **2014**, *26*, (32), 5702–5707.
9. Prins, R.; Bussell, M. E., Metal phosphides: Preparation, characterization and catalytic reactivity., *Catalysis Letters*, **2012**, *142*, (12), 1413–1436.
10. Yang, J.; Zhang, F.; Wang, X.; He, D.; Wu, G.; Yang, Q.; Hong, X.; Wu, Y.; Li, Y., Porous Molybdenum Phosphide Nano-Octahedrons Derived from Confined Phosphorization in UIO-66 for Efficient Hydrogen Evolution., *Angew Chem Int Ed*, **2016**, *128*, (41), 13046–13050.
11. Xiao, P.; Sk, M. A.; Thia, L.; Ge, X.; Lim, R. J.; Wang, J. Y.; Lim, K. H.; Wang, X., Molybdenum phosphide as an efficient electrocatalyst for the hydrogen evolution reaction., *Energy Environ Sci*, **2014**, *7*, (8), 2624–2629.
12. Vrubel, H.; Hu, X., Molybdenum boride and carbide catalyze hydrogen evolution in both acidic and basic solutions., *Angew Chem Int Ed*, **2012**, *51*, (51), 12703–12706.

13. T. F. Jaramillo; K. P. Jørgensen; J. Bonde; J. H. Nielsen; S. Horch; I. Chorkendorff, Identification of Active Edge Sites for Electrochemical H2 Evolution from MoS2 Nanocatalysts., *Science (1979)*, **2007**, *317*, (5834), 100–102.

14. Lee, D. W.; Jin, X.; Yun, S. Y.; Hwang, S. J., Boride-induced phase tuning of defect-introduced MoS2 nanosheets to boost the electrocatalytic hydrogen evolution reaction., *J Mater Chem A Mater*, **2023**, *11*, (46), 25308–25315.

15. Xiong, J.; Cai, W.; Shi, W.; Zhang, X.; Li, J.; Yang, Z.; Feng, L.; Cheng, H., Salt-templated synthesis of defect-rich MoN nanosheets for boosted hydrogen evolution reaction., *J Mater Chem A Mater*, **2017**, *5*, (46), 24193–24198.

16. Yin, Y.; Zhang, Y.; Gao, T.; Yao, T.; Zhang, X.; Han, J.; Wang, X.; Zhang, Z.; Xu, P.; Zhang, P.; Cao, X.; Song, B.; Jin, S., Synergistic Phase and Disorder Engineering in 1T-MoSe2 Nanosheets for Enhanced Hydrogen-Evolution Reaction., *Adv Mater*, **2017**, *29*, (28).

17. Kong, D.; Wang, H.; Cha, J. J.; Pasta, M.; Koski, K. J.; Yao, J.; Cui, Y., Synthesis of MoS2 and MoSe2 films with vertically aligned layers., *Nano Lett*, **2013**, *13*, (3), 1341–1347.

18. Xie, J.; Zhang, H.; Li, S.; Wang, R.; Sun, X.; Zhou, M.; Zhou, J.; Lou, X. W.; Xie, Y., Defect-rich MoS2 ultrathin nanosheets with additional active edge sites for enhanced electrocatalytic hydrogen evolution., *Adv Mater*, **2013**, *25*, (40), 5807–5813.

19. Xu, C.; Peng, S.; Tan, C.; Ang, H.; Tan, H.; Zhang, H.; Yan, Q., Ultrathin S-doped MoSe2 nanosheets for efficient hydrogen evolution., *J Mater Chem A Mater*, **2014**, *2*, (16), 5597–5601.

20. Zhu, J.; Wang, Z. C.; Dai, H.; Wang, Q.; Yang, R.; Yu, H.; Liao, M.; Zhang, J.; Chen, W.; Wei, Z.; Li, N.; Du, L.; Shi, D.; Wang, W.; Zhang, L.; Jiang, Y.; Zhang, G., Boundary activated hydrogen evolution reaction on monolayer MoS 2., *Nat Commun*, **2019**, *10*, (1).

21. Lee, J. E.; Jung, J.; Ko, T. Y.; Kim, S.; Kim, S. Il; Nah, J.; Ryu, S.; Nam, K. T.; Lee, M. H., Catalytic synergy effect of MoS2/reduced graphene oxide hybrids for a highly efficient hydrogen evolution reaction., *RSC Adv*, **2017**, *7*, (9), 5480–5487.

22. Shah, S. A.; Shen, X.; Xie, M.; Zhu, G.; Ji, Z.; Zhou, H.; Xu, K.; Yue, X.; Yuan, A.; Zhu, J.; Chen, Y., Nickel@Nitrogen-Doped Carbon@MoS 2 Nanosheets: An Efficient Electrocatalyst for Hydrogen Evolution Reaction., *Small*, **2019**, *15*, (9).

23. Fernandes, R.; Chunduri, A.; Gupta, S.; Kadrekar, R.; Arya, A.; Miotello, A.; Patel, N., Exploring the hydrogen evolution capabilities of earth-abundant ternary metal borides for neutral and alkaline water-splitting., *Electrochim Acta*, **2020**, *354*.

24. Sitler, S. J.; Raja, K. S.; Charit, I., Metal-Rich Transition Metal Diborides as Electrocatalysts for Hydrogen Evolution Reactions in a Wide Range of pH., *J Electrochem Soc*, **2016**, *163*, (13), H1069–H1075.

25. Park, H.; Encinas, A.; Scheifers, J. P.; Zhang, Y.; Fokwa, B. P. T., Boron-Dependency of Molybdenum Boride Electrocatalysts for the Hydrogen Evolution Reaction., *Angew Chem Int Ed*, **2017**, *56*, (20), 5575–5578.

26. Park, H.; Zhang, Y.; Scheifers, J. P.; Jothi, P. R.; Encinas, A.; Fokwa, B. P. T., Graphene-and Phosphorene-like Boron Layers with Contrasting Activities in Highly Active Mo2B4 for Hydrogen Evolution., *J Am Chem Soc*, **2017**, *139*, (37), 12915–12918.

27. Park, H.; Lee, E.; Lei, M.; Joo, H.; Coh, S.; Fokwa, B. P. T., Canonic-Like HER Activity of Cr1–xMoxB2 Solid Solution: Overpowering Pt/C at High Current Density., *Adv Mate*, **2020**, *32*, (28), 2–7.

28. Park, H.; Zhang, Y.; Lee, E.; Shankhari, P.; Fokwa, B. P. T., High-Current-Density HER Electrocatalysts: Graphene-like Boron Layer and Tungsten as Key Ingredients in Metal Diborides., *ChemSusChem*, **2019**, *12*, (16), 3726–3731.

29. Ai, X.; Zou, X.; Chen, H.; Su, Y.; Feng, X.; Li, Q.; Liu, Y.; Zhang, Y.; Zou, X., Transition-Metal–Boron Intermetallics with Strong Interatomic d–sp Orbital Hybridization for High-Performance Electrocatalysis., *Angew Chem Int Ed*, **2020**, *132*, (10), 3989–3993.

30. Zhuang, Z.; Li, Y.; Li, Z.; Lv, F.; Lang, Z.; Zhao, K.; Zhou, L.; Moskaleva, L.; Guo, S.; Mai, L., MoB/g-C3N4 Interface Materials as a Schottky Catalyst to Boost Hydrogen Evolution., *Angew Chem*, **2018**, *57*, (2), 496–500.

31. Zheng, S.; Fu, Y.; Zheng, L.; Zhu, Z.; Yu, G.; Yang, D., Polypyrrole encapsulating TiB2 as newly-emerged electrocatalyst for highly boosted hydrogen evolution reaction., *Ceram Int*, **2019**, *45*, (17), 23298–23303.

32. Jothi, P. R.; Zhang, Y.; Scheifers, J. P.; Park, H.; Fokwa, B. P. T., Molybdenum diboride nanoparticles as a highly efficient electrocatalyst for the hydrogen evolution reaction., *Sustain Energy Fuels*, **2017**, *1*, (9), 1928–1934.

33. Fokwa, B. P. T.; Misse, P. R. N.; Gilleßen, M.; Dronskowski, R., Sn-flux syntheses, characterizations and bonding analyses of OsB and TiB2., *J Alloys Compd*, **2010**, *489*, (2), 339–342.

34. Jothi, P. R.; Yubuta, K.; Fokwa, B. P. T., A Simple, General Synthetic Route toward Nanoscale Transition Metal Borides., *Adv Mater*, **2018**, *30*, (14), 2–7.

35. He, J.; Bhargav, A.; Manthiram, A., Molybdenum Boride as an Efficient Catalyst for Polysulfide Redox to Enable High-Energy-Density Lithium–Sulfur Batteries., *Adv Mater*, **2020**, *32*, (40).

36. Liu, X.; Gong, Y., A Simple Molten Salt Route to Crystalline β-MoB2Nanosheets with High Activity for the Hydrogen Evolution Reaction., *Inorg Chem*, **2021**, *60*, (23), 18075–18081.

37. Liu, X.; Gong, Y., α-MoB2Nanosheets for Hydrogen Evolution in Alkaline and Acidic Media., *ACS Appl Nano Mater*, **2022**, *5*, (8), 10183–10191.

38. Kravchenko, S. E.; Domashnev, I. A.; Dremova, N. N.; Vinokurov, A. A.; Shilkin, S. P., Synthesis of Vanadium Diboride Nanoparticles via Reaction of Amorphous Boron with Vanadium in KCl and Na2B4O7 Ionic Melts., *Inorg Mater*, **2019**, *55*, (5), 443–448.

39. Wen, T.; Ning, S.; Liu, D.; Ye, B.; Liu, H.; Chu, Y., Synthesis and characterization of the ternary metal diboride solid-solution nanopowders., *J Am Ceram Soc*, **2019**, *102*, (8), 4956–4962.

40. Ma, J.; Du, Y.; Wu, M.; Li, G.; Feng, Z.; Guo, M.; Sun, Y.; Song, W.; Lin, M.; Guo, X., A simple inorganic-solvent-thermal route to nanocrystalline niobium diboride., *J Alloys Compd*, **2009**, *468*, (1–2), 473–476.

41. Ran, S.; Sun, H.; Wei, Y.; Wang, D.; Zhou, N.; Huang, Q., Low-Temperature Synthesis of Nanocrystalline NbB 2 Powders by Borothermal Reduction in Molten Salt ., *J Am Ceram Soc*, **2014**, *97*, (11), 3384–3387.

42. Portehault, D.; Devi, S.; Beaunier, P.; Gervais, C.; Giordano, C.; Sanchez, C.; Antonietti, M., A General Solution Route toward Metal Boride Nanocrystals., *Angew Chem*, **2011**, *123*, (14), 3320–3323.

43. Luo, Y.; Tang, L.; Khan, U.; Yu, Q.; Cheng, H. M.; Zou, X.; Liu, B., Morphology and surface chemistry engineering toward pH-universal catalysts for hydrogen evolution at high current density., *Nat Commun*, **2019**, *10*, (1).

44. Morales-Guio, C. G.; Stern, L. A.; Hu, X., Nanostructured hydrotreating catalysts for electrochemical hydrogen evolution., *Chemical Society Reviews*, **2014**, *43*, (18), 6555–6569.

45. Chen, Y.; Yu, G.; Chen, W.; Liu, Y.; Li, G. D.; Zhu, P.; Tao, Q.; Li, Q.; Liu, J.; Shen, X.; Li, H.; Huang, X.; Wang, D.; Asefa, T.; Zou, X., Highly Active, Nonprecious Electrocatalyst Comprising Borophene Subunits for the Hydrogen Evolution Reaction., *J Am Chem Soc*, **2017**, *139*, (36), 12370–12373.

46. Perdew, J. P.; Burke, K.; Ernzerhof, M., Generalized Gradient Approximation Made Simple., *Phys Rev Lett*, **1996**, *77*, (18), 3865–3868.

47. Kresse, G.; Joubert, D., From ultrasoft pseudopotentials to the projector augmented-wave method., *Phys Rev B*, **1999**, *59*, (3), 1758–1775.

48. Kresse, G.; Furthmü, J., Efficient iterative schemes for ab initio total-energy calculations using a plane-wave basis set., *Phys Rev B*, **1996**, *54*, (16), 169–186.

49. Tang, Q.; Jiang, D. E., Mechanism of hydrogen evolution reaction on 1T-MoS2 from first principles., *ACS Catal*, **2016**, *6*, (8), 4953–4961.

50. Jothi, P. R.; Zhang, Y.; Yubuta, K.; Culver, D. B.; Conley, M.; Fokwa, B. P. T., Abundant vanadium diboride with graphene-like boron layers for hydrogen evolution., *ACS Appl Energy Mater*, **2019**, *2*, (1), 176–181.

51. Skúlason, E.; Karlberg, G. S.; Rossmeisl, J.; Bligaard, T.; Greeley, J.; Jónsson, H.; Nørskov, J. K., Density functional theory calculations for the hydrogen evolution reaction in an electrochemical double layer on the Pt(111) electrode., *Phys Chem Chem Phys*, **2007**, *9*, (25), 3241–3250.

52. Atkins, P. W., *Physical Chemistry 3rd Ed.*, **1985**,.

53. Klemenz, S.; Fries, M.; Dürrschnabel, M.; Skokov, K.; Kleebe, H. J.; Gutfleisch, O.; Albert, B., Low-temperature synthesis of nanoscale ferromagnetic α′-MnB., *Dalton Trans*, **2019**, *49*, (1), 131–135.

54. Kim, H.; Trinkle, D. R., Mechanical properties and phase stability of monoborides using density functional theory calculations., *Phys Rev Mater*, **2017**, *1*, (1).

55. Wang, Y.; Trenary, M., Surface Chemistry of Boron Oxidation. 2. The Reactions of B2O2 and B2O3 with Boron Films Grown on Ta(110)., *Chem Mater*, **1993**, *5*, 199–205.

56. Terlan, B.; Levin, A. A.; Börrnert, F.; Simon, F.; Oschatz, M.; Schmidt, M.; Cardoso-Gil, R.; Lorenz, T.; Baburin, I. A.; Joswig, J. O.; Eychmüller, A., Effect of Surface Properties on the Microstructure, Thermal, and Colloidal Stability of VB2 Nanoparticles., *Chem Mater*, **2015**, *27*, (14), 5106–5115.

57. Silversmit, G.; Depla, D.; Poelman, H.; Marin, G. B.; De Gryse, R., Determination of the V2p XPS binding energies for different vanadium oxidation states (V5+ to V0+)., *J Electron Spectros Relat Phenomena*, **2004**, *135*, (2–3), 167–175.

58. Gupta, S.; Patel, M. K.; Miotello, A.; Patel, N., Metal Boride-Based Catalysts for Electrochemical Water-Splitting: A Review., *Advanced Functional Materials*, **2020**, *30*, (1).

59. Pu, Z.; Liu, T.; Zhang, G.; Liu, X.; Gauthier, M. A.; Chen, Z.; Sun, S., Nanostructured Metal Borides for Energy-Related Electrocatalysis: Recent Progress, Challenges, and Perspectives., *Small Methods*, **2021**, *5*, (10).

60. Jiang, Y.; Lu, Y., Designing transition-metal-boride-based electrocatalysts for applications in electrochemical water splitting., *Nanoscale*, **2020**, *12*, (17), 9327–9351.

61. Wang, F. G.; Liu, X.; Lv, Q. X.; Liu, B.; Chai, Y. M.; Dong, B., Transition Metal Boride-Based Materials for Electrocatalytic Water Splitting., *Chin J Struct Chem*, **2022**, *41*, (9), 2209008–2209044.

62. Yao, Y.; Zhang, Z.; Jiao, L., Development Strategies in Transition Metal Borides for Electrochemical Water Splitting., *Energy Environ Mater*, **2022**, *5*, (2), 470–485.

63. Lee, E.; Fokwa, B. P. T., Nonprecious Metal Borides: Emerging Electrocatalysts for Hydrogen Production., *Acc Chem Res*, **2022**, *55*, (1), 56–64.

64. Sheng, W.; Gasteiger, H. A.; Shao-Horn, Y., Hydrogen Oxidation and Evolution Reaction Kinetics on Platinum: Acid vs Alkaline Electrolytes., *J Electrochem Soc*, **2010**, *157*, (11), B1529.

65. Chung, D. Y.; Park, S. K.; Chung, Y. H.; Yu, S. H.; Lim, D. H.; Jung, N.; Ham, H. C.; Park, H. Y.; Piao, Y.; Yoo, S. J.; Sung, Y. E., Edge-exposed MoS2 nano-assembled structures as efficient electrocatalysts for hydrogen evolution reaction., *Nanoscale*, **2014**, *6*, (4), 2131–2136.

66. Aghamohammadi, P.; Hüner, B.; Altıncı, O. C.; Akgul, E. T.; Teymur, B.; Simsek, U. B.; Demir, M., Recent advances in the electrocatalytic applications (HER, OER, ORR, water splitting) of transition metal borides (MBenes) materials., *International Journal of Hydrogen Energy*, **2024**, *87*, 179–198.

67. Lu, Z.; Zhu, W.; Yu, X.; Zhang, H.; Li, Y.; Sun, X.; Wang, X.; Wang, H.; Wang, J.; Luo, J.; Lei, X.; Jiang, L., Ultrahigh hydrogen evolution performance of under-water 'superaerophobic' MoS2 nanostructured electrodes., *Adv Mater*, **2014**, *26*, (17), 2683–2687.

68. Durst, J.; Siebel, A.; Simon, C.; Hasché, F.; Herranz, J.; Gasteiger, H. A., New insights into the electrochemical hydrogen oxidation and evolution reaction mechanism., *Energy Environ Sci*, **2014**, *7*, (7), 2255–2260.

69. Zhu, L.; Lin, H.; Li, Y.; Liao, F.; Lifshitz, Y.; Sheng, M.; Lee, S. T.; Shao, M., A rhodium/silicon co-electrocatalyst design concept to surpass platinum hydrogen evolution activity at high overpotentials., *Nat Commun*, **2016**, *7*.

70. S. Trasatti; O. Petrii, Real surface area measurements in electrochemistry., *Pure Appl Chem*, **1991**, *63*, (5), 711–734.

71. Hammer, B.; Hansen, L. B.; Nørskov, J. K., Improved adsorption energetics within density-functional theory using revised Perdew-Burke-Ernzerhof functionals., *Phys Rev B*, **1999**, *59*, (11), 7413–7421.

Chapter 3.

Stoichiometric α-MoB_2 and MoB_2/MoB Composites for Ampere-Level Hydrogen Evolution: Tin and Boron Guided Morphology and Phase Design

Sang Bum Kim, Hyeonkyeong Lee, Akira Yasuhara, Kunio Yubuta, Francisco Zaera, Boniface P.T. Fokwa

Transition-metal borides promise conductive, acid-stable HER catalysts but are often obscured by excess-boron residues and poorly controlled morphologies. We report phase-pure, stoichiometric α-MoB_2 nanoparticles synthesized by a Sn/$SnCl_2$ redox-flux route from a 1:2:6 ($MoCl_5$:B:Sn) feed, eliminating excess boron and yielding ~50 nm crystallites. Tuning the B feed and Sn amount affords three benchmarks—1:2:6 (α-MoB_2; MoB_2-SP), 1:8:2.5 (MoB_2/B; excess-B), and 1:2:2.5 (MoB_2/MoB composite)—revealing a two-knob rule: boron sets size/packing, Sn sets phase/morphology. Despite unfavorable surface area and agglomeration, stoichiometric α-MoB_2 exhibits strong intrinsic activity. In stationary (non-rotating) carbon cloth tests (0.5 M H_2SO_4), α-MoB_2 reaches η_{150} = 203 mV and η_{1000} = 393 mV; a MoB_2/MoB composite, obtained by Sn/B tuning, achieves η_{150} = 173 mV and η_{1000}= 361 mV, surpassing Pt/C at 1 A·cm^{-2} under identical conditions. The performance arises from phase synergy, preserved Mo–B terminations, and suppressed B-overcoats, enabling ampere-level HER with earth-abundant Mo–B catalysts.

3.1. Introduction

Hydrogen has emerged as a crucial clean-energy carrier in the pursuit of decarbonization.[1] Water electrolysis, among various production pathways, offers a sustainable route to high-purity H_2 via the hydrogen evolution reaction (HER) at the cathode.[2] However, the efficiency and cost of electrolyzers depend critically on the HER catalysts. Platinum (Pt) remains the benchmark due to its near-zero overpotential and fast kinetics.[3] Unfortunately, Pt's scarcity and high cost severely limit its large-scale use, motivating extensive efforts to develop earth-abundant alternatives capable of matching or surpassing Pt's performance.[4–6]

Over the past decade, significant advances have been made in exploring non-precious HER electrocatalysts based on transition metal compounds.[7,8] Prominent examples include transition metal chalcogenides (e.g. MoS_2),[9] phosphides (e.g. Ni_2P, CoP),[10,11] carbides and nitrides (e.g. Mo_2C, W_2C, Co_4N),[12–14] as well as various metal alloys and heterostructures.[15–17] Many of these materials exhibit impressive HER activity, especially when optimally nanostructured or compositionally tuned, with some approaching, or even surpassing, the efficiency of Pt in either acidic or alkaline media.[18,19] For instance, MoS_2 catalysts were shown to drive HER at modest overpotentials once active edge sites are exposed.[20] Likewise, Ni_2P has achieved high current densities in acidic electrolyte.[10] Theoretical screening and volcano-plot analyses have further guided the discovery of catalysts with near-optimal hydrogen binding energetics.[21] Nevertheless, most noble-metal-free catalysts still require substantially higher overpotentials than Pt (typically around 150 mV at 10 $mA \cdot cm^{-2}$) and often suffer from durability issues in corrosive

media.[22,23] These challenges become especially pronounced under the high current densities ($A \cdot cm^{-2}$) relevant to industrial water electrolysis. [24,25] Achieving catalysts that remain highly active and stable at such large currents remains a critical hurdle. Accordingly, recent research has increasingly focused on catalyst systems that can sustain high performance under practical, high-current conditions.

Transition metal borides (TMBs) have recently emerged as a particularly promising class of HER electrocatalysts to meet these demanding requirements.[26] TMBs combine abundant metals (e.g. Ni, Co, Mo, W) with boron, an element that imparts high electrical conductivity and unique metal–boron bonding environments.[27] In contrast to chalcogenides or phosphides, many borides are intrinsically metallic with robust crystal structures, suggesting excellent HER kinetics and strong corrosion resistance.[28,29] Early studies indeed found that incorporating boron into transition metals can dramatically enhance catalytic performance. For example, amorphous cobalt–boron alloys catalyze H_2 evolution across a wide pH range with remarkable stability, and amorphous nickel–boron (Ni–B) catalysts exhibit HER activity approaching that of Pt, along with outstanding long-term stability.[30,31] Such findings established boron alloying as a powerful strategy to create highly active and durable HER catalysts from base metals. Building on the successes of amorphous borides, subsequent work has explored crystalline TMB phases, revealing exceptional HER activity in several cases.

Among TMBs, molybdenum diboride (MoB_2) has attracted particular attention as an HER catalyst because of its favorable AlB_2-type crystal structure and chemical stability. In α-MoB_2, layers of molybdenum atoms alternate with flat hexagonal boron sheets that

provide near-optimal hydrogen-binding sites, as supported by both theory and experiments.[32] Consistently, bulk molybdenum borides show high HER activity in acid, and within the series, boron-richer phases (MoB_2, β-MoB) outperformed the boron-poorer Mo_2B, demonstrating a clear "boron dependency" trend in catalytic performance. A recent review also highlights rapid progress in Mo borides and the emergence of 2D MBene-like boron sheets.[33] Notably, even the polymorphs of MoB_2 show divergent activities, where the α-phase (with graphene-like flat boron sheets) showed much higher HER activity than the β-phase (with puckered, phosphorene-like boron layers), underscoring the impact of boron layer structure on catalysis.[34,35] Partial substitution of Mo with other metals provides another pathway to optimize MoB_2. For example, 30% W-substituted MoB_2 was reported to retain comparatively lower overpotentials at current densities of 150 $mA \cdot cm^{-2}$ than pure MoB_2 and substituting 40% of Mo with Cr enabled sustained HER with an overpotential 150 mV lower than that of Pt/C at higher current density of ~800 $mA \cdot cm^{-2}$.[36,37] Very recently, self-supported α-MoB/β-MoB_2 ceramic electrodes achieved 289–294 mV at 1 $A \cdot cm^{-2}$ across acidic and alkaline media through macroporous channels that enhance transport and interfacial charge transfer.[38]

Nanostructuring TMB catalysts further enhances their HER performance. In 2017, Jothi *et al.* synthesized MoB_2 nanocrystals (~50-100 nm) via a solid-state metathesis route, achieving an overpotential of 154 mV at 10 $mA \cdot cm^{-2}$ in acid.[39] This improvement over bulk MoB_2 is consistent with nanosizing effects that increase electrochemically active surface area and expose more active sites. However, because boron has a very high melting point, boride nanoparticle syntheses often suffer from large particle sizes, uncontrolled

crystallization, and mixed phases.[40] To lower reaction temperatures and improve phase control, researchers commonly employ flux-assisted or solution routes—most notably molten-salt methods, as described by Portehault *et al*.[41] Using this molten-salt method, Liu and Gong have successfully synthesized ultrathin nanosheets for both β-MoB and α-MoB_2 that each delivered ~187 and ~124 mV overpotential at 10 $mA \cdot cm^{-2}$ in alkaline media with great stability.[42] These advances have cemented MoB_2 and related borides among the most promising non-precious HER catalyst. In 2018, Jothi *et al.* introduced a simple, general $Sn/SnCl_2$ redox route to nanoscale transition metal borides.[43] Using this approach, they obtained nano-vanadium diboride (VB_2), that required an overpotential of 192 mV at 10 mA cm^{-2} (vs 348 mV for bulk-VB_2).[44] Notably, our most recent work employed the same Sn-redox strategy to prepare vanadium-stabilized MoB nanoparticles that achieved ~1000 mA cm^{-2} at ~0.45 V with ~97% retention over ~28 h, outperforming Pt/C under identical conditions and highlighting the relevance of flux-controlled borides for high-current HER.[45]

While molybdenum borides (MoB, MoB_2, Mo_2B) clearly show exceptional HER activity, regardless of their composition, the practical challenge has been the synthesis of phase-pure, nanostructured molybdenum borides with controlled stoichiometry. Conventional solid-state and solution-phase routes frequently rely on large excesses of boron precursors (e.g. borane or $NaBH_4$) to drive boride formation, which can leave boron-rich impurities or amorphous coatings that obscure intrinsic activity and impede conductivity.[41,42,46] In Sn-redox syntheses, excess boron in the feed is likewise employed to access targeted molybdenum boride phases, increasing the risk of electronically

insulating residues that compromise performance.[43] Even in solid-state metathesis routes to MoB_2, the use of excess boron has been associated with residual MoB as a secondary phase in the product.[39] Such boron residues and secondary phases complicate a rigorous assessment of MoB_2's intrinsic catalytic properties, underscoring the need for synthetic strategies that deliver stoichiometric, phase-pure MoB_2 nanoparticles without surplus amorphous boron or amorphous by-products. As a related demonstration of composition control without boron overload, partial vanadium substitution enabled single-phase MoB with a 1:1 B:Mo ratio directly from the feed.[45]

There are three common HER benchmarking configurations, thin-film rotating disk electrodes (RDEs), porous carbon substrates, and self-supported binder-free electrodes, each emphasizing different aspects of activity, transport, and durability.[47,48] Rotating-disk electrodes (RDEs) are invaluable for screening intrinsic kinetics on ultrathin films, but they can overestimate activity relative to stationary, device-like electrodes where through-plane transport and bubble management dominate at ≥0.5–1 A cm^{-2}. [49,50] To emulate practical operation, we therefore adopt stationary porous electrodes that allow high loadings and realistic gas–liquid transport.[51–54] Carbon cloth (CC) is particularly suitable: it is commercially accessible, easy to process, supports large catalyst inventories, and mirrors the porous-transport architectures used in stacks without the surface-treatment needs of Ti foams/PTLs.[55–57] CC also avoids rotation artifacts, enabling fair comparison across current regimes and preserving ohmic pathways under vigorous gas evolution. [58,59] While self-supported architectures can minimize interfacial resistances,[38] they consume more active material and complicate rapid composition–structure screening.[60,61] Using CC thus

balances practical transport with experimental throughput, aligning our tests with the ≥0.5–1 A cm^{-2} targets relevant to industrial electrolysis while retaining clear structure–performance readouts.

Herein, we report the synthesis of phase-pure, stoichiometric α-MoB_2 nanoparticles without excess boron via a Sn/$SnCl_2$-mediated redox-flux method. Using a stoichiometric metal:boron feed (1:2) with excess Sn yields α-MoB_2 crystallites free of secondary phases and amorphous-B residues. In 0.5 M H_2SO_4, α-MoB_2 delivers 203 mV at 150 mA·cm^{-2} and 393 mV at 1 A·cm^{-2} despite a less favorable morphology and lower surface area, underscoring the intrinsically high HER activity of stoichiometric MoB_2. By contrast, conventional MoB_2 prepared from excess-boron feeds often carries amorphous-B overcoats that degrade conductivity and mask intrinsic activity. The best performance was obtained from a MoB_2/MoB composite, tuned via the Sn/B feed, achieving 173 mV at 150 mA·cm^{-2} and 361 mV at 1 A·cm^{-2}, outperforming Pt/C at 1 A·cm^{-2} under identical conditions. We attribute these gains via synergy between two intrinsically active boride phases and flux/boron-controlled growth that preserves fully conductive boride surfaces while promoting smaller, uniform particles, enabling ampere-level HER with earth-abundant Mo–B catalysts.

3.2. Experimental Section

3.2.1. Chemicals

Molybdenum Chloride ($MoCl_5$, powder, 99.95 %), boron (amorphous powder, 99 %) and Platinum on carbon (Pt/C, 20 %) were obtained from Alfa Aesar. Sulfuric acid (H2SO4, 98 %) was purchased from Fisher Scientific. Copper sheet and conductive carbon glue were obtained from Basic copper, Ted pella, respectively. All chemicals were used without further purification.

3.2.2. Sample preparation

All of the chemicals used in the experiment were handled in a nitrogen-filled glovebox. Anhydrous molybdenum source, $MoCl_5$, elemental boron, and Sn powder were mixed in a mortar and pressed into a pellet in the glovebox. The pellet was then sealed in a quartz ampoule under vacuum or argon atmosphere. Different mole compositions ($MoCl_5$:B:Sn) used for different samples, specifically 1:2:2.5 for MoB_2/MoB, 1:2:6.0 for MoB_2-SP, and 1:8:2.5 for MoB_2/B. The sealed quartz ampoule containing the pellet was then heated in an electric furnace for 4 hours at 800°C with 2°C/min heating and cooling rate. Upon completion of the reaction, the ampoule was opened to reveal a dark-colored product (pellet), which was then ground into powder and treated in approximately 10% concentrated HCl for one hour before washed with deionized water and ethanol, then dried overnight at 65°C. X-ray diffraction analysis confirmed that the resulting powder of MoB_2-SP and MoB_2/B exhibited a single crystalline phase α-MoB_2 (space group P6/mmm, ICSD No.1510763), while MoB_2/MoB displayed a secondary phase of MoB (space group I41/amd, ICSD No.9008953).

3.2.3. Electrode preparation

4 mg of each synthesized powder was ultrasonically dispersed in 1 mL of ethanol with 20 μL of a 5% Nafion solution (Sigma Aldrich) for 30 min to form a homogeneous catalyst slurry. Then the slurry catalyst mixture was coated over a carbon cloth (Sigracet) with an area of 3×3 mm^2. Finally, the catalyst-coated carbon cloth was dried at 70 °C for 120 minutes in an oven to remove the solvent from the electrode and to improve the bonding. Then the catalyst coated carbon cloth was attached to a copper sheet using conductive silver paste. The exposed surface of the copper sheet was covered with epoxy adhesive and dried overnight at room temperature. The catalyst loading of the electrode was kept at ~1 mg/cm^2 for all the samples analyzed.

3.3. Results and Discussion

Molybdenum boride nanoparticles were synthesized via a Sn/$SnCl_2$-mediated redox-flux route, affording three benchmark products from $MoCl_5$:B:Sn feeds of 1:2:2.5 (assigned MoB_2/MoB), 1:2:6 (MoB_2-SP), and 1:8:2.5 (MoB_2/B). Powder X-ray diffraction (**Figure 3.1a-c**) shows that the 1:2:2.5 route—using stoichiometric B and the stoichiometric Sn required for $MoCl_5$ reduction, yields a MoB_2/MoB composite, whereas both 1:2:6 (stoichiometric B, excess Sn) and 1:8:2.5 (excess B, stoichiometric Sn) crystallize as single-phase α-MoB_2 (AlB_2-type, *P6/mmm*). In the composite, reflections from the MoB second phase exhibit pronounced preferred orientation (red asterisks, **Figure 3.1a**), consistent with previous observations for MoB produced by the same Sn-redox approach.[45] EDS elemental maps confirm uniform spatial distributions of Mo and B for all

three samples (**Figure 3.1d–f**), with the corresponding spectra compiled in **Figure 3.2**. Quantitative EDS (**Table 3.1**) gives B:Mo atomic ratios of 3.15 for MoB_2/MoB (24.1 at% Mo, 75.9 at% B), 2.12 for MoB_2-SP (32.1 at% Mo, 67.9 at% B), and 6.81 for MoB_2/B (12.8 at% Mo, 87.2 at% B), consistent with near-stoichiometric α-MoB_2 for MoB_2-SP, substantial B excess retained in MoB_2/B prepared from the 1:8:2.5 feed, and modest B-enrichment in the composite.

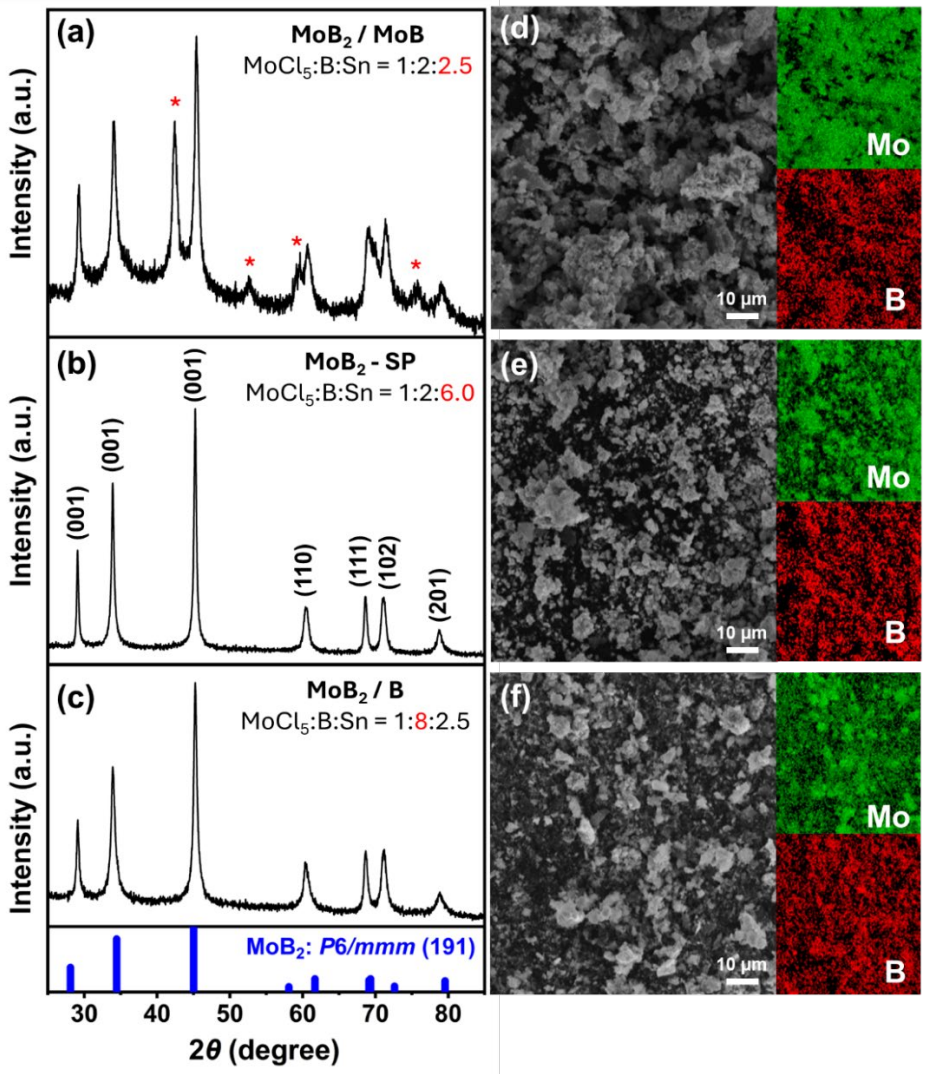

Figure 3.1. Powder X-ray diffraction patterns of synthesized (a) MoB_2/MoB, (b) MoB_2-SP, and (c) MoB_2/B. Energy dispersive X-ray spectroscopy (EDS) elemental mapping of Mo and B in (d) MoB_2/MoB, (e) MoB_2-SP, and (f) MoB_2/B.

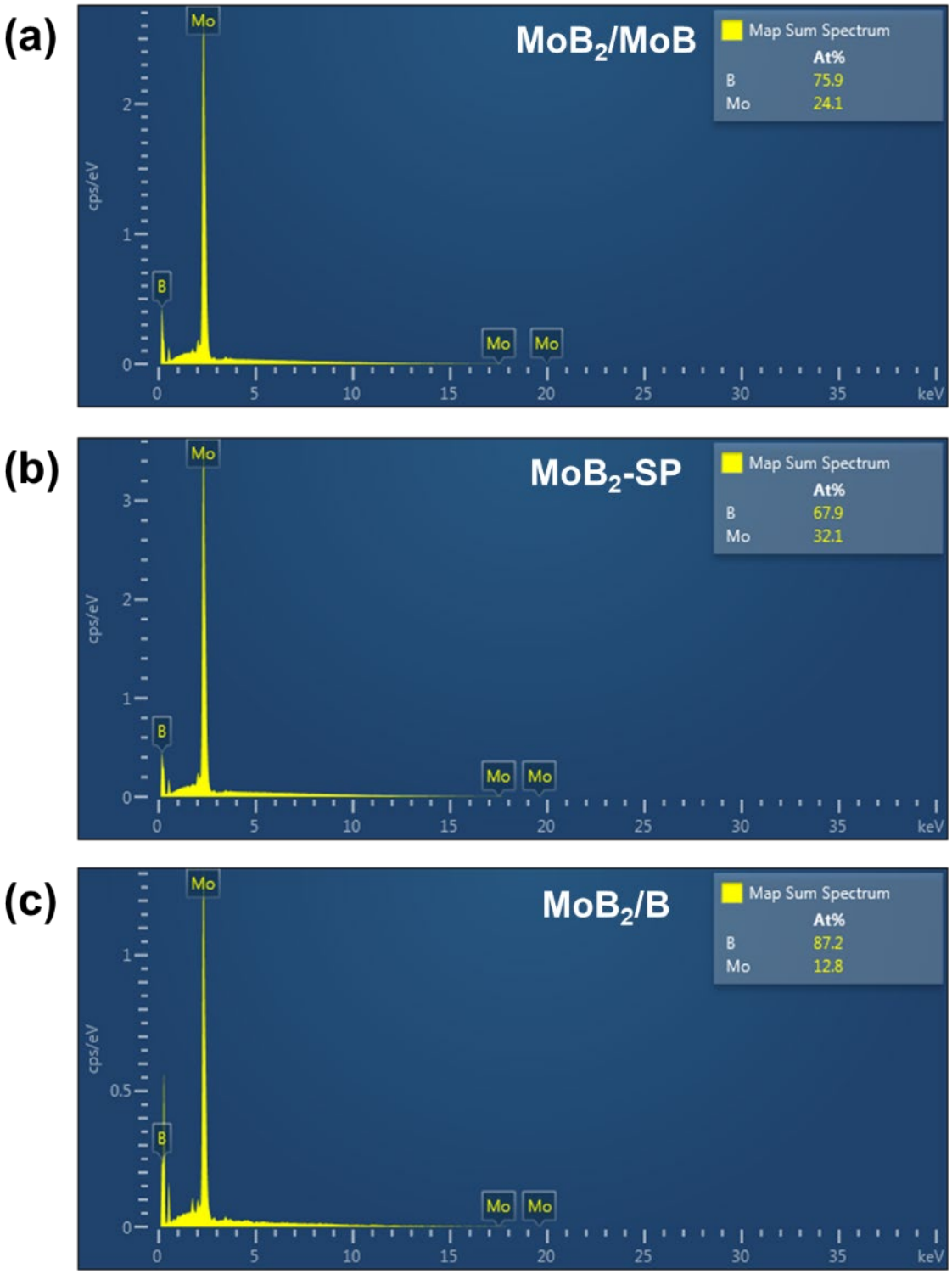

Figure 3.2. EDS elemental spectra associated with EDS mapping in Figure 3.1 of (a) MoB_2/MoB, (b) MoB_2-SP, and (c) MoB_2/B.

Scanning electron microscopy (SEM, **Figure 3.3a-c**) reveals distinct morphologies across the series: MoB_2/MoB presents relatively uniform granular nanoparticles (**Figure 3.3a**), MoB_2-SP shows a heterogeneous mixture of nanoneedles and thin plates that agglomerate into higher-order clusters (**Figure 3.3b**), and MoB_2/B displays the smallest, most uniform primaries (**Figure 3.3c**). The particle-size evolution broadly follows the molten-salt literature, smaller particles with higher B in the feed.[41] However, unlike molten-salt syntheses where excess salt constrains growth,[62] the Sn-redox medium behaves oppositely at high Sn: for MoB_2-SP (stoichiometric B, excess Sn) the primaries and aggregates become larger rather than smaller, indicating a flux-dominated aggregation regime with a higher crystal/particle growth rate.

Table 3.1. Composition of the three samples measured from EDS (**Figure 3.1** & **3.2**).

Sample	Mo (at%)	B (at%)	B/Mo Ratio
MoB_2/MoB	24.1	75.9	3.15
MoB_2-SP	32.1	67.9	2.12
MoB_2/B	12.8	87.2	6.81

Table 3.2. Textural parameters from N_2 physisorption at 77 K. Specific surface area (S_{BET}) was obtained by multipoint BET from adsorption branch. Total pore volume (V_{pore}) was derived from the QSDFT-Ads analysis (N_2 @ 77K; mixed slit/cylindrical kernel)

Sample	Specific surface area ($m^2 g^{-1}$)	Pore volume ($cm3 g^{-1}$)
MoB_2/MoB	**15.78**	**0.0482**
MoB_2-SP	**8.32**	**0.0305**
MoB_2/B	**34.68**	**0.0527**

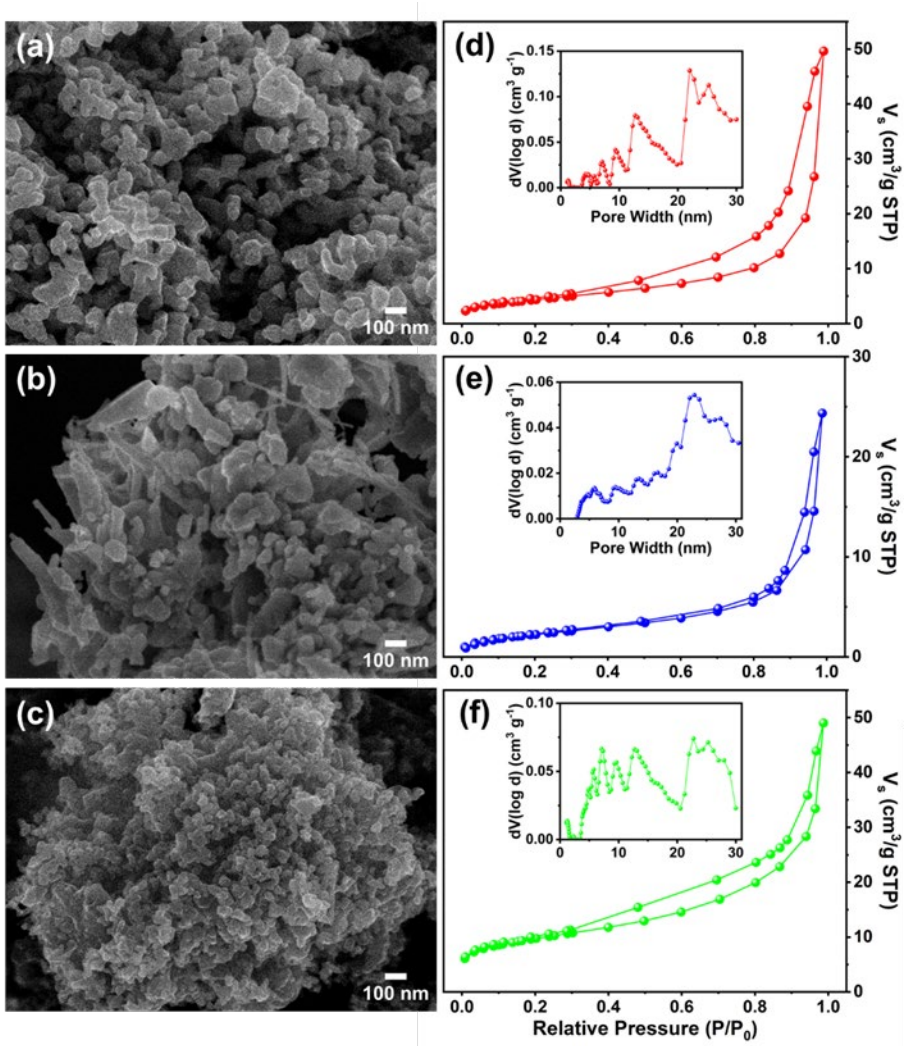

Figure 3.3. SEM images of (a) MoB_2/MoB, (b) MoB_2-SP, and (c) MoB_2/B. BET isotherms of (d) MoB_2/MoB, (e) MoB2-SP, and (f) MoB2/B, and the insets showing pore volume distribution.

The N_2 adsorption–desorption isotherms (**Figure 3.3j-l**) for all three samples are type-IV with pronounced H3 hysteresis, consistent with mesoporous textures arising from interparticle packing of plate/flake–particle aggregates; the very low uptake at $P/P_0 \approx 0.01$ indicates negligible intrinsic microporosity, so accessible porosity derives predominantly from interparticle slits/cavities. BET specific surface areas, determined from the adsorption

branch under Rouquerol criteria, are S_{BET} = 34.68 m^2 g^{-1} (MoB_2/B), 15.78 m^2 g^{-1} (MoB_2/MoB), and 8.32 m^2 g^{-1} (MoB_2-SP) (**Table 3.2**). Pore-size distributions (PSDs; insets, **Figure 3.3j-l**) were obtained from the adsorption branch using QSDFT for N_2 at 77 K with a mixed slit/cylindrical kernel (instrument/analysis details in the SI), yielding peak modes at ~5–12 nm (MoB_2/B), ~13–15 nm (MoB_2/MoB), and ~25–40 nm (MoB_2-SP). Corresponding pore volumes from QSDFT are 0.0482 cm^3 g^{-1} (MoB_2/MoB), 0.0305 cm^3 g^{-1} (MoB_2-SP), and 0.0527 cm^3 g^{-1} (MoB_2/B), tracking the S_{BET} trend (MoB_2/B > MoB_2/MoB > MoB_2-SP) and reflecting progressively wider interparticle voids and stronger agglomeration as B feed decreases and/or Sn increases. Together with SEM, these analyses establish that B-feed controls primary size/packing, while Sn-flux governs aggregate growth and particle morphology.

QSDFT was employed rather than classical BJH because (i) the SEM-observed mixture of stacked plates/flakes and particulate clusters naturally generates both slit-like and cylindrical/interstitial voids, best represented by a mixed-geometry kernel, and (ii) in H3-type systems the desorption branch is influenced by network percolation/cavitation, which biases desorption-based models (BJH/Kelvin) and can redistribute pore volume across the mesopore range. Accordingly, we report QSDFT-Ads PSDs (mixed slit/cyl kernel) alongside adsorption-branch, Rouquerol-validated BET areas as standard measures of texture.

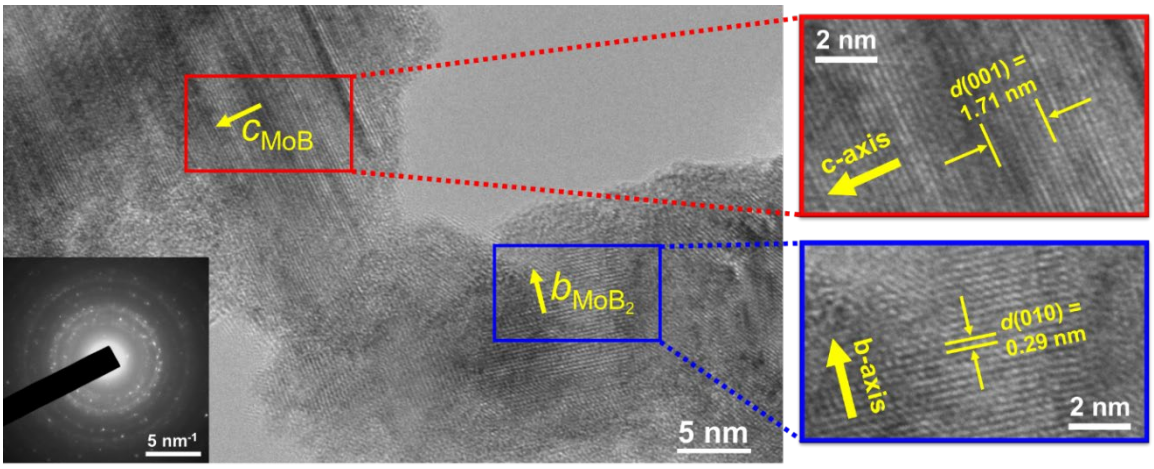

Figure 3.4. HRTEM image of MoB_2/MoB nanoparticles with MoB c-lattice and MoB_2 b-lattice

High-resolution TEM for the composite (**Figure 3.4**), resolves MoB (001) and α-MoB_2 (010) domains within single particles; the SAED inset is non-uniform, reflecting multiphase character. Lattice-fringe indexing highlights the (001) planes of MoB and the (010) planes of α-MoB_2, consistent with the XRD assignment. Stacking faults frequently occur in the MoB lamellae—an expected feature for monoborides produced via Sn-redox synthesis and consonant with earlier observations for the same structure using the same method.[45]

For XPS Mo 3d (**Figure 3.5a-c**), all three samples exhibit the characteristic boride/metallic low-binding energy (BE) envelope composed of a minor Mo^0 doublet at 227.8–227.9 eV ($3d_{5/2}$) and 230.5–230.7 eV ($3d_{3/2}$) with very narrow widths (FWHM ≈ 0.39–0.50 eV), together with the Mo–B related component centered near ≈ 228–231 eV. Higher-BE contributions from Mo^{4+} (MoO_2-like) appear at 229.3 ± 0.1 eV ($3d_{5/2}$) and 232.3–232.4 eV ($3d_{3/2}$) with FWHM ≈ 1.0–1.2 eV, and a small Mo^{6+} doublet at 232.7–

232.8/235.8–236.0 eV (FWHM ≈ 2.4–2.7 eV). The overall line shapes (intensity, area, widths) are very similar across the three samples, and the Mo^0 fraction remains small—as expected for nanosized borides.[39,45] Notably, the low-BE Mo–B/Mo^0 envelope is comparably pronounced in MoB_2-SP (**Figure 3.5b**) and MoB_2/MoB (**Figure 3.5a**), but least evident in MoB_2/B (**Figure 3.5c**). This sequence tracks the HER trend, supporting that accessible Mo-B terminations (low-BE Mo signal) are performance-relevant for MoB_2-based catalysts.[63]

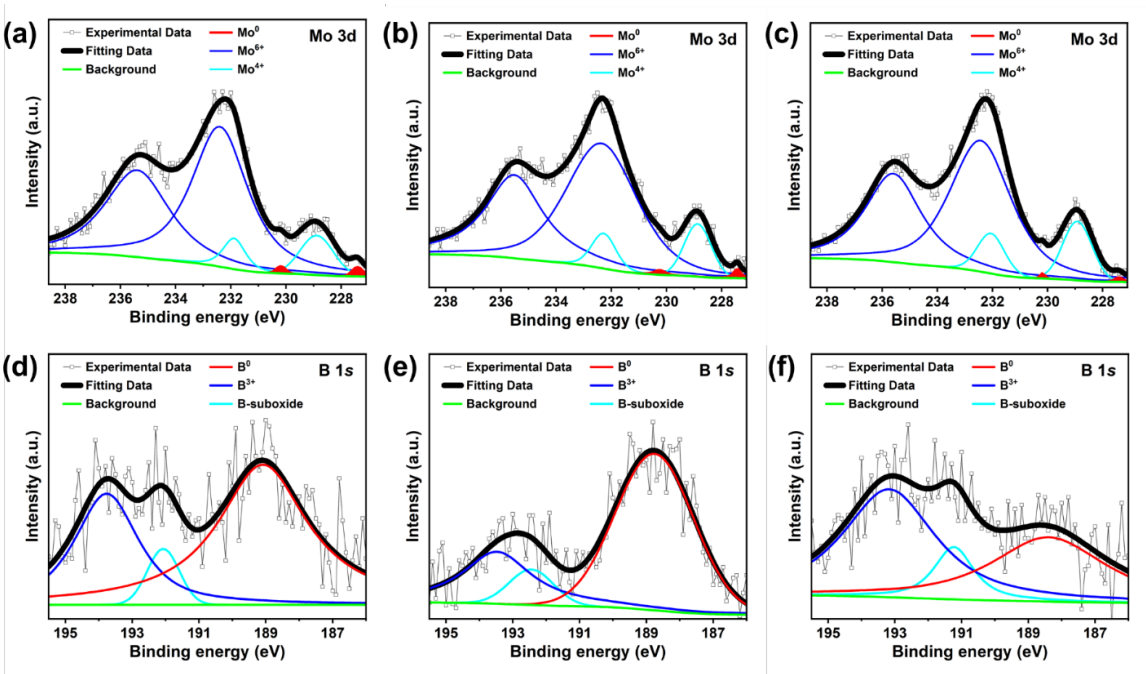

Figure 3.5. High-resolution XPS spectra of Mo 3d, B 1s and O 1s of MoB_2/MoB (a–c), MoB_2-SP (d–f), and MoB_2/B (g–i).

Table 3.3. XPS peak position and full width at half maximum (FWHM) parameters for Mo 3d and B1s of MoB_2/MoB, MoB_2-SP, and MoB_2/B

Sample	Assigned Species	Spin-orbit Components	Peak Position (eV)	FWHM (eV)
MoB_2/MoB	Mo^{6+} (MoO_3)	$3d_{5/2}$	232.82	2.57
		$3d_{3/2}$	235.82	2.67
	Mo^{4+} (MoO_2)	$3d_{5/2}$	229.28	1.41
		$3d_{3/2}$	232.34	1.06
	Mo^0 (MoB_2/MoB)	$3d_{5/2}$	227.81	0.487
		$3d_{3/2}$	230.57	0.459
	B^{3+} (B_2O_3)		235.82	3.22
	B-suboxide (B_2O2)		232.82	2.57
	B^0 (MoB_2/MoB)		189.09	2.67
MoB_2-SP	Mo^{6+} (MoO_3)	$3d_{5/2}$	232.75	3.03
		$3d_{3/2}$	235.91	2.47
	Mo^{4+} (MoO_2)	$3d_{5/2}$	229.27	1.15
		$3d_{3/2}$	232.68	1.03
	Mo^0 (MoB_2/MoB)	$3d_{5/2}$	227.84	0.497
		$3d_{3/2}$	230.65	0.435
	B^{3+} (B_2O_3)		193.47	2.48
	B-suboxide (B_2O2)		192.44	1.56
	B^0 (MoB_2/MoB)		188.76	2.76
MoB_2/B	Mo^{6+} (MoO_3)	$3d_{5/2}$	232.83	2.62
		$3d_{3/2}$	236.00	2.4
	Mo^{4+} (MoO_2)	$3d_{5/2}$	229.32	1.24
		$3d_{3/2}$	232.45	1.16
	Mo^0 (MoB_2/MoB)	$3d_{5/2}$	227.81	0.390
		$3d_{3/2}$	230.58	0.410
	B^{3+} (B_2O_3)		193.17	3.23
	B-suboxide (B_2O2)		191.23	1.41
	B^0 (MoB_2/MoB)		188.39	4.07

Table 3.4. Composition of the three samples measured from XPS.

Sample	Mo (at%)	B (at%)	B/Mo Ratio
MoB_2/MoB	23.44	76.56	3.27
MoB_2-SP	31.03	68.97	2.22
MoB_2/B	14.12	85.88	6.08

The B 1s spectra (**Figure 3.5d–f**) differentiate the surface chemistry. Each sample contains a B^0 (Mo-B) peak at ≈188.3-188.9 eV, a B-suboxide shoulder at ≈191.1–191.6 eV, and a higher-BE B^{3+} (B_2O_3/borate-like) component at ≈192.8–193.5 eV. In MoB_2-SP (**Figure 3.5e**) the B^0 ≈188.8 eV peak dominates while the oxide contributions at ≈191–193 eV are weak (**Table 3.3**: B^0 FWHM ≈ 2.8 eV), indicating that most surface B participates in Mo–B bonding rather than forming oxides. MoB_2/B (**Figure 3.5f**) shows the opposite behavior: a strong B^{3+} ≈193.2 eV and a pronounced B-suboxide ≈191.2 eV, together with a broadened B^0 (FWHM ≈ 4.1 eV), consistent with excess/heterogeneous B that readily oxidizes. MoB_2/MoB (**Figure 3.5d**) lies between these limits, with a sizable B^0 ≈188.7–188.9 eV and moderate oxide intensity.[39,44,45,63] Overall, the B 1s evolution, B^0-rich in MoB_2-SP, intermediate in MoB_2/MoB, and oxide-rich in MoB_2/B, aligns with the low-BE Mo trend above.

Quantitative XPS composition (**Table 3.4**) further corroborates these assignments. The surface Mo and B atomic fractions are 23.44/76.56 at% for MoB_2/MoB, 31.03/68.97 at% for MoB_2-SP, and 14.12/85.88 for MoB_2/B. Expressed as B:Mo ratio, the values are 3.27 (MoB_2/MoB), 2.22 (MoB_2-SP), and 6.08 (MoB_2/B), indicating a B-rich surface for the B-added sample and a comparatively lower B:Mo for the SP product. These XPS-derived B:Mo trends match the EDS measurements in **Figure 3.1** and **Figure 3.2**, which likewise show MoB_2/B as the most B-loaded, MoB_2/MoB intermediate, and MoB_2-SP the least B-enriched. Together with the peak-shape analysis, the compositional data reinforce that maximizing low-BE Mo–B (~227.8-231 eV) and B^0 (~188.5-188.9 eV) while

suppressing high-BE B-oxide (~191-193.5 eV) correlates with the superior HER activity observed for the MoB_2/MoB and MoB_2-SP catalysts.

The HER performance of the Mo–B nanoparticle catalysts was evaluated in 0.5 M H_2SO_4 using a three-electrode configuration on stationary carbon cloth (CC). **Figure 3.6a,d** shows the polarization curves (iR-corrected LSVs) for the three samples. All samples exhibit efficient catalytic activity, reaching the 150 $mA \cdot cm^{-2}$ benchmark at relatively low overpotentials (η_{150}). At 150 $mA \cdot cm^{-2}$, MoB_2/MoB, MoB_2-SP, and MoB_2/B required 173, 203, and 281 mV, respectively. At the lower current density of 10 $mA \cdot cm^{-2}$ (**Figure 3.7**), where the Pt/C is best with $\eta_{10} \approx 30–40$ mV, the MoB_2/MoB composite leads the boride electrodes, requiring only 96 mV; Notably, at this low current density our MoB_2-based catalysts are within ~60 mV of Pt—an impressive level for a noble-metal-free material. More importantly, the borides maintain their advantage as current increases, as discussed next.

A primary motivation for developing robust non-noble catalysts is to meet the demands of industrial electrolysis, which operates at high current densities (≥ 500 $mA \cdot cm^{-2}$). We therefore measured the overpotentials required to reach 1 $A \cdot cm^{-2}$ for each sample (**Figure 3.6d**). Again, the MoB_2/MoB sample excelled, delivering 1 $A \cdot cm^{-2}$ at 361 mV. Notably, this outperforms Pt/C—under identical conditions, the commercial Pt/C electrode required ~0.826 V to reach 1 $A \cdot cm^{-2}$, more than twice the overpotential of MoB_2/MoB. MoB_2-SP reached 1 $A \cdot cm^{-2}$ at ~393 mV, while the B-rich MoB_2/B sample required ~516 mV to drive the same current. These results demonstrate a remarkable sensitivity of high-current performance to the Mo–B feed ratio (and resulting phase purity). Despite

agglomeration evident in SEM and lower S_{BET}, MoB_2-SP shows very good performance at both low and high current density, underscoring the intrinsic activity of stoichiometric α-MoB_2. By contrast, MoB_2/B, with its large excess of boron, likely forms insulating/oxidized B overcoats that inhibit access/conductivity as was evident from Portehault et al.[41] For the MoB_2/MoB composite, modest B-excess in EDS/XPS, reduced agglomeration (BET), and phase synergy together boost activity.

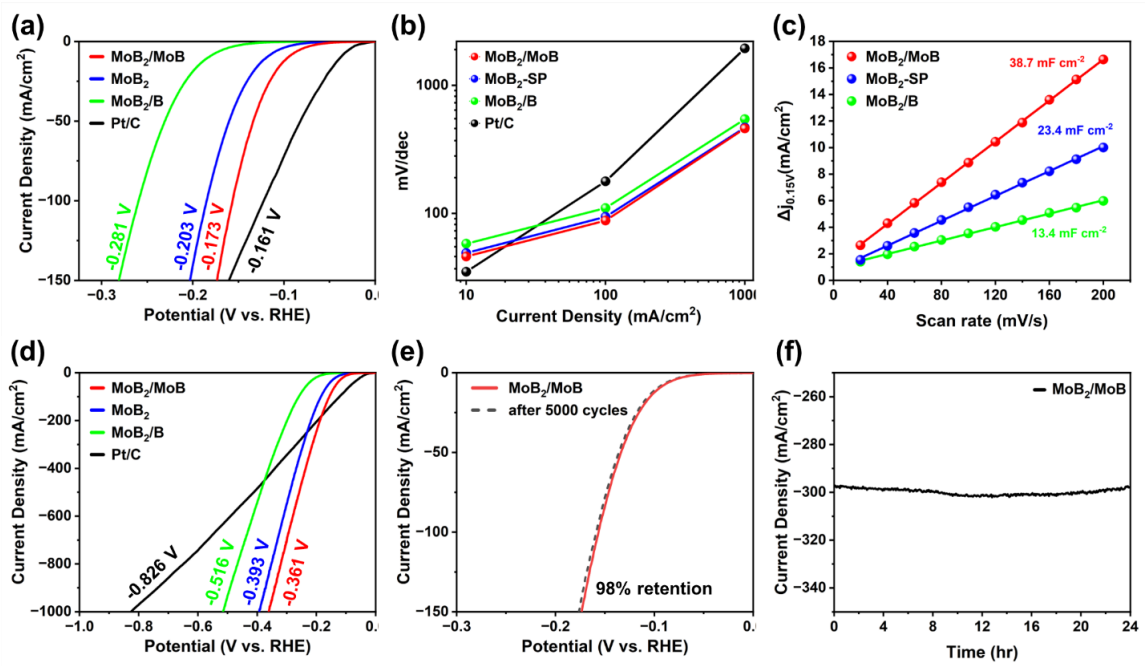

Figure 3.6. Linear sweep polarization curves of different electrodes of MoB_2/MoB, MoB_2-SP, MoB_2/B and 20% Pt/C recorded in 0.5 M H_2SO_4 to reach (a) 150 mA cm^{-2} and (d) 1000 mA cm^{-2}. (b) Tafel slopes of these materials at different current densities. (c) Charging current density difference plotted against scan rate to yield double-layer capacitance (C_{dl}) of the boride samples. (e) Polarization curves of MoB_2/MoB electrode before and after 5000 cycles. (f) Chronoamperometry curve of MoB_2/MoB electrode for 24 h.

Table 3.5. Fitted EIS data from Nyquist Plots in **Figure 3.9**.

Electrode type	R_s [Ohm]	R_{ct} [Ohm]	CPE [F s^{a-1}]	a
MoB_2/MoB	10.2	24.4	3.69 e^{-3}	0.841
MoB_2-SP	9.6	31.9	3.20 e^{-3}	0.810
MoB_2/B	10.4	53.6	2.35 e^{-3}	0.760

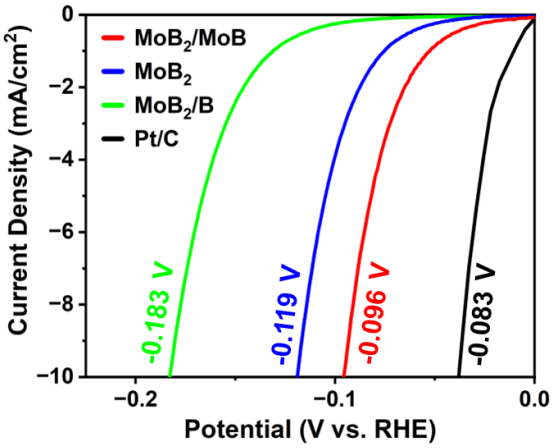

Figure 3.7. Linear sweep polarization curves of different electrodes of MoB_2/MoB, MoB_2-SP, MoB_2/B and 20% Pt/C recorded in 0.5 M H_2SO_4 to 10 mA cm^{-2}.

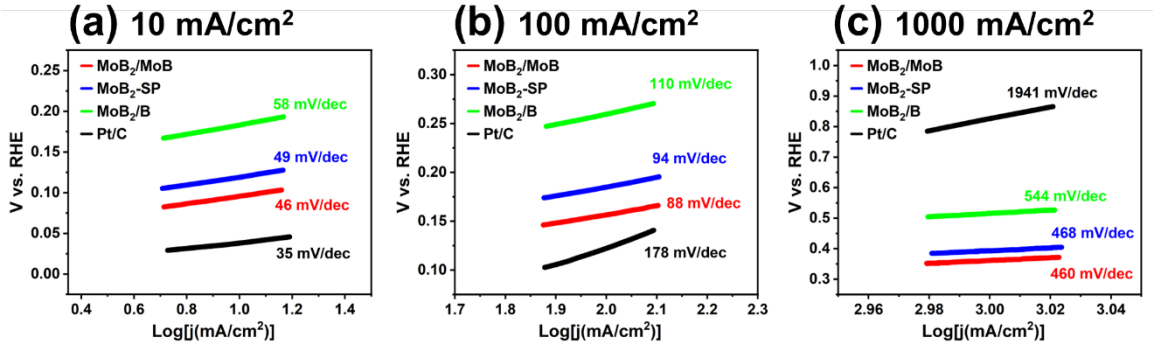

Figure 3.8. Tafel plots of MoB_2/MoB, MoB_2-SP, MoB_2/B and Pt/C electrodes at different current densities of (a) 10, (b) 100, and (c) 1000 mA cm^{-2}.

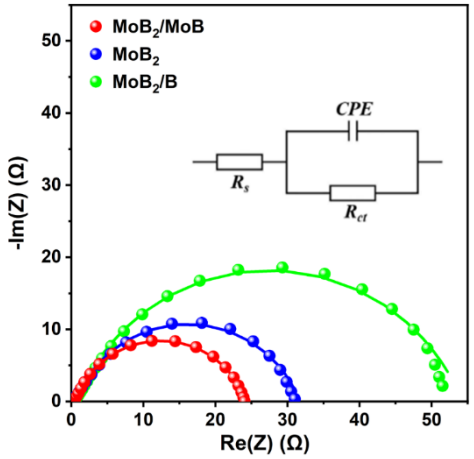

Figure 3.9. Nyquist plot representations of the electrochemical impedance spectra of the boride samples of (red) MoB_2/MoB, (blue) MoB_2-SP, and (green) MoB_2/B.

Tafel slopes were calculated at 10, 100, and 1000 $mA \cdot cm^{-2}$, as shown in **Figure 3.8**. At 10 $mA \cdot cm^{-2}$, Pt/C shows 35 $mV \cdot dec^{-1}$, whereas the borides give 46/49/58 $mV \cdot dec^{-1}$ (MoB_2/MoB / MoB_2-SP / MoB_2/B). At 100 $mA \cdot cm^{-2}$, the borides remain clustered at ~88–94 $mV \cdot dec^{-1}$, while Pt/C increases to 178 $mV \cdot dec^{-1}$; at 1 $A \cdot cm^{-2}$, the borides show ~460–544 $mV \cdot dec^{-1}$ vs ~1941 $mV \cdot dec^{-1}$ for Pt/C. These trends, summarized in **Figure 3.6b**, indicate that Pt/C becomes transport-limited under our stationary CC tests, whereas the borides sustain more favorable apparent kinetics at high current density.

Electrochemical impedance spectroscopy (EIS) was performed at overpotentials corresponding to 10 $mA \cdot cm^{-2}$ to compare the charge-transfer resistance (R_{ct}) of the electrodes, as summarized in **Table 3.5**. The Nyquist plots in **Figure 3.9** show a single semicircle for each sample, from which R_{ct} values were extracted: 24.4 Ω for MoB_2/MoB and 31.9 Ω for MoB_2-SP (both low), whereas MoB_2/B exhibits much higher Rct, consistent with its poorer performance. These resistances mirror the catalytic performances of each electrode and support that minimizing insulating B residues is critical for charge-transfer efficiency.

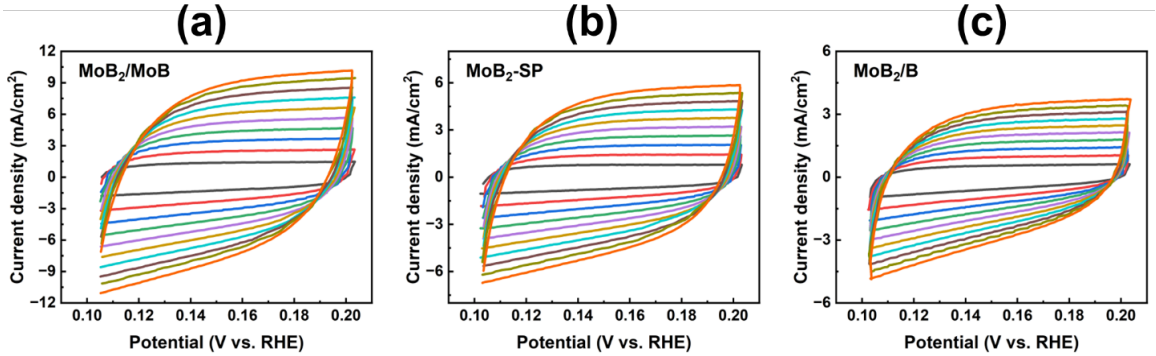

Figure 3.10. C_{dl} measurements from cyclic voltammetry profiles at different scan rates from 20 to 200 mV/s for (a) MoB_2/MoB, (b) MoB_2-SP, and (c) MoB_2/B.

The electrochemically active surface area (ECSA) was estimated via double-layer capacitance (C_{dl}). CVs used for extraction are plotted in **Figure 3.10**, and ECSA proxies are compiled in **Figure 3.6c** as Δj vs scan rate. MoB_2/MoB shows 38.7 $mF \cdot cm^{-2}$, MoB_2-SP 23.4 $mF \cdot cm^{-2}$ and MoB_2/B 13.4 $mF \cdot cm^{-2}$. Despite the lower ECSA and stronger agglomeration for MoB_2-SP, its overpotentials remain comparatively low across current regimes, highlighting intrinsic α-MoB_2 activity when excess-B residues are eliminated. **Figure 3.6e** along with **Figure 3.11** shows strong stability among the three electrodes, minimal change after 5000 CV cycles. The chronoamperometry of MoB_2/MoB shown in **Figure 3.6f** at around 300 $mA \cdot cm^{-2}$, remains stable for 24 hours, which is among the highest sustained current densities reported for boride nanoparticles under stationary testing.

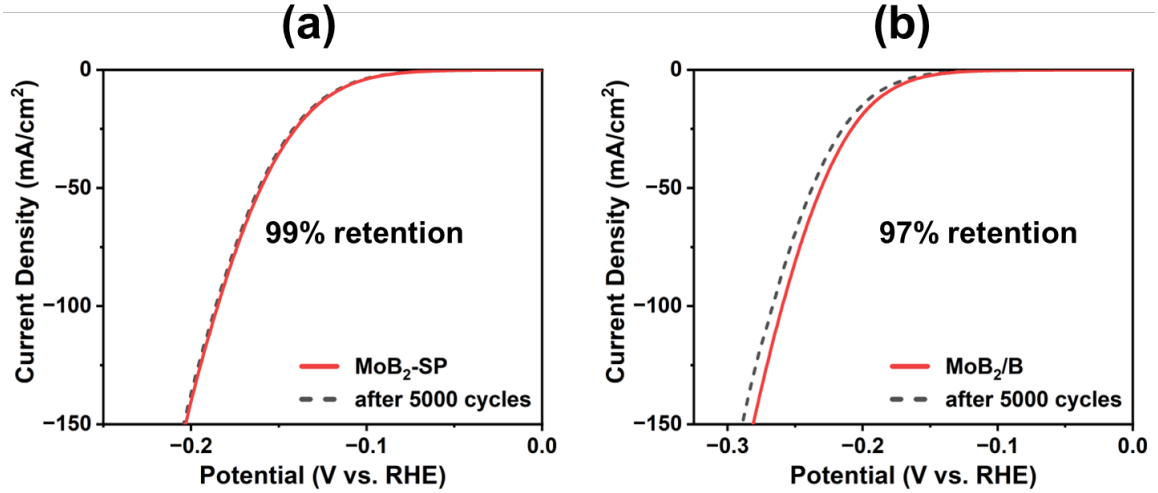

Figure 3.11. Polarization curves of (a) MoB_2-SP and (b) MoB_2/B electrodes before and after 5000 cycles.

3.4. Conclusion

We established a stoichiometric, flux-controlled synthesis of α-MoB_2 nanoparticles that avoids excess-boron artifacts and decouples size from phase: the boron feed tunes primary size/packing, and the Sn flux toggles phase/morphology between single-phase α-MoB_2 and MoB_2/MoB composites. Structural (XRD/HRTEM) and surface (XPS) analyses show that eliminating amorphous/oxidized B maximizes low-BE Mo–B and B^0 signatures, correlating with improved charge transfer (lower R_{ct}) and performance. Textural measurements (SEM, BET/QSDFT) reveal that higher Sn promotes coarsening and agglomeration with lower accessible area; nevertheless, α-MoB_2 (MoB_2-SP) remains highly active, demonstrating that intrinsic Mo-B terminations, not surface area alone, govern HER. Under stationary, non-rotating carbon cloth (CC)—a practical proxy for porous transport layers—α-MoB_2 achieves η_{150} = 203 mV and η_{1000} = 393 mV, while the MoB_2/MoB composite attains η_{150} = 173 mV and η_{1000} = 361 mV, outperforming Pt/C at 1 $A \cdot cm^{-2}$ under identical conditions. This performance stems from phase synergy (electronic percolation + site diversity), suppressed B-overcoats, and flux/boron-controlled growth that preserves conductive boride surfaces while limiting aggregation. Our two-knob design rule—B feed sets size/packing; Sn flux sets phase/morphology—offers a general blueprint to realize ampere-level, noble-metal-free HER on porous supports, and should translate to allied transition-metal borides.

3.5. References

1. Terlouw, T.; Rosa, L.; Bauer, C.; McKenna, R., Future hydrogen economies imply environmental trade-offs and a supply-demand mismatch., *Nat Commun*, **2024**, *15*, (1).
2. Roger, I.; Shipman, M. A.; Symes, M. D., Earth-abundant catalysts for electrochemical and photoelectrochemical water splitting., *Nat Rev Chem*, **2017**, *1*, 1–13.
3. Markovic, N. M.; Ross, P. N., Surface science studies of model fuel cell electrocatalysts., *Surf Sci Rep*, **2002**, *45*, (4–6), 117–229.
4. Chu, S.; Majumdar, A., Opportunities and challenges for a sustainable energy future., *Nature*, **2012**, *488*, (7411), 294–303.
5. Abbas, M. A.; Bang, J. H., Rising Again: Opportunities and Challenges for Platinum-Free Electrocatalysts., *Chemistry of Materials*, **2015**, *27*, (21), 7218–7235.
6. Hansen, J. N.; Prats, H.; Toudahl, K. K.; Mørch Secher, N.; Chan, K.; Kibsgaard, J.; Chorkendorff, I., Is There Anything Better than Pt for HER?, *ACS Energy Lett*, **2021**, *6*, (4), 1175–1180.
7. Shi, J.; Bao, Y.; Ye, R.; Zhong, J.; Zhou, L.; Zhao, Z.; Kang, W.; Aidarova, S. B., Recent progress and perspective of electrocatalysts for the hydrogen evolution reaction., *Catalysis Science and Technology*, **2025**, *15*, (7), 2104–2131.
8. Wu, H.; Feng, C.; Zhang, L.; Zhang, J.; Wilkinson, D. P., Non-noble Metal Electrocatalysts for the Hydrogen Evolution Reaction in Water Electrolysis., *Electrochemical Energy Reviews*, **2021**, *4*, (3), 473–507.
9. Laursen, A. B.; Kegnæs, S.; Dahl, S.; Chorkendorff, I., Molybdenum sulfides - Efficient and viable materials for electro - And photoelectrocatalytic hydrogen evolution., *Energy Environ Sci*, **2012**, *5*, (2), 5577–5591.
10. Popczun, E. J.; McKone, J. R.; Read, C. G.; Biacchi, A. J.; Wiltrout, A. M.; Lewis, N. S.; Schaak, R. E., Nanostructured nickel phosphide as an electrocatalyst for the hydrogen evolution reaction., *J Am Chem Soc*, **2013**, *135*, (25), 9267–9270.
11. Popczun, E. J.; Read, C. G.; Roske, C. W.; Lewis, N. S.; Schaak, R. E., Highly active electrocatalysis of the hydrogen evolution reaction by cobalt phosphide nanoparticles., *Angewandte Chemie - International Edition*, **2014**, *53*, (21), 5427–5430.
12. Liao, L.; Wang, S.; Xiao, J.; Bian, X.; Zhang, Y.; Scanlon, M. D.; Hu, X.; Tang, Y.; Liu, B.; Girault, H. H., A nanoporous molybdenum carbide nanowire as an electrocatalyst for hydrogen evolution reaction., *Energy Environ Sci*, **2014**, *7*, (1), 387–392.

13. Gong, Q.; Wang, Y.; Hu, Q.; Zhou, J.; Feng, R.; Duchesne, P. N.; Zhang, P.; Chen, F.; Han, N.; Li, Y.; Jin, C.; Li, Y.; Lee, S. T., Ultrasmall and phase-pure W2C nanoparticles for efficient electrocatalytic and photoelectrochemical hydrogen evolution., *Nat Commun*, **2016**, *7*.

14. Chen, Z.; Song, Y.; Cai, J.; Zheng, X.; Han, D.; Wu, Y.; Zang, Y.; Niu, S.; Liu, Y.; Zhu, J.; Liu, X.; Wang, G., Tailoring the d-Band Centers Enables Co 4 N Nanosheets To Be Highly Active for Hydrogen Evolution Catalysis ., *Angewandte Chemie*, **2018**, *130*, (18), 5170–5174.

15. Zhang, J.; Wang, T.; Liu, P.; Liao, Z.; Liu, S.; Zhuang, X.; Chen, M.; Zschech, E.; Feng, X., Efficient hydrogen production on MoNi 4 electrocatalysts with fast water dissociation kinetics., *Nat Commun*, **2017**, *8*, 15437.

16. Yu, P.; Wang, F.; Shifa, T. A.; Zhan, X.; Lou, X.; Xia, F.; He, J., Earth abundant materials beyond transition metal dichalcogenides: A focus on electrocatalyzing hydrogen evolution reaction., *Nano Energy*, **2019**, *58*, 244–276.

17. Song, A.; Song, S.; Duanmu, M.; Tian, H.; Liu, H.; Qin, X.; Shao, G.; Wang, G., Recent Progress of Non-Noble Metallic Heterostructures for the Electrocatalytic Hydrogen Evolution., *Small Science*, **2023**, *3*, (9).

18. Seh, Z. W.; Kibsgaard, J.; Dickens, C. F.; Chorkendorff, I.; Nørskov, J. K.; Jaramillo, T. F., Combining theory and experiment in electrocatalysis: Insights into materials design., *Science (1979)*, **2017**, *355*, (6321).

19. Zeng, K.; Zhang, D., Recent progress in alkaline water electrolysis for hydrogen production and applications., *Prog Energy Combust Sci*, **2010**, *36*, (3), 307–326.

20. T. F. Jaramillo; K. P. Jørgensen; J. Bonde; J. H. Nielsen; S. Horch; I. Chorkendorff, Identification of Active Edge Sites for Electrochemical H2 Evolution from MoS2 Nanocatalysts., *Science (1979)*, **2007**, *317*, (5834), 100–102.

21. Hinnemann, B.; Moses, P. G.; Bonde, J.; Jørgensen, K. P.; Nielsen, J. H.; Horch, S.; Chorkendorff, I.; Nørskov, J. K., Biomimetic hydrogen evolution: MoS2 nanoparticles as catalyst for hydrogen evolution., *J Am Chem Soc*, **2005**, *127*, (15), 5308–5309.

22. Feidenhans'l, A. A.; Regmi, Y. N.; Wei, C.; Xia, D.; Kibsgaard, J.; King, L. A., Precious Metal Free Hydrogen Evolution Catalyst Design and Application., *Chem Rev*, **2024**, *124*, (9), 5617–5667.

23. Zou, X.; Zhang, Y., Noble metal-free hydrogen evolution catalysts for water splitting., *Chem Soc Rev*, **2015**, *44*, (15), 5148–5180.

24. Sheng, W.; Myint, M.; Chen, J. G.; Yan, Y., Correlating the hydrogen evolution reaction activity in alkaline electrolytes with the hydrogen binding energy on monometallic surfaces., *Energy Environ Sci*, **2013**, *6*, (6), 1509–1512.

25. Carmo, M.; Fritz, D. L.; Mergel, J.; Stolten, D., A comprehensive review on PEM water electrolysis., *International Journal of Hydrogen Energy*, **2013**, *38*, (12), 4901–4934.

26. Lee, E.; Fokwa, B. P. T., Nonprecious Metal Borides: Emerging Electrocatalysts for Hydrogen Production., *Acc Chem Res*, **2022**, *55*, (1), 56–64.

27. Sadeghi, E.; Chamani, S.; Peighambardoust, N. S.; Aydemir, U., Unveiling the Potential of Metal Diborides for Electrocatalytic Water Splitting: A Comprehensive Review., *Energy and Environmental Materials*, **2025**, *8*, (3).

28. Abeysinghe, J. P.; Kölln, A. F.; Gillan, E. G., Rapid and Energetic Solid-State Metathesis Reactions for Iron, Cobalt, and Nickel Boride Formation and Their Investigation as Bifunctional Water Splitting Electrocatalysts., *ACS Materials Au*, **2022**, *2*, (4), 489–504.

29. Hong, J.; Mutalik, S.; Pescarmona, P. P.; Protesescu, L., Metal Borides: From Industrial Classics to Versatile Colloidal Nanocrystals for Energy, Catalysis, and Hard Coatings Applications†., *Chemistry of Materials*, **2024**, *36*, (5), 2147–2164.

30. Gupta, S.; Patel, N.; Miotello, A.; Kothari, D. C., Cobalt-Boride: An efficient and robust electrocatalyst for Hydrogen Evolution Reaction., *J Power Sources*, **2015**, *279*, 620–625.

31. Zeng, M.; Wang, H.; Zhao, C.; Wei, J.; Qi, K.; Wang, W.; Bai, X., Nanostructured Amorphous Nickel Boride for High-Efficiency Electrocatalytic Hydrogen Evolution over a Broad pH Range., *ChemCatChem*, **2016**, *8*, (4), 708–712.

32. Park, H.; Encinas, A.; Scheifers, J. P.; Zhang, Y.; Fokwa, B. P. T., Boron-Dependency of Molybdenum Boride Electrocatalysts for the Hydrogen Evolution Reaction., *Angewandte Chemie*, **2017**, *129*, (20), 5667–5670.

33. Rout, C. S.; Shinde, P. V.; Patra, A.; Jeong, S. M., Recent Developments and Future Perspectives of Molybdenum Borides and MBenes., *Advanced Science*, **2024**, *11*, (21).

34. Park, H.; Zhang, Y.; Scheifers, J. P.; Jothi, P. R.; Encinas, A.; Fokwa, B. P. T., Graphene-and Phosphorene-like Boron Layers with Contrasting Activities in Highly Active Mo2B4 for Hydrogen Evolution., *J Am Chem Soc*, **2017**, *139*, (37), 12915–12918.

35. Frotscher, M.; Klein, W.; Bauer, J.; Fang, C. M.; Halet, J. F.; Senyshyn, A.; Baehtz, C.; Albert, B., M2B5 or M2B4? A reinvestigation of the Mo/B and W/B system., *Z Anorg Allg Chem*, **2007**, *633*, (15), 2626–2630.

36. Park, H.; Zhang, Y.; Lee, E.; Shankhari, P.; Fokwa, B. P. T., High-Current-Density HER Electrocatalysts: Graphene-like Boron Layer and Tungsten as Key Ingredients in Metal Diborides., *ChemSusChem*, **2019**, *12*, (16), 3726–3731.

37. Park, H.; Lee, E.; Lei, M.; Joo, H.; Coh, S.; Fokwa, B. P. T., Canonic-Like HER Activity of Cr1–xMoxB2 Solid Solution: Overpowering Pt/C at High Current Density., *Advanced Materials*, **2020**, *32*, (28).

38. Huang, S.; Huang, A.; Huang, H.; Tan, C.; Yang, Y.; Tang, W.; Hao, L.; Xu, X.; Agathopoulos, S., Self-Supported α-MoB/β-MoB2 Ceramic Electrodes for Efficient High-Current-Density Hydrogen Evolution in Acidic, Neutral, and Alkaline pH-Values., *ACS Appl Mater Interfaces*, **2025**,.

39. Jothi, P. R.; Zhang, Y.; Scheifers, J. P.; Park, H.; Fokwa, B. P. T., Molybdenum diboride nanoparticles as a highly efficient electrocatalyst for the hydrogen evolution reaction., *Sustain Energy Fuels*, **2017**, *1*, (9), 1928–1934.

40. Fokwa, B. P. T.; Misse, P. R. N.; Gilleßen, M.; Dronskowski, R., Sn-flux syntheses, characterizations and bonding analyses of OsB and TiB2., *J Alloys Compd*, **2010**, *489*, (2), 339–342.

41. Portehault, D.; Devi, S.; Beaunier, P.; Gervais, C.; Giordano, C.; Sanchez, C.; Antonietti, M., A general solution route toward metal boride nanocrystals., *Angewandte Chemie - International Edition*, **2011**, *50*, (14), 3262–3265.

42. Liu, X.; Gong, Y., α-MoB2Nanosheets for Hydrogen Evolution in Alkaline and Acidic Media., *ACS Appl Nano Mater*, **2022**, *5*, (8), 10183–10191.

43. Jothi, P. R.; Yubuta, K.; Fokwa, B. P. T., A Simple, General Synthetic Route toward Nanoscale Transition Metal Borides., *Adv Mater*, **2018**, *30*, (14), 2–7.

44. Jothi, P. R.; Zhang, Y.; Yubuta, K.; Culver, D. B.; Conley, M.; Fokwa, B. P. T., Abundant vanadium diboride with graphene-like boron layers for hydrogen evolution., *ACS Appl Energy Mater*, **2019**, *2*, (1), 176–181.

45. Kim, S. B.; Yapo, J. A.; Yasuhara, A.; Yubuta, K.; Fokwa, B. P. T., Vanadium-Stabilized MoB Nanoparticles Enable Hydrogen Evolution at Industry-Relevant High Current Densities., *Small*, **2025**,.

46. Liu, X.; Gong, Y., A Simple Molten Salt Route to Crystalline β-MoB2Nanosheets with High Activity for the Hydrogen Evolution Reaction., *Inorg Chem*, **2021**, *60*, (23), 18075–18081.

47. Jin, M.; Zhang, X.; Niu, S.; Wang, Q.; Huang, R.; Ling, R.; Huang, J.; Shi, R.; Amini, A.; Cheng, C., Strategies for Designing High-Performance Hydrogen Evolution Reaction Electrocatalysts at Large Current Densities above 1000 mA cm-2., *ACS Nano*, **2022**, *16*, (8), 11577–11597.

48. Wang, C. R. et al., Proton Exchange Membrane (PEM) Water Electrolysis: Cell-Level Considerations for Gigawatt-Scale Deployment., *Chemical Reviews*, **2025**, *125*, (3), 1257–1302.

49. Suntivich, J.; Gasteiger, H. A.; Yabuuchi, N.; Shao-Horn, Y., Electrocatalytic Measurement Methodology of Oxide Catalysts Using a Thin-Film Rotating Disk Electrode., *J Electrochem Soc*, **2010**, *157*, (8), B1263.

50. Ehelebe, K.; Schmitt, N.; Sievers, G.; Jensen, A. W.; Hrnjić, A.; Collantes Jiménez, P.; Kaiser, P.; Geuß, M.; Ku, Y. P.; Jovanovič, P.; Mayrhofer, K. J. J.; Etzold, B.; Hodnik, N.; Escudero-Escribano, M.; Arenz, M.; Cherevko, S., Benchmarking Fuel Cell Electrocatalysts Using Gas Diffusion Electrodes: Inter-lab Comparison and Best Practices., *ACS Energy Lett*, **2022**, *7*, (2), 816–826.

51. Satjaritanun, P.; Shimpalee, S.; Zenyuk, I. V., Gas Diffusion Layers: Experimental and Modeling Approach for Morphological and Transport Properties., *Acc Mater Res*, **2022**, *3*, (4), 416–425.

52. Yuan, S.; Zhao, C.; Cai, X.; An, L.; Shen, S.; Yan, X.; Zhang, J., Bubble evolution and transport in PEM water electrolysis: Mechanism, impact, and management., *Progress in Energy and Combustion Science*, **2023**, *96*.

53. Tao, Y.; Wu, M.; Hu, M.; Xu, X.; Abdullah, M. I.; Shao, J.; Wang, H., High-performance porous transport layers for proton exchange membrane water electrolyzers., *SusMat*, **2024**, *4*, (4).

54. Lagadec, M. F.; Grimaud, A., Water electrolysers with closed and open electrochemical systems., *Nature Materials*, **2020**, *19*, (11), 1140–1150.

55. Hensle, N.; Hoffmann, J.; Najafianashrafi, Z.; Smolinka, T.; Abel Chuang, P. Y.; Weber, A., Understanding the use of carbon-based porous transport layers at the cathode in PEM water electrolysis., *J Power Sources*, **2025**, *642*.

56. Cho, J.; Kim, D. H.; Noh, M. W.; Kim, H.; Oh, H. G.; Lee, P.; Yoon, S.; Won, W.; Park, Y. J.; Lee, U.; Choi, C. H., Dissolution of the Ti porous transport layer in proton exchange membrane water electrolyzers., *J Mater Chem A Mater*, **2024**, *12*, (35), 23688–23696.

57. Zhang, T.; Meng, L.; Chen, C.; Du, L.; Wang, N.; Xing, L.; Tang, C.; Hu, J.; Ye, S., Similarities and Differences between Gas Diffusion Layers Used in Proton Exchange Membrane Fuel Cell and Water Electrolysis for Material and Mass Transport., *Advanced Science*, **2024**, *11*, (32).

58. Bhandari, S.; Narangoda, P. V.; Mogensen, S. O.; Tesch, M. F.; Mechler, A. K., Effect of Experimental Parameters on the Electrocatalytic Performance in Rotating Disc Electrode Measurements: Case Study of Oxygen Evolution on Ni−Co-Oxide in Alkaline Media., *ChemElectroChem*, **2022**, *9*, (17).

59. McCrory, C. C. L.; Jung, S.; Ferrer, I. M.; Chatman, S. M.; Peters, J. C.; Jaramillo, T. F., Benchmarking Hydrogen Evolving Reaction and Oxygen Evolving Reaction Electrocatalysts for Solar Water Splitting Devices., *J Am Chem Soc*, **2015**, *137*, (13), 4347–4357.

60. Park, S. H.; Koo, J.; Park, Y. J.; Jang, S.; Ryu, H. J.; Han, H. S.; Lee, K. T., Uniformly scalable and stackable porous transport layer manufactured by tape casting and calendering for efficient water electrolysis., *Chemical Engineering Journal*, **2024**, *481*.

61. Shi, Y.; Yang, F.; Tao, L., Ni-Activated and Ni-P-Activated Porous Titanium Carbide Ceramic Electrodes as Efficient Electrocatalysts for Overall Water Splitting., *ACS Appl Mater Interfaces*, **2023**, *15*, (23), 28055–28063.

62. Wei, Y.; Huang, Z.; Zhou, L.; Ran, S., Novel borothermal synthesis of VB2 powders., *International Journal of Materials Research*, **2015**, *106*, (11), 1206–1208.

63. Lee, E.; Yapo, J. A.; Bhupathy, A.; Mentzel, T. S.; Yin, X.; Adeniji, S. E.; Kim, S. B.; Fokwa, B. P. T., Antibonding–Vacancy Coupling Boosts Hydrogen Evolution Rate in Diborides., *ACS Energy Lett*, **2025**, 4560–4566.

Chapter 4.

Redox-Flux-Assisted Iodide Chemistry Yields Nanosized RuB_2/Ru_2B_3 Composites for Hydrogen Evolution in Acidic and Alkaline Media: Managing Iodide Volatility

Sang Bum Kim, Logan Quach, Boniface P.T. Fokwa

Ruthenium borides are promising, Pt-like hydrogen evolution reaction (HER) catalysts, but nanosizing and phase control remain challenging due to volatile halide transport and high-temperature growth. We report a halide-directed, flux-assisted route that uses RuI_3 with KCl (≈50 wt%) to suppress iodide volatility and enable nanoparticulate, boron-rich Ru–B composites. Compared head-to-head with a conventional $RuCl_3$/Sn route, the iodide path yields finer particles and a RuB_2/Ru_2B_3 composite (I-RuB_2/Ru_2B_3) with superior HER activity: in 0.5 M H_2SO_4 it requires 13.0 mV and 101.7 mV to achieve 10 and 150 mA cm^{-2}, respectively; in 1.0 M KOH, 15.6 mV and 122 mV. A chloride-derived analog (Cl-RuB_2/Ru_2B_3) is competitive but coarser, while excess-boron synthesis (Cl-RuB_2/B) shows low overpotentials at 10 mA cm^{-2} yet suffers high-current losses attributed to resistive B-rich overlayers. Tafel slopes for the composites fall below 30 mV dec^{-1}, consistent with Pt-like kinetics. Although acid stability is limited, the best catalyst retains ~97% activity after 5000 cycles in alkaline electrolyte. This iodide-enabled strategy generalizes molten-salt moderation of volatile precursors and clarifies activity–stability trade-offs that govern Ru–B HER catalysts across various pH values.

4.1. Introduction

Hydrogen is widely promoted as a clean energy carrier that can help decarbonize hard-to-electrify sectors when produced using low-carbon pathways.[1] In prospective "hydrogen economy" scenarios, electrolytic H_2 can cut lifecycle emissions versus fossil-derived H_2 by ~50–90% depending on the power mix and scale.[2] Yet deployment faces systems-level constraints (renewable build-out, land/water footprints, infrastructure), reinforcing the need for efficient, durable electrocatalysts that reduce stack cost and energy use.[3–5] Water electrolysis offers high-purity H_2 and grid-balancing potential—including with non-ideal waters—but its viability hinges on catalyst performance and stability across media.[6,7] At the active-site level, Pt remains the benchmark for HER due to near-optimal ΔG_{H^*}, but its scarcity and price motivate alternatives with comparable activity and far better material availability.[8–11]

HER proceeds via Volmer–Heyrovsky or Volmer–Tafel sequences; acidic HER draws protons from hydronium, whereas alkaline HER must first split water, generally slowing kinetics.[12–15] This pH-dependence explains why exchange currents for Pt-group surfaces can drop by orders of magnitude in base relative to acid, and why interfacial cations/water structure modulate reaction barriers.[14,15] Mechanistic insight into ΔG_{H^*}, water dissociation energetics, and the electric double layer therefore guides catalyst design that remains active across electrolytes. [16]

Transition-metal borides (TMBs) have emerged as promising HER catalysts because strong metal–boron bonding and diverse structures can confer high conductivity, corrosion resistance, and intrinsically active surfaces—even without extreme

nanosizing.[17–20] In AlB_2-type diborides with graphenic B–B layers, boron motifs themselves contribute to favorable hydrogen adsorption and charge transfer, creating bifunctional metal–boron ensembles.[21] Specific examples include α-MoB_2 and W-promoted α-$Mo_{1-x}W_xB_2$ that sustain high HER rates at elevated current density, consistent with activity of flat B-layers and W-enabled electronic promotion.[21,22] Low-temperature redox/metathesis routes have also delivered nanocrystalline MoB_2 with improved activity over bulk material by exposing these favorable facets, and more recently V-stabilized MoB solid solutions ($V_{0.3}Mo_{0.7}B$) reached industrial-level current densities while retaining durability.[23,24]

Ruthenium-based catalysts are especially attractive because Ru binds hydrogen similarly to Pt yet is more abundant, and its activity can be boosted via local coordination and support effects.[25–27] Embedding single Ru atoms or ultrasmall Ru ensembles in N-doped carbons yields pH-universal HER performance and, in alkaline media, even surpasses commercial Pt/C through lower water-dissociation barriers at RuC_xN_y moieties.[25,28] Within the Ru–B family, phase engineering matters: comparative studies on Ru_7B_3, RuB, Ru_2B_3 and RuB_2 show that increasing boron content (toward RuB_2) weakens over-strong Ru–H binding and enhances activity/stability.[29] Complementary Ru–B on heteroatom-doped carbons has likewise delivered low overpotentials in both acid and base via synergistic Ru–B interactions that facilitate Volmer kinetics.[30]

A persistent challenge for Ru systems is durability in strongly acidic environments, where oxidation/dissolution pathways can degrade Ru under aggressive operation.[31] Strategies to mitigate degradation include (i) strong metal–support interactions and

coordination that anchor isolated Ru centers, which maintain activity with improved acid stability; (ii) electronic/structural tuning via heterointerfaces that modulate water activation; and (iii) electrolyte micro-environment engineering, where alkali cations restructure interfacial water and influence HER/HOR kinetics.[25,26,28,30] While cation-engineering alone is not a universal "anti-corrosion" fix, it complements catalyst design by lowering kinetic penalties for water dissociation and shaping the double layer.[15]

Scaling TMBs to the nanoscale increases active area and exposes specific boron-rich planes, but conventional high-temperature syntheses often yield coarse grains and mixed phases.[17,19,32] Solution or molten-salt redox/metathesis strategies address this by lowering temperatures, enabling particle-size/morphology control and access to metastable or highly dispersed borides.[23,33,34] Chemical reduction with borohydrides can also produce amorphous or nanocrystalline borides that are HER-active across pH, offering a complementary route to crystalline intermetallics.[35,36]

Precursor chemistry is a critical but underused lever in controlling TMB nucleation/growth. In particular, trace halides strongly perturb reduction kinetics and particle morphology; iodide is especially potent, accelerating some metal reductions while retarding others and driving rapid, shape-selective growth.[37,38] Specific adsorption of iodide can steer anisotropic growth and facet expression, often causing burst nucleation and fast particle coalescence; in multimetal co-reductions, iodide can differentially control relative reduction rates and complicate phase-pure co-nucleation.[38–40] These attributes help explain why metal iodides are rarely used as primary precursors for controlled boride nanoparticles syntheses, despite their strong kinetic leverage.

Here, we introduce a halide-directed, flux-assisted synthesis that pairs an iodide route—RuI_3 moderated by KCl (≈50 wt%)—with a conventional chloride/Sn route ($RuCl_3$ + Sn) to disentangle how precursor identity governs phase selection, particle size, and HER performance across pH. KCl suppresses iodide-driven volatility and enables nanosized, boron-rich Ru–B, yielding a RuB_2/Ru_2B_3 composite (I-RuB_2/Ru_2B_3), whereas the chloride/Sn path furnishes a similar composite but with coarser grains (Cl-RuB_2/Ru_2B_3); pushing chloride to excess boron produces near-single-phase RuB_2 enveloped by a B-rich overlayer (Cl-RuB_2/B). The iodide-derived composite delivers low overpotentials of 13.0/101.7 mV (10/150 mA cm^{-2}) in 0.5 M H_2SO_4 and 15.6/122 mV in 1.0 M KOH, along with Pt-like Tafel slopes (<30 mV dec^{-1}), while the B-overlayer sample exhibits pronounced high-current losses. Durability diverges by pH: despite limited acid stability typical of Ru systems, I-RuB_2/Ru_2B_3 retains ~97% of its initial activity after 5,000 cycles in alkaline electrolyte without any added conductive support. Collectively, we map practical synthesis windows for boron-rich Ru–B, establish an iodide/KCl precursor–flux pairing that enables true nanosizing, and clarify activity–stability trade-offs at technologically relevant current densities.

4.2. Experimental Section

4.2.1. Chemicals

Ruthenium Chloride ($RuCl_3$, powder, 99.9%), Ruthenium Iodide (RuI_3, powder, ≥ 99%), boron (amorphous powder, 99%) and Platinum on carbon (Pt/C, 20%) were obtained from Alfa Aesar. Sulfuric acid (H_2SO_4, 98%) was purchased from Fisher

Scientific. Copper sheet and conductive carbon glue were obtained from Basic Copper and Ted Pella, respectively. All chemicals were used without further purification.

4.2.2. Sample preparation

All of the chemicals used in the experiment were handled in a nitrogen-filled glovebox. Anhydrous ruthenium sources, $RuCl_3$ and RuI_3, elemental boron, and Sn powder were mixed in a mortar and pressed into a pellet in the glovebox. The pellet was then sealed in a quartz ampoule under vacuum after argon atmosphere. Different mole compositions (Ru source : B : Sn or KCl) were used for different samples. The sealed quartz ampoule containing the pellet was then heated in an electric furnace for 4 hours at 850 °C with 2 °C/min (for $RuCl_3$ samples) and 0.5 °C/min (for RuI_3 samples) heating and cooling rates. Upon completion of the reaction, the ampoule was opened to reveal a dark-colored product (powder), which was then ground further into finer powder and treated in approximately 10% HCl for one hour before being washed with deionized water and ethanol, then dried overnight at 65 °C.

4.2.3. Electrode preparation

4 mg of each synthesized powder was ultrasonically dispersed in 1 mL of ethanol with 20 μL of a 5% Nafion solution (Sigma Aldrich) for 30 min to form a homogeneous catalyst slurry. Then the slurry catalyst mixture was coated onto a carbon cloth (Sigracet) with an area of 3×3 mm^2. Finally, the catalyst-coated carbon cloth was placed in a drying oven at 70 °C for 120 minutes to remove the solvent from the electrode and to improve adhesion. Then the catalyst-coated carbon cloth was attached to a copper sheet using conductive silver paste. The exposed surface of the copper sheet was covered with epoxy

adhesive and dried overnight at room temperature. The catalyst loading of the electrode was kept at ~1 mg/cm^2 for all the samples analyzed.

4.3. Results and Discussion

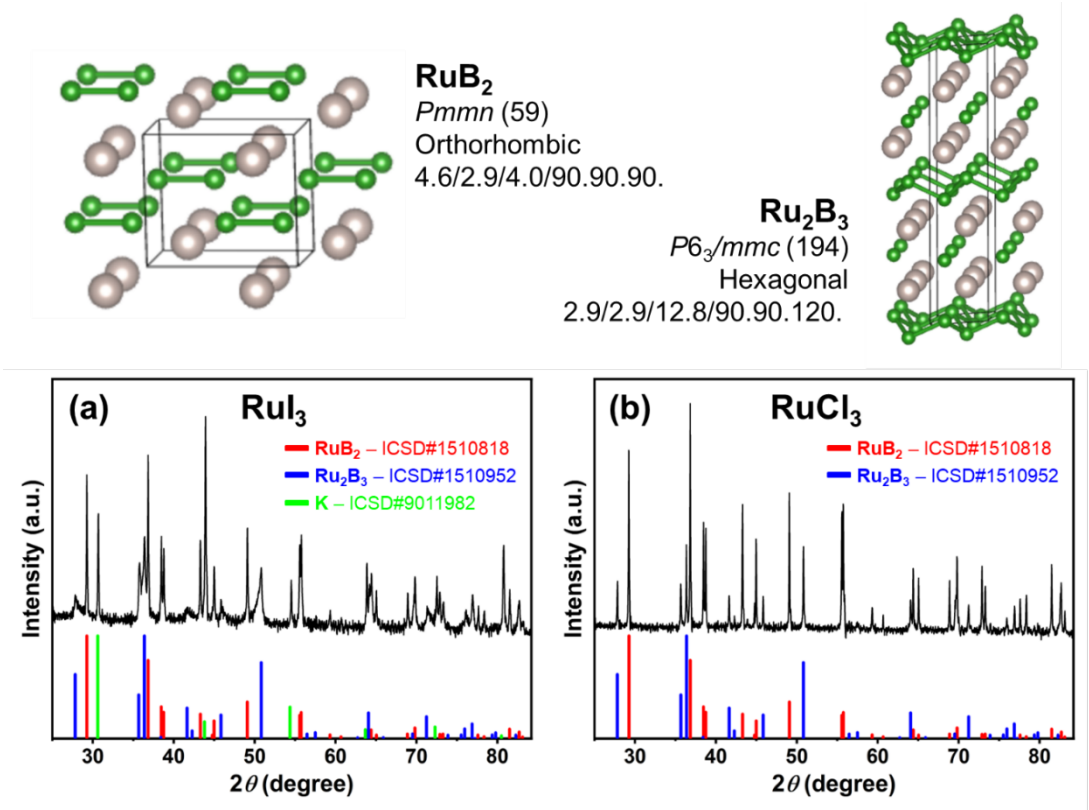

Figure 4.1. Powder X-ray diffraction (PXRD) of ruthenium boride products prepared by halide-directed, flux-assisted synthesis. (a) I-RuB_2/Ru_2B_3 and (b) Cl-RuB_2/Ru_2B_3

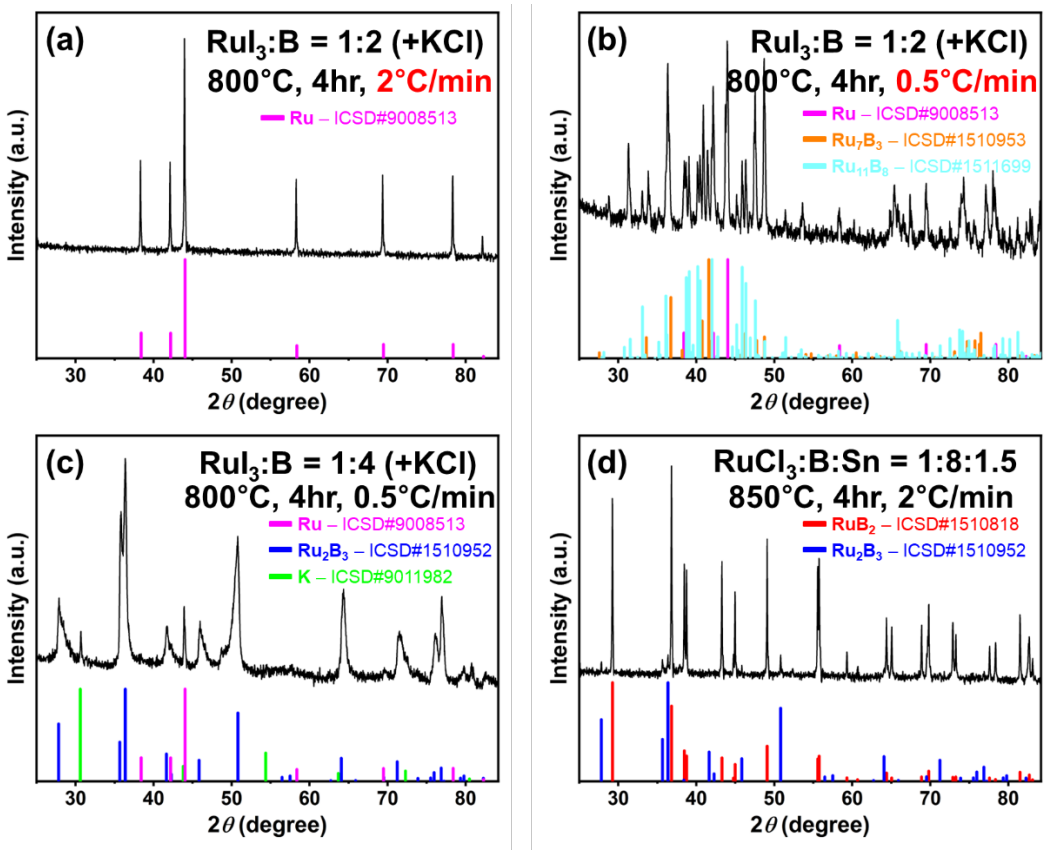

Figure 4.2. Powder X-ray diffraction data of synthesized products of different Ru:B ratio with KCl or Sn at different reaction temperatures and heating rates. (a) 1:2+KCl at 800 °C with 2 °C/min, (b) 1:2+KCl at 800 °C with 0.5 °C/min, (c) 1:4+KCl at 800 °C with 0.5 °C/min, and (d) (Cl-RuB_2/B) 1:8+Sn at 850 °C with 2°C/min.

Powder X-ray diffraction (PXRD) in **Figure 4.1a** and **b** benchmarks two representative composites obtained from iodide and chloride metal sources, respectively: an iodide-derived RuB_2/Ru_2B_3 composite prepared with RuI_3 + KCl flux (I-RuB_2/Ru_2B_3) and a chloride-derived analogue from $RuCl_3$ + Sn (Cl RuB_2/Ru_2B_3). Systematic control experiments in **Figure 4.2a–d** map the synthesis window. Using RuI_3 alone, rapid ramps in reaction temperature transport volatile Ru/I/Sn species to be condensed on top of the ampoule headspace so the pellet disintegrates and the reaction between Ru and B does not take place. However, adding solid KCl (~50 wt%) suppresses iodide volatility (metathesis

to KI) and acts as a molten-salt flux above ~770 °C,[41] allowing reaction to proceed to 850 °C where Ru–B coupling occurs (**Figure 4.2a–c**). Heating-rate sensitivity is pronounced: the fast ramp (**Figure 4.2a**) prematurely reduces to Ru^0 to form metal ruthenium crystals, whereas the slower ramp (**Figure 4.2b**) yields Ru-rich borides. Increasing B to a 1:4 (metal:B) in the feed (**Figure 4.2c**) stabilizes Ru_2B_3 at 800 °C, and stepping to 850 °C furnishes the I-RuB_2/Ru_2B_3 composite summarized in **Figure 4.1a**. Residual K is partially trapped and not fully removed by washing, consistent with weak K-bearing signatures in the PXRD pattern (**Figure 4.1a**) and EDS mapping (**Figure 4.5**). Cl-RuB_2/Ru_2B_3 in **Figure 4.1b** was synthesized with the exact same conditions as the iodide counterpart, except for its metal source and the redox/flux agent (Sn).[33] Using Sn, which can be easily removed with acid and does not form a secondary phase with either Ru or B, no side phases other than the two main Ru-B crystals are evident as seen in XRD pattern. Pushing the chloride route to 1:8 (metal:B) drives the product toward RuB_2 with a B-rich matrix (Cl-RuB_2/B) as in **Figure 4.2d**. Notably, with $RuCl_3$ + Sn the reaction pellet loses its initial shape and disintegrates into coarse powder, yielding bulkier product even when the phase assemblage converges to RuB_2/Ru_2B_3 after the reaction. These outcomes mirror prior MoB_2 synthesis in Chapter 3 of this thesis: excess B promotes diboride purity while encouraging B-derived surface layers and smaller crystallites.

Table 4.1. Composition of the three samples measured from EDS (Fig 2 & Fig S2,S3).

Sample	Ru (at%)	B (at%)	B/Ru Ratio
RuI_3 - 1:4	24.3	75.7	3.12
$RuCl_3$ - 1:4	23.7	76.3	3.22
$RuCl_3$ - 1:8	11.6	88.4	7.62

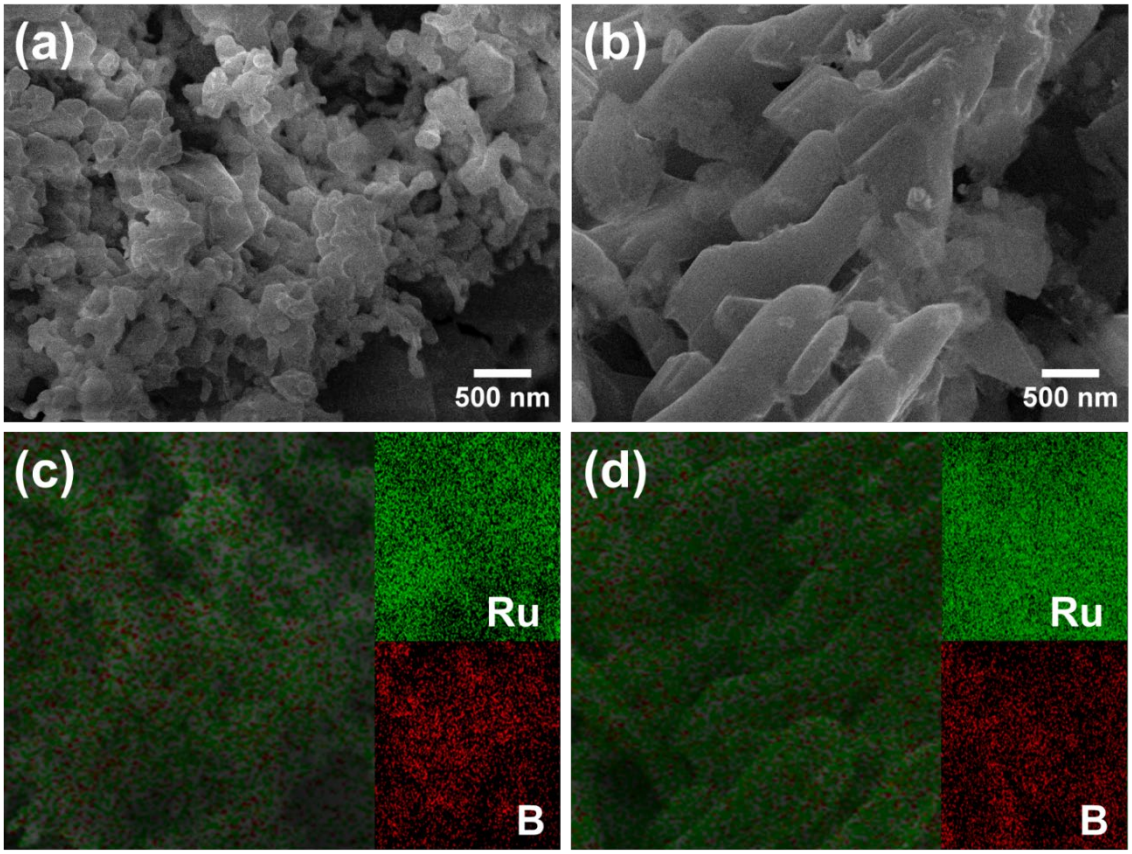

Figure 4.3. SEM images of (a) I-RuB_2/Ru_2B_3 and (b) Cl-RuB_2/Ru_2B_3, and the energy dispersive X-ray spectroscopy (EDS) elemental mapping of Ru and B in (c) I-RuB_2/Ru_2B_3 and (d) Cl-RuB_2/Ru_2B_3

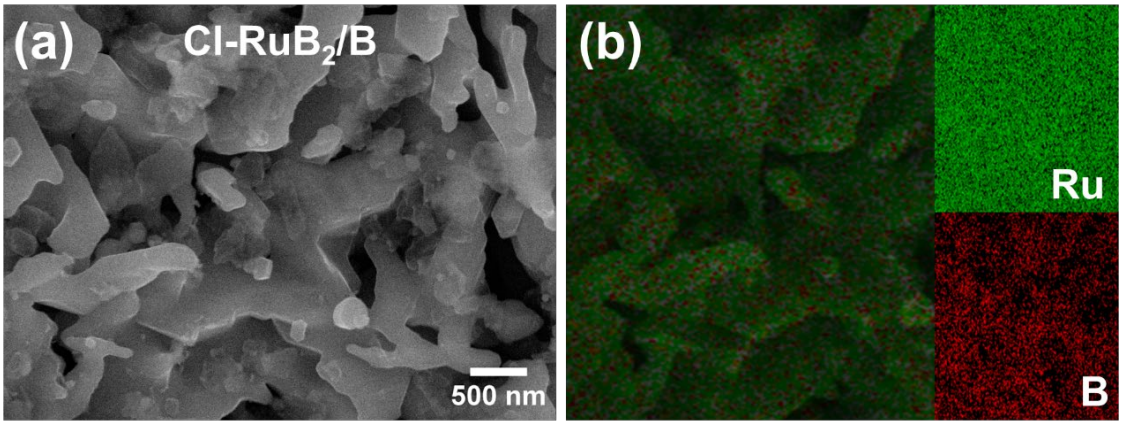

Figure 4.4. (a) SEM image and (b) energy dispersive X-ray spectroscopy (EDS) elemental mapping of Ru and B of Cl-RuB_2/B.

Morphology and spatial elemental distributions corroborate these trends. SEM in **Figure 4.3a** shows the iodide route produces much finer primaries in nanoscale, while the chloride/Sn product in **Figure 4.3b** comprises loosely sintered, coarser aggregates. EDS maps for Ru and B (uniform lateral distributions) are shown for the iodide composite in **Figure 4.3c** and the chloride composites in **Figure 4.3d** and **Fig S2b**. The Cl-RuB_2/B specimen is provided in **Figure 4.4**. Quantitative EDS (spectra in **Figure 4.6**) and the summary **Table 4.1** give metal (Ru) vs. B atomic percentages of 24.3:75.7 for I-RuB_2/Ru_2B_3 (1:4 feed), 23.7:76.3 for Cl-RuB_2/Ru_2B_3 (1:4), and 11.6:88.4 for Cl-RuB_2/B (1:8), corresponding to B/metal ratios of ~3.1, ~3.2, and ~7.6, respectively. These results are consistent with mixed Cl-RuB_2/Ru_2B_3 domains plus B-rich surfaces in the composites and a strongly B-enriched surface matrix enveloping RuB_2 grains in the 1:8 product as parallel to previously reported borides.[24,33] The SEM image of Cl-RuB_2/B in **Figure 4.4a** is composed of smaller particles with similar morphology to Cl-RuB_2/Ru_2B_3 with less B in the feed. This is consistent with previous reports and Ch.3 of this thesis, that the excess boron in the feed decreases the size of resulting particles.[24,34]

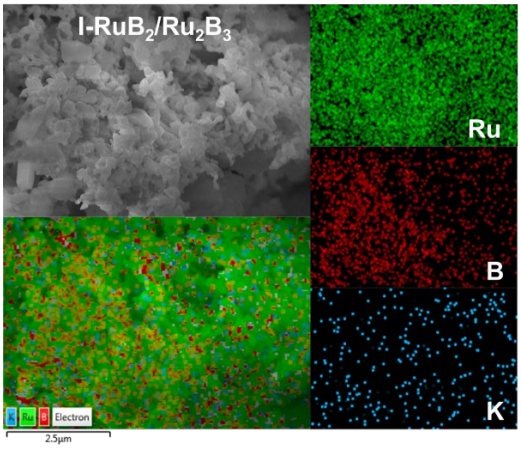

Figure 4.5. EDS mapping of I-RuB_2/Ru_2B_3 (Ru, B, and K) in (a) wide and (b) close-up views.

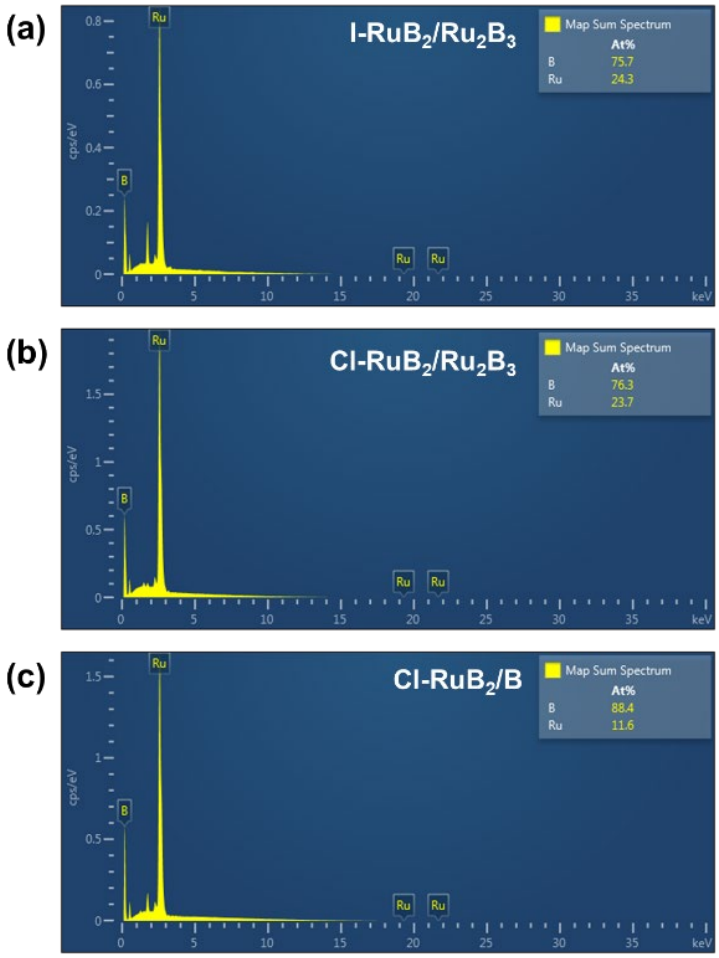

Figure 4.6. EDS elemental spectra of (a) I-RuB_2/Ru_2B_3, (b) Cl-RuB_2/Ru_2B_3, and (c) Cl-RuB_2/B for Ru & B from the mapping in **Figure 4.3** and **4.4**.

Hydrogen evolution reaction (HER) activity follows these structure–composition motifs. Polarization curves (iR-corrected LSVs) in **Figure 4.7a** (0.5 M H_2SO_4) and **Figure 4.7b** (1.0 M KOH) show that I-RuB_2/Ru_2B_3 reaches 10/150 mA cm^{-2} at overpotentials of 13.0/101.7 mV in the acid and 15.6/122 mV in the alkaline medium. Cl-RuB_2/Ru_2B_3 requires 28.7/163.7 mV (acid) and 21.8/149.2 mV (alkaline), whereas Cl-RuB_2/B exhibits 16.4/245.5 mV (acid) and 24.6/201.5 mV (alkaline). The electrodes require generally lower overpotentials for a given current density in H_2SO_4 than KOH as consistent with previous

reports on Ru-B based catalysts.[29,42] B-rich surface matrices in Cl-RuB_2/B show comparable overpotential at lower current density (η_{10}) but penalized at high current density (η_{150}), consistent with resistive B overlayers as expected,[24,34] aligning with the Chapter 3 result in this dissertation. In base, the gap between the two benchmark composites narrows, Cl-RuB_2/Ru_2B_3 particularly competitive, yet I-RuB_2/Ru_2B_3 still shows equal or better performance than the benchmark Pt/C.

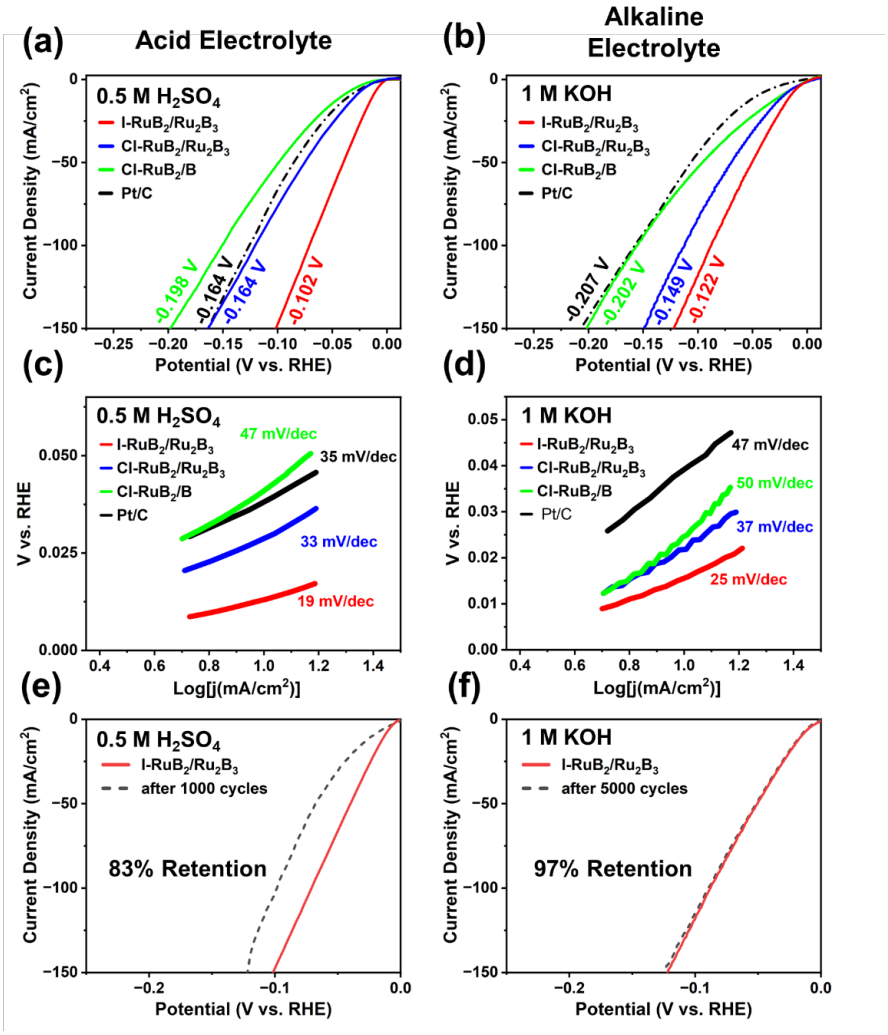

Figure 4.7. Linear sweep polarization curves of I-RuB_2/Ru_2B_3, Cl-RuB_2/Ru_2B_3, Cl-RuB_2/B, and 20% Pt/C electrodes (a) in 0.5 M H_2SO_4 and (b) 1 M KOH. Tafel slopes of these materials (c) in 0.5 M H_2SO_4 and (d) 1 M KOH. Polarization curves of I-RuB_2/Ru_2B_3 electrode before and after 5000 cycles (e) in 0.5 M H_2SO_4 and (f) 1 M KOH

Kinetic analysis via Tafel plots (**Figure 4.7c,d**) reveals Pt-like behavior for the composites, with slopes less than 30 mV dec^{-1} and the iodide composite (I-RuB_2/Ru_2B_3) even dipping further below 30 mV dec^{-1} in both media. Such values are characteristic of a Volmer–Tafel mechanism with Tafel recombination as the rate-determining step on optimized, Pt-like surfaces; by contrast, the B-rich Cl-RuB_2/B exhibits larger slopes, consistent with additional kinetic resistance and/or less ideal H* binding imposed by surface films. These observations are consistent with canonical HER microkinetics, which assign ~30 mV dec^{-1} to the Tafel-limited pathway and ~40/120 mV dec^{-1} to Heyrovsky/Volmer limits, respectively.

Durability diverges sharply by pH (**Figure 4.7e,f**). In acid, all Ru–B electrodes show noticeable decay on cycling, consistent with known dissolution/ripening pathways of Ru-containing nanoparticles under strongly acidic polarization. In alkaline, the I-RuB_2/Ru_2B_3 electrode retains ~97% of its initial activity after 5,000 cycles, pointing to stable surfaces/microstructures under OH^- media and highlighting the benefit of the nanoscale composite architecture. Literature suggests several levers to further harden Ru-based catalysts without sacrificing activity: engineering the interfacial cation environment (e.g., K^+) to restructure water and lower kinetic barriers; building strong metal–support interactions and heterointerfaces to pin Ru centers; and tuning local coordination with B/N-doped carbons.[16,43–47] While these strategies have been demonstrated broadly for HER/HOR and for stabilizing Ru oxides in harsh media, they are directly compatible with the present Ru–B platform (and practically implementable here, given residual K observed by EDS).

4.4. Conclusion

This study establishes a practical synthesis window to access highly active Ru–B catalysts by leveraging iodide chemistry under flux control. Using RuI_3 with KCl (≈50 wt%) mitigates iodide-driven vapor transport and enables nucleation/growth of B-rich Ru–B phases at 800–850 °C. Compared with the conventional $RuCl_3$/Sn route, the iodide/KCl strategy produces markedly smaller particles and a RuB_2/Ru_2B_3 composite (I-RuB_2/Ru_2B_3) that exhibits Pt-like kinetics (Tafel slopes ≤ 30 mV dec^{-1}) and low overpotentials at both modest and industrially relevant currents. Specifically, I-RuB_2/Ru_2B_3 achieves 13.0 mV (10 mA cm^{-2}) and 101.7 mV (150 mA cm^{-2}) in acid, and 15.6 mV and 122 mV in base, outperforming the chloride-derived composite (28.7/163.7 mV in acid; 21.8/149.2 mV in base at 10/150 mA cm^{-2}). An excess-boron chloride route drives near-single-phase RuB_2 (Cl-RuB_2/B) with low 10 mA cm^{-2} overpotentials but pronounced high-current losses, consistent with a resistive B-rich surface matrix that hampers charge transport.

While acid cycling reveals durability limitations typical of Ru/RuO_x systems, alkaline stability is excellent: ~97% retention after 5000 cycles, underscoring the inherent resilience of the iodide-derived composite in OH^- media. Literature strategies—including cation-environment engineering (e.g., K^+), interfacial water structuring, and strong metal–support interactions—offer clear routes to extend acid durability and further improve kinetics in base without compromising activity. Together with the size/phase control afforded by iodide plus KCl, these approaches provide a coherent roadmap for optimizing Ru–B catalysts across pH.

Beyond Ru–B, this work highlights precursor/halide identity as a powerful lever for TMB synthesis. Iodide's unique reduction/adsorption behavior, when moderated by a molten-salt flux, can deliver nanoscale products and stabilize B-rich intermetallics otherwise difficult to access, while avoiding complete volatilization at elevated temperatures. This synthesis–structure–function framework should translate to other borides where balancing phase purity, particle size, and conductive surfaces is essential for achieving low overpotentials at high current densities.

4.5. References

1. Turner, J. A., Sustainable Hydrogen Production., *Science (1979)*, **2004**, *305*, (5686), 972–974.
2. Terlouw, T.; Rosa, L.; Bauer, C.; McKenna, R., Future hydrogen economies imply environmental trade-offs and a supply-demand mismatch., *Nat Commun*, **2024**, *15*, (1).
3. van Renssen, S., The hydrogen solution?, *Nature Climate Change*, **2020**, *10*, (9), 799–801.
4. Li, Y.; Zhou, H.; Cai, S.; Prabhakaran, D.; Niu, W.; Large, A.; Held, G.; Taylor, R. A.; Wu, X. P.; Tsang, S. C. E., Electrolyte-assisted polarization leading to enhanced charge separation and solar-to-hydrogen conversion efficiency of seawater splitting., *Nat Catal*, **2024**, *7*, (1), 77–88.
5. Tonelli, D.; Rosa, L.; Gabrielli, P.; Caldeira, K.; Parente, A.; Contino, F., Global land and water limits to electrolytic hydrogen production using wind and solar resources., *Nat Commun*, **2023**, *14*, (1).
6. Tong, W.; Forster, M.; Dionigi, F.; Dresp, S.; Sadeghi Erami, R.; Strasser, P.; Cowan, A. J.; Farràs, P., Electrolysis of low-grade and saline surface water., *Nature Energy*, **2020**, *5*, (5), 367–377.
7. van der Spek, M.; Banet, C.; Bauer, C.; Gabrielli, P.; Goldthorpe, W.; Mazzotti, M.; Munkejord, S. T.; Røkke, N. A.; Shah, N.; Sunny, N.; Sutter, D.; Trusler, J. M.; Gazzani, M., Perspective on the hydrogen economy as a pathway to reach net-zero CO2 emissions in Europe†., *Energy Environ Sci*, **2022**, *15*, (3), 1034–1077.
8. Jiang, K.; Liu, B.; Luo, M.; Ning, S.; Peng, M.; Zhao, Y.; Lu, Y. R.; Chan, T. S.; de Groot, F. M. F.; Tan, Y., Single platinum atoms embedded in nanoporous cobalt selenide as electrocatalyst for accelerating hydrogen evolution reaction., *Nat Commun*, **2019**, *10*, (1).
9. He, T.; Wang, W.; Shi, F.; Yang, X.; Li, X.; Wu, J.; Yin, Y.; Jin, M., Mastering the surface strain of platinum catalysts for efficient electrocatalysis., *Nature*, **2021**, *598*, (7879), 76–81.
10. Feidenhans'l, A. A.; Regmi, Y. N.; Wei, C.; Xia, D.; Kibsgaard, J.; King, L. A., Precious Metal Free Hydrogen Evolution Catalyst Design and Application., *Chemical Reviews*, **2024**, *124*, (9), 5617–5667.
11. Dubouis, N.; Grimaud, A., The hydrogen evolution reaction: From material to interfacial descriptors., *Chem Sci*, **2019**, *10*, (40), 9165–9181.
12. Nørskov, J. K.; Bligaard, T.; Logadottir, A.; Kitchin, J. R.; Chen, J. G.; Pandelov, S.; Stimming, U., Trends in the Exchange Current for Hydrogen Evolution., *J Electrochem Soc*, **2005**, *152*, (3), J23.

13. Durst, J.; Siebel, A.; Simon, C.; Hasché, F.; Herranz, J.; Gasteiger, H. A., New insights into the electrochemical hydrogen oxidation and evolution reaction mechanism., *Energy Environ Sci*, **2014**, *7*, (7), 2255–2260.

14. Lamoureux, P. S.; Singh, A. R.; Chan, K., PH Effects on Hydrogen Evolution and Oxidation over Pt(111): Insights from First-Principles., *ACS Catal*, **2019**, *9*, (7), 6194–6201.

15. Huang, B.; Rao, R. R.; You, S.; Hpone Myint, K.; Song, Y.; Wang, Y.; Ding, W.; Giordano, L.; Zhang, Y.; Wang, T.; Muy, S.; Katayama, Y.; Grossman, J. C.; Willard, A. P.; Xu, K.; Jiang, Y.; Shao-Horn, Y., Cation- and pH-Dependent Hydrogen Evolution and Oxidation Reaction Kinetics., *JACS Au*, **2021**, *1*, (10), 1674–1687.

16. Monteiro, M. C. O.; Goyal, A.; Moerland, P.; Koper, M. T. M., Understanding Cation Trends for Hydrogen Evolution on Platinum and Gold Electrodes in Alkaline Media., *ACS Catal*, **2021**, *11*, (23), 14328–14335.

17. Jiang, Y.; Lu, Y., Designing transition-metal-boride-based electrocatalysts for applications in electrochemical water splitting., *Nanoscale*, **2020**, *12*, (17), 9327–9351.

18. Hong, J.; Mutalik, S.; Pescarmona, P. P.; Protesescu, L., Metal Borides: From Industrial Classics to Versatile Colloidal Nanocrystals for Energy, Catalysis, and Hard Coatings Applications†., *Chemistry of Materials*, **2024**, *36*, (5), 2147–2164.

19. Kawashima, K.; Márquez, R. A.; Smith, L. A.; Vaidyula, R. R.; Carrasco-Jaim, O. A.; Wang, Z.; Son, Y. J.; Cao, C. L.; Mullins, C. B., A Review of Transition Metal Boride, Carbide, Pnictide, and Chalcogenide Water Oxidation Electrocatalysts., *Chem Rev*, **2023**, *123*, (23), 12795–13208.

20. Lee, E.; Fokwa, B. P. T., Nonprecious Metal Borides: Emerging Electrocatalysts for Hydrogen Production., *Acc Chem Res*, **2022**, *55*, (1), 56–64.

21. Park, H.; Encinas, A.; Scheifers, J. P.; Zhang, Y.; Fokwa, B. P. T., Boron-Dependency of Molybdenum Boride Electrocatalysts for the Hydrogen Evolution Reaction., *Angew Chem Int Ed*, **2017**, *56*, (20), 5575–5578.

22. Park, H.; Zhang, Y.; Lee, E.; Shankhari, P.; Fokwa, B. P. T., High-Current-Density HER Electrocatalysts: Graphene-like Boron Layer and Tungsten as Key Ingredients in Metal Diborides., *ChemSusChem*, **2019**, *12*, (16), 3726–3731.

23. Jothi, P. R.; Zhang, Y.; Scheifers, J. P.; Park, H.; Fokwa, B. P. T., Molybdenum diboride nanoparticles as a highly efficient electrocatalyst for the hydrogen evolution reaction., *Sustain Energy Fuels*, **2017**, *1*, (9), 1928–1934.

24. Kim, S. B.; Yapo, J. A.; Yasuhara, A.; Yubuta, K.; Fokwa, B. P. T., Vanadium-Stabilized MoB Nanoparticles Enable Hydrogen Evolution at Industry-Relevant High Current Densities., *Small*, **2025**, *21*, (24), 2412693.

25. Lu, B.; Guo, L.; Wu, F.; Peng, Y.; Lu, J. E.; Smart, T. J.; Wang, N.; Finfrock, Y. Z.; Morris, D.; Zhang, P.; Li, N.; Gao, P.; Ping, Y.; Chen, S., Ruthenium atomically dispersed in carbon outperforms platinum toward hydrogen evolution in alkaline media., *Nat Commun*, **2019**, *10*, (1).

26. Yang, Y.; Yu, Y.; Li, J.; Chen, Q.; Du, Y.; Rao, P.; Li, R.; Jia, C.; Kang, Z.; Deng, P.; Shen, Y.; Tian, X., Engineering Ruthenium-Based Electrocatalysts for Effective Hydrogen Evolution Reaction., *Nano-Micro Letters*, **2021**, *13*, (1).

27. Luo, W.; Wang, Y.; Cheng, C., Ru-based electrocatalysts for hydrogen evolution reaction：Recent research advances and perspectives., *Materials Today Physics*, **2020**, *15*.

28. Mahmood, J.; Li, F.; Jung, S. M.; Okyay, M. S.; Ahmad, I.; Kim, S. J.; Park, N.; Jeong, H. Y.; Baek, J. B., An efficient and pH-universal ruthenium-based catalyst for the hydrogen evolution reaction., *Nat Nanotechnol*, **2017**, *12*, (5), 441–446.

29. Zou, X.; Wang, L.; Ai, X.; Chen, H.; Zou, X., Crystal phase-dependent electrocatalytic hydrogen evolution performance of ruthenium-boron intermetallics., *Chemical Communications*, **2020**, *56*, (20), 3061–3064.

30. Qiao, Y.; Yuan, P.; Pao, C. W.; Cheng, Y.; Pu, Z.; Xu, Q.; Mu, S.; Zhang, J., Boron-rich environment boosting ruthenium boride on B, N doped carbon outperforms platinum for hydrogen evolution reaction in a universal pH range., *Nano Energy*, **2020**, *75*.

31. Hodnik, N.; Jovanovič, P.; Pavlišič, A.; Jozinović, B.; Zorko, M.; Bele, M.; Šelih, V. S.; Šala, M.; Hočevar, S.; Gaberščček, M., New insights into corrosion of ruthenium and ruthenium oxide nanoparticles in acidic media., *Journal of Physical Chemistry C*, **2015**, *119*, (18), 10140–10147.

32. Fahrenholtz, W. G.; Binner, J.; Zou, J., Synthesis of ultra-refractory transition metal diboride compounds., *J Mater Res*, **2016**, *31*, (18), 2757–2772.

33. Jothi, P. R.; Yubuta, K.; Fokwa, B. P. T., A Simple, General Synthetic Route toward Nanoscale Transition Metal Borides., *Adv Mater*, **2018**, *30*, (14), 2–7.

34. Portehault, D.; Devi, S.; Beaunier, P.; Gervais, C.; Giordano, C.; Sanchez, C.; Antonietti, M., A General Solution Route toward Metal Boride Nanocrystals., *Angewandte Chemie*, **2011**, *123*, (14), 3320–3323.

35. Gupta, S.; Patel, N.; Miotello, A.; Kothari, D. C., Cobalt-Boride: An efficient and robust electrocatalyst for Hydrogen Evolution Reaction., *J Power Sources*, **2015**, *279*, 620–625.

36. Zeng, M.; Wang, H.; Zhao, C.; Wei, J.; Qi, K.; Wang, W.; Bai, X., Nanostructured Amorphous Nickel Boride for High-Efficiency Electrocatalytic Hydrogen Evolution over a Broad pH Range., *ChemCatChem*, **2016**, *8*, (4), 708–712.

37. King, M. E.; Personick, M. L., Iodide-induced differential control of metal ion reduction rates: synthesis of terraced palladium-copper nanoparticles with dilute bimetallic surfaces., *J Mater Chem A Mater*, **2018**, *6*, (44), 22179–22188.

38. King, M. E.; Kent, I. A.; Personick, M. L., Halide-assisted metal ion reduction: Emergent effects of dilute chloride, bromide, and iodide in nanoparticle synthesis., *Nanoscale*, **2019**, *11*, (33), 15612–15621.

39. Ghosh, S.; Manna, L., The Many 'facets' of Halide Ions in the Chemistry of Colloidal Inorganic Nanocrystals., *Chemical Reviews*, **2018**, *118*, (16), 7804–7864.

40. Duchene, J. S.; Niu, W.; Abendroth, J. M.; Sun, Q.; Zhao, W.; Huo, F.; Wei, W. D., Halide anions as shape-directing agents for obtaining high-quality anisotropic gold nanostructures., *Chemistry of Materials*, **2013**, *25*, (8), 1392–1399.

41. Kravchenko, S. E.; Domashnev, I. A.; Dremova, N. N.; Vinokurov, A. A.; Shilkin, S. P., Synthesis of Vanadium Diboride Nanoparticles via Reaction of Amorphous Boron with Vanadium in KCl and Na2B4O7 Ionic Melts., *Inorg Mater*, **2019**, *55*, (5), 443–448.

42. Yang, P.; Zhou, B.; Wang, J.; Wang, Y.; Chen, Z.; Wang, X.; Wang, L.; Liu, F.; Wu, Z., Molten salt assisted to synthesize molybdenum–ruthenium boride for hydrogen generation in wide pH range., *Int J Hydrogen Energy*, **2023**, *48*, (57), 21568–21577.

43. Goyal, A.; Koper, M. T. M., The Interrelated Effect of Cations and Electrolyte pH on the Hydrogen Evolution Reaction on Gold Electrodes in Alkaline Media., *Angewandte Chemie International Edition*, **2021**, *60*, (24), 13452–13462.

44. Li, P.; Jiang, Y.-L.; Men, Y.; Jiao, Y.-Z.; Chen, S., Kinetic cation effect in alkaline hydrogen electrocatalysis and double layer proton transfer., *Nat Commun*, **2025**, *16*, (1), 1844.

45. Gou, W.; Wang, Y.; Zhang, M.; Tan, X.; Ma, Y.; Qu, Y., A review on fundamentals for designing stable ruthenium-based catalysts for the hydrogen and oxygen evolution reactions., *Chinese Journal of Catalysis*, **2024**, *60*, 68–106.

46. Zhang, Y.; Huang, W.; Wei, H., Electrocatalytic Stability Over Ruthenium-Based Catalysts for Proton Exchange Membrane Water Electrolysis., *ChemCatChem*, **2025**, *17*, (5).

47. Xue, Y.; Zhao, J.; Huang, L.; Lu, Y.-R.; Malek, A.; Gao, G.; Zhuang, Z.; Wang, D.; Yavuz, C. T.; Lu, X., Stabilizing ruthenium dioxide with cation-anchored sulfate for durable oxygen evolution in proton-exchange membrane water electrolyzers., *Nat Commun*, **2023**, *14*, (1), 8093.

Chapter 5.

Conclusion

Here, I conclude by returning to the two barriers that have long limited transition-metal borides (TMBs) in water electrolysis: reliable, phase-controlled nanoparticle synthesis without boron-rich passivation, and a mechanistic bridge that connects composition, structure, and surfaces to performance at device-relevant current densities. This thesis addresses both. By leveraging a $Sn/SnCl_2$ redox–flux and the immiscibility of Sn with B, I established a controllable, low-temperature route to crystalline TMB nanoparticles with clean surfaces and well-defined chemistries. The method reduces the need for large excess boron, mitigates coarsening, and streamlines post-processing—practical advantages that enable rigorous comparisons across compositions and scalable preparation for electrolysis.

Within this synthesis platform, vanadium-stabilized molybdenum monoboride ($V_{0.3}Mo_{0.7}B$) nanoparticles emerged as a non-PGM catalyst that delivers in the regime that matters for deployment. The material outperforms commercial Pt/C beyond a few hundred mA cm^{-2} and sustains industrial-level operation, reaching ~1000 mA cm^{-2} at ~0.45 V in acid with ~97% activity retention over ~28 hours. Electrochemical analyses (Tafel behavior, C_{dl}-derived ECSA, and EIS) indicate a higher accessible active-site density and lower charge-transfer resistance than MoB-based composites. Complementary DFT links these observations to hydrogen-binding energetics: on the dominant {112} facet, ΔG_H shifts toward thermoneutrality at high coverage, rationalizing the superiority specifically

in the high-current regime. Together, these results provide a coherent synthesis-to-descriptor-to-device picture for a practical, platinum-free HER cathode.

A second key outcome is a clarified structure–activity relationship in the Mo–B system. By precisely tuning Sn and B inputs, I accessed single-phase α-MoB_2 (MoB_2-SP) without sacrificial excess boron, alongside two composite regimes (MoB_2/MoB and MoB_2/B). Despite larger particles and lower geometric surface area than the composites, MoB_2-SP exhibits strong intrinsic HER activity. This finding emphasizes that phase purity and electronic structure—i.e., which terminations and facets are actually expressed—govern kinetics more decisively than surface area alone. It also helps reconcile literature reports where high apparent activities coincided with mixed phases or boron-rich surface layers.

The broader implications are straightforward. In designing TMB catalysts, synthetic knobs that stabilize the electronically optimal phase (including judicious alloying or solid-solution formation) should take precedence over strategies that merely inflate surface area at the expense of phase purity. Facet control matters: targeting surfaces confirmed by PXRD/TEM and evaluating ΔG_H at high hydrogen coverage provide more faithful guidance for $\geq 10^2$–10^3 mA cm^{-2} operation. Finally, electrode architecture is part of the catalyst at scale—bubble management, film porosity, and conductivity pathways can reinforce or obscure intrinsic kinetics and must be engineered in concert.

Chapter 4 addresses a long-standing barrier in Ru-borides—nanosizing and phase selection in the presence of volatile halides. We show that pairing RuI_3 with ~50 wt% KCl simultaneously suppresses iodide-driven runaway transport and provides a benign molten-

salt flux above ~770-800 °C, enabling intact pellets and reaction completion at 850 °C to yield a nanoscale RuB2/Ru_2B_3 composite (I-RuB2/Ru_2B_3). A chloride/Sn comparator converges to a similar composite but with coarser grains (Cl-RuB2/Ru_2B_3), while pushing the chloride route to eightfold excess B favors near-single-phase RuB_2 with a B-rich overlayer (Cl-RuB_2/B)—mirroring MoB_2 behavior. The iodide-enabled product exhibits low overpotentials (0.5 M H_2SO_4: 13.0/101.7 mV at 10/150 mA cm^{-2}; 1 M KOH: 15.6/122 mV), and Pt-like Tafel slopes (< 30 mV dec^{-1}), with ~97% activity retained after 5000 cycles in alkaline electrolyte without conductive supports. Together these results map practical synthesis windows for boron-rich Ru-borides and clarify activity–stability trade-offs across pH.

Beyond the specific chemistries, several cross-cutting principles emerge. (i) Substitutional stabilization (e.g., V in MoB) can reduce synthesis severity and particle size while preserving intrinsic active motifs, translating to higher active-site densities and lower transport resistances at scale currents. (ii) Excess-boron strategies promote diboride phase purity but may deposit resistive B-rich overlayers that dull high-current response, demanding careful balance between purity and interfacial conductivity. (iii) Precursor/halide identity is a powerful and underused lever: iodide has strong kinetic leverage yet must be moderated; coupling RuI_3 with KCl is an effective volatility-management and flux strategy that should generalize to other volatile-halide TMB systems. Finally, durability in acidic media remains a challenge for Ru systems due to oxidation/dissolution pathways; emerging solutions—metal–support interactions,

heterointerface design, and electrolyte micro-environment (e.g., alkali-cation) engineering—offer complementary routes to retain activity while mitigating degradation.

Overall, the thesis demonstrates that judicious control over precursor chemistry, flux, and stoichiometry yields nanosized, boron-rich TMBs with HER metrics that rival noble-metal benchmarks at technologically relevant current densities, while outlining practical synthesis maps and durability pathways for future device-level deployment.